High precision laser micromachining for sensing applications

Frank Albri

Submitted for the degree of Doctor of Philosophy

Heriot-Watt University

School of Engineering and Physical Sciences / Institute of Photonics and Quantum Sciences

December 2014

Abstract

In this PhD thesis the development of laser-based processes for sensing applications is investigated. The manufacture of optical fibre sensors is of particular interest because fibre optics offers advantages in space constraint environments or in environments where electronic sensors fail. Laser micromilling of the transparent and mechanically challenging to machine materials sapphire and fused silica is investigated. An industrial picosecond laser providing 6 ps pulses with the ability to emit at 1030 nm (IR), 515 nm (green) and 343 nm (UV) is used for processing of these materials; providing a maximum laser pulse energy of 25 µJ at UV, 75 µJ at green and 125 µJ in IR. The UV wavelength is identified as the most reliable machining wavelength for these materials with the least amount of cracking and achieving a surface roughness R_q of just 300 nm compared to 1220 nm (green) and 1500 nm (IR) in fused silica. In sapphire the surface roughness is 420 nm using UV , with green it is 500 nm and using IR it is 800 nm. The material removal rates using this laser milling process are larger than with other micromachining techniques, hence it was applied to manufacture cantilever sensors on the end of an optical fibre. The monolithic fibre top sensor is carved out of conventional telecommunications optical fibre. The cantilever is a structure of less than 10 µm thickness, 20 µm width and 125 µm length. Using the Fabry-Perot interferometer method the sensor detects small movements with a resolution better than 15 nm. A technique is developed to correct for laser machining angles and hence generate parallel interferometer faces. An electric arc cleaning process of the laser manufactured cantilever sensors is investigated that reduces the surface roughness to 30 nm. The manufacturing process reduces manufacturing times by a factor of 100. A working sensor is demonstrated in a deflection experiment.

Such short pulses are not always required to manufacture the highest resolution sensors. The manufacture of high precision optical encoder scales (pitch 8 µm, depth 200 nm) with two processes (i) ablative removal of a polyimide layer and (ii) a melt reflow process on nickel coated scales is demonstrated. Both processes are using 33 ns laser pulses at 355 nm generating a pulse energy of up to 1 mJ.

Acknowledgements

Many people have an influence on getting someone to write a thesis. In this section I would like to thank the people that were most important and had most influence on this thesis and helped me to do the research, write the thesis and not give up.

Firstly, I would like to thank my supervisor, Professor Duncan Hand, for offering me the opportunity to work within the Applied optics and photonics group at Heriot-Watt University. I would like to stress the importance of his guidance and vision throughout the period of my active research. Furthermore his continued support and many phone calls during the period of writing up helped me to finish this thesis. I would also like to mention Robert Maier who gave continued input during meetings and always offered a second opinion and often had a different point of view. Finally special thanks go to Richard Carter, he offered some supreme proof reading in some cases in a record breaking time. He helped in many cases with turning my broken English into a readable state and for his reading stamina and not giving up. Many thanks to Krystian Wlodarczyk for helpful discussions and support in the laboratories.

I would like to thank the colleagues in my office who although not always helpful regarding scientific matters you were always good for a discussion about developments in football and about Liverpool. I would also like to thank all those who played football with me. Special thanks to Daniel Rylatt, and Conny Gollek for being really good neighbours. I will always remember the lengthy discussions about research as well as private matters, enjoying good beers and good wine on your couch.

Last but not least I would like to thank my parents who lay the foundation of my education. I also have to thank them for their patience and continued support throughout my life. The greatest thanks have to be expressed towards the person who might have suffered the most during the time of research and writing, my fiancée Alla. Thank you for your continued support and believe in me even in difficult times.

ACADEMIC REGISTRY
Research Thesis Submission

Name*:*	Frank Albri		
School/PGI:	EPS / IPAQS		
Version: *(i.e. First, Resubmission, Final)*	Final	Degree Sought (Award **and** Subject area)	Doctor of Philosophy in Physics

Declaration

In accordance with the appropriate regulations I hereby submit my thesis and I declare that:

1) the thesis embodies the results of my own work and has been composed by myself
2) where appropriate, I have made acknowledgement of the work of others and have made reference to work carried out in collaboration with other persons
3) the thesis is the correct version of the thesis for submission and is the same version as any electronic versions submitted*.
4) my thesis for the award referred to, deposited in the Heriot-Watt University Library, should be made available for loan or photocopying and be available via the Institutional Repository, subject to such conditions as the Librarian may require
5) I understand that as a student of the University I am required to abide by the Regulations of the University and to conform to its discipline.

* *Please note that it is the responsibility of the candidate to ensure that the correct version of the thesis is submitted.*

Signature of Candidate*:*		Date:	

Submission

Submitted By *(name in capitals):*	
Signature of Individual Submitting:	
Date Submitted:	

For Completion in the Student Service Centre (SSC)

Received in the SSC by *(name in capitals):*			
Method of Submission *(Handed in to SSC; posted through internal/external mail):*			
*E-thesis Submitted (**mandatory for final theses)***			
Signature:		Date:	

TABLE OF CONTENTS

Chapter 1: Introduction

1.1 Opening words and motivation

The invention of the laser has been the beginning for a whole new field of science. Many topics were boosted by the excitement surrounding the laser although it took several years to fully develop processes and applications. Topics that increased in interest were optics, spectroscopy, chemistry and engineering in general. Many developments in current technology are based on the success story of the laser. Devices that are commonly used today like compact disc players would not have been possible without the laser. Broadband communication and high speed internet across the globe as well as telecommunications are only made possible by the laser. One topic that might be less in the centre of attention for the general public is the laser in manufacturing. The laser provides an ideal manufacturing tool for many processes, the most common include processing of metal sheets including cutting, welding and drilling. The main advantages of lasers include near zero tool wear, quick changes in manufacturing design, and the ability to produce focus a high intensity onto a small spot. In recent years the processing of glass has become more and more important as technology advances and devices such as smartphones and large screen televisions require special glasses that are cut with a very high precision. Ideally this process is also very fast and often with complex shapes to allow for buttons and other design features. Many of the more recent developments were achieved with short and ultrashort laser pulses because these are fairly new as a valid tool for the manufacturing industry and therefore offer new oppertunities.

This thesis focuses on the application of short and ultrashort pulsed lasers for high precision material structuring. Example applications are investigated that are impossible or not commercially feasible to manufacture with other technologies. These are the laser micromilling of the transparent ceramics sapphire and fused

silica; micromilling of fused silica for optical fibre sensor applications focusing on the example of a fibre top cantilever sensor; and the generation of optical encoder scales for high precision motion stages. Two of these applications require ultrashort (picosecond) laser pulses; however the encoder structuring provides a much better result with the significantly longer pulsed nanosecond laser, despite demanding a sub-micron vertical precision.

The process that is described for optical fibre top cantilever sensor manufacturing provides a significant improvement in processing time over the previously used technique and so reduces the production cost to a level where mass production becomes feasible. Even with a semi-automated process with manual adjustment of the rotation stages, the process achieved was a rate of one cantilever every six minutes, and this could easily be reduced by a factor of 10 by automating the alignment process. In contrast, the current technique uses a focussed ion beam manufacture process where one cantilever is produced every 4 hours. One important parameter for the manufacture of optical sensing elements is the surface finish to minimise loss due to surface scattering. With typical laser ablation processes the surface roughness is high with an R_a of 200 – 400 nm. We hence developed a post processing technique using an electric arc to reduce the surface roughness of laser manufactured cantilevers.

1.2 Summary of chapters

- **Chapter 2: Literature review** comprises a review of conventional micromachining technologies, including abrasive processing, etching, and particle beam methods. This chapter also gives an introduction to the use of lasers in manufacturing and applications of ultrashort laser pulses, and their main advantages over conventional micromachining methods when machining hard and brittle ceramics.
- **Chapter 3: Micromilling of fused silica and sapphire.** In this chapter the process of laser micromilling the transparent materials fused silica and sapphire is investigated. Such materials are difficult to machine by other

means, so the laser is a particularly attractive solution. Material removal efficiencies and the impact of wavelength are investigated, and the tradeoff between efficiency and quality is presented.

- **Chapter 4: Manufacture of cantilever based optical fibre sensing devices** covers the design and the working principle of a fibre optical cantilever sensor and two different design ideas are examined in detail. One of these is a small cantilever machined from the end-face of the fibre whilst the other uses a side cantilever and total internal reflection. The development of a process to manufacture fibre top type cantilever sensors is described. This uses a picosecond laser. The surface quality of the machined surfaces is assessed and processes to improve the surface quality are evaluated. A sensor manufactured in this way is demonstrated in an example application.
- **Chapter 5: Manufacture of high precision encoder scales using a nanosecond laser process** contains the description of a high precision manufacture problem which is best solved by using a nanosecond (rather than picosecond) pulsed laser. The longer pulse enables a purely melting process, avoiding the optically rough surface produced by laser ablation. Different example processes are described to generate the desired feature on various materials.
- **Chapter 6: Conclusion** provides an overall conclusion of the research work and investigations carried out in this thesis. It lists some suggestions for future research and suggestions for the continuation of the work.

Chapter 2: Literature review

One of the main factors driving economic growth in recent years has been miniaturization. In manufacturing and in electronics miniaturization is pushing towards new boundaries. When feature sizes in the micron range are required traditional manufacturing methods do not work and so other methods are required. This literature review provides an overview of several methods that can be used to machine on the micron scale, with a particular emphasis on laser processes.

2.1 Motivation: Challenges and issues in high precision laser machining

High precision machining has several challenges. Within very small structures the mechanical properties become increasingly important. For example the thickness of a wall is limited when using mechanical milling because a milling tool always has a feed rate that also applies a force onto the milled surfaces. Depending on the geometries and the pattern design that is to be machined other structures might limit the use of certain manufacturing techniques. Many materials, particularly hard and brittle materials, are difficult to machine with mechanical tools. However lasers can remove material and achieve a good quality, and are capable of providing complex 3D shapes.

2.2 Overview of non-laser micromachining techniques

It is important when setting up a manufacturing process to understand the limitations and advantages of the various processes that are available to solve a certain task. To achieve optimal machining, several factors play a role and it is important to recognise that the highest quality is not always the most important factor; often the cost of a process is more important. In some cases a better design of a part allows a different manufacturing technique to be selected. All these different aspects make it very complex to optimise the manufacture of a part. This is the case for large scale manufacturing as well as micro-manufacturing. On the microscale many different processes are, however, competing each of them with its advantages and

disadvantages. The next section examines some of these factors and highlights example applications where each method achieves good or the best results.

2.2.1 Micromilling

Micromilling in concept is very similar to the macroscopic milling process. It also uses a tool that rotates at a very high rate. The edges of the tool remove a small amount of material from the work piece with every turn. The tool is typically a few tens of microns in diameter therefore the material removal rate with each turn is kept low to ensure low tool wear and to avoid tool breakage [1]. Tools for Micromilling are produced by focused ion beam (FIB) machining to achieve the smallest tool diameters of 22 µm. It is possible to use such tools to manufacture structures and walls as thin as 8 µm and the typical angle of the walls is 89.5° to the supporting substrate [2, 3]. It is, however, very difficult to use micromilling for 3-dimensional or free standing structures that have only very little supporting area. Machining a groove is much simpler than machining a wall, hence the dimensions to cut or to make a groove are much smaller and ultimately dependent on the tool diameter. Grooves as thin as 1-2 µm have been achieved with this method [3].

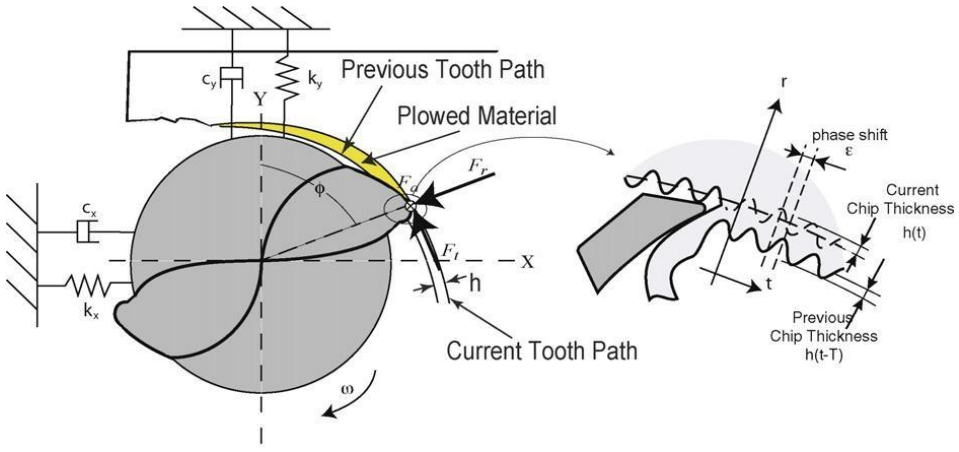

Figure 2.1: Schematic drawing of the micromilling process showing the important terms and and the material removal mechanism in a traditional milling process.

In any milling process the parameters that are important are the rotation speed and the feed rate. Often special tools having a cutting edge angle that is specific to the material and feature size are necessary for good results.

Micromilling of hard and brittle materials such as fused silica, sapphire and many other ceramics is very difficult. The hardness of the materials requires specialized milling tools. Often diamond tools are used, however diamond tools on the micron scale need to be specially manufactured through focussed ion beam (FIB) milling. This makes them expensive due to long manufacturing times and an expensive FIB machine. Furthermore the tool wear is high and detecting tool breakage is difficult. This can damage the sample [4, 5] as the brittle ceramics tend to crack under mechanical stress. This limits the precision that is achieved. Only very slow milling speeds are possible without large cracks. Recently a micromilling regime (feed rate, rotational speed and contact angle of the cutting edge) was found in which glass can be machined in a ductile mode and hence machining results in a very smooth surface, but it is also very slow at feed rates below 6 μms^{-1}. Typical surface features that are achieved with this technique in glass are in the order of hundreds of µm due to the radius of the tools used [6, 7].

2.2.2 Abrasive methods

The use of abrasive tools is a traditional machining technique that has been exploited for centuries. It is not a surprise that it can also be used for micromachining, since abrasive methods use small hard grains that remove small amounts of material. As a large number of grains are used together it is possible to machine large volumes. The material is removed through the amount of impacts a large number of small grains that each remove a very small amount of material and hence together they can remove larger volumes. The mechanisms are very similar to micromilling, in that the tool is rotated and each rotation removes a small amount of material. The best known techniques of abrasive machining are grinding and polishing, both techniques are very similar, commonly grinding is used for the rough shape while polishing is used for final finishing of a part. All kinds of material can be ground, even hard and

brittle materials, e.g. fused silica optics. While the rough grinding process is fast because it can be applied on a large area, the better the surface quality required the slower the process becomes.

Ultrasonic micro machining by comparison uses a slurry which is a suspension of diamond or silica particles in a liquid.

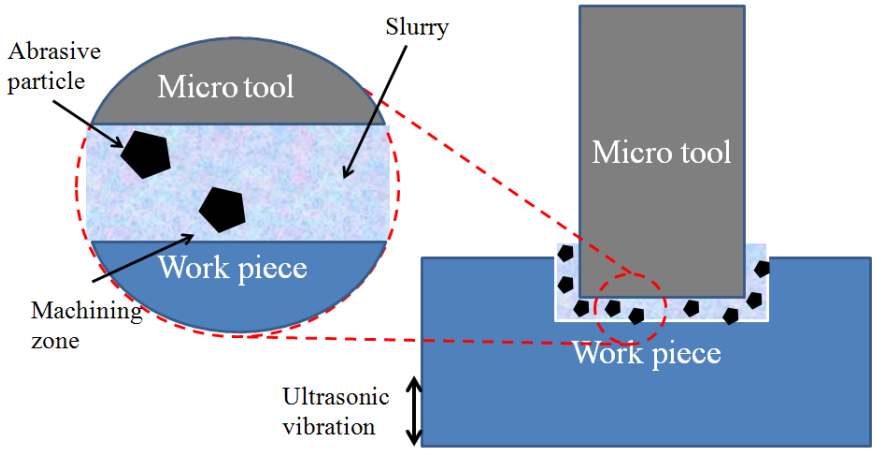

Figure 2.2: Schematic of ultrasonic micromachining using the work piece vibration method.

A special tool, often made of tungsten or other hard metals, is brought in close proximity to the work piece and the slurry is continuously pumped into the space between the work piece and the tool [8, 9]. The slurry has two advantages. It carries the debris away from the machining area and it also acts as a coolant. The material removal rates are strongly related to the interacting area and the material hardness. Therefore the bigger the structure the higher the removal rate, machining with a tool diameter of 10 mm can achieve removal rates between 2 and 10 $mm^3 min^{-1}$ [10]. The smallest tool diameters are in the range between 30 and 100 µm which results in holes of diameters > 50 µm. Typical drilling rates for holes are in the order of 3 to 5 µm s^{-1}.

Powder blasting is a well known technique that finds applications in macro machining, for example the removal of paint, and can be utilized for micromachining

as well. With sufficiently small particles (5-30 µm) the smallest structures of 30 µm can be achieved [11]. The surface roughness achieved with powder blasting is limited by the material removal process. Typical values for the surface roughness, $R_{q,}$ are in the range of a few µm (rms). Additionally micro powder blasting requires masks to protect the area that is not machined, which need to be manufactured for each layout, which is not very flexible in terms of quickly changing the machining geometry. However, large areas can be processed in parallel and masks can be reused. The main limitation of powder blasting is the aspect ratio which is typically limited to 2:1. In addition an undercutting effect under the mask often occurs causing problems when not accounted for in the mask design. Some applications however take advantage of this undercutting effect. The powder jet can be positioned at an angle to the work surface to improve the aspect ratio limitations and to produce free standing parts, but this is only done for special, laboratory, applications and not for industrial micro manufacturing [12-15].

2.2.3 Electronic discharge machining (EDM)

EDM is a process in which electronic pulses are applied between a tool and the workpiece, to create sparking and hence remove material. To increase control a liquid dielectric is used between the two surfaces. Each spark removes a small amount of material and a negative of the tool shape is reproduced in the workpiece [3, 16]. In micro-EDM the voltage of the pulses is kept as small as possible to remove only a tiny volume with each pulse. The smallest energies per pulse are in the range of a few nanojoules, Ferri et al reported machining with 3nJ pulses [17]. This technique is suitable for a variety of materials which are hard to machine with other techniques for example hardened steel, carbides, semiconductors and conductive ceramics. When a wire is used as the electrode this is called wire electro-discharge grinding (WEDG) or machining (WEDM). The wire is comsumed by the process arc and constantly fed, which enables degrees of freedom similar to a milling machine. Uniform rods can be machined by rotating the workpiece. Usually a nozzle brings the dielectric liquid to the discharge area and thereby removes the debris created by the previous sparks as well as cooling the substrate and the tool.

The resolution is determined by the area of interaction; in WEDG this is set by the diameter of the wire. *Di et al.* showed feature size of $30.8\mu m$ machined with a wire of a diameter of $30\mu m$ in stainless steel [18]. A very common application of μ-EDM is deburring as reported by *Jeong et al* [19], in which the process is used as a post processing technique to achieve smoother surfaces than with a rough initial machining procedure.

2.2.4 Focused Ion Beam machining

Focused Ion Beam (FIB) machining was mainly developed between 1970 and 1980 with the first commercial machines becoming available in the 1990s [20]. The main advantage of FIB machines is their widespread usability in many applications. They can be used for imaging, milling and deposition applications, and indeed all these modes can be used in combination. The systems are, however, complicated, and require a footprint of 3 m^2. The main disadvantage of FIB machining is that the cost of a machine is very high not only in initial investment but also in maintenance and running costs (> 100 $/h) [21] and low processing speeds with removal rates of 0.2 $\mu m^3 s^{-1}$ in fused silica [22]. The cost, however, is acceptable for some applications where a very specialized and precise control is required. FIBs allow very precise control over the machined depth and pattern, with accurate removal of single layers of atoms. Therefore the main applications are in the semiconductor industry to analyze or to modify parts. They provide an excellent tool for mask inspection and repair. As masks for the semiconductor industry are very expensive and often need only small repairs FIB machines become financially viable.

An FIB machine can be separated into three main parts: (i) the ion column, which provides the ions used for material removal; (ii) the vacuum system and work chamber; (iii) the workstation and control interface which provides the point of user interaction with the machine.

The ion column, which is the main part in terms of mechanics of machining, consists again of several main parts. It is very similar to a column of a scanning electron

microscope, the main difference being that it provides gallium ions rather than electrons. An ion source extracts gallium ions from a liquid gallium cone. The specifics of the ion extraction process depend on the particular system. A typical extraction system works at a voltage of 7000 V[23].

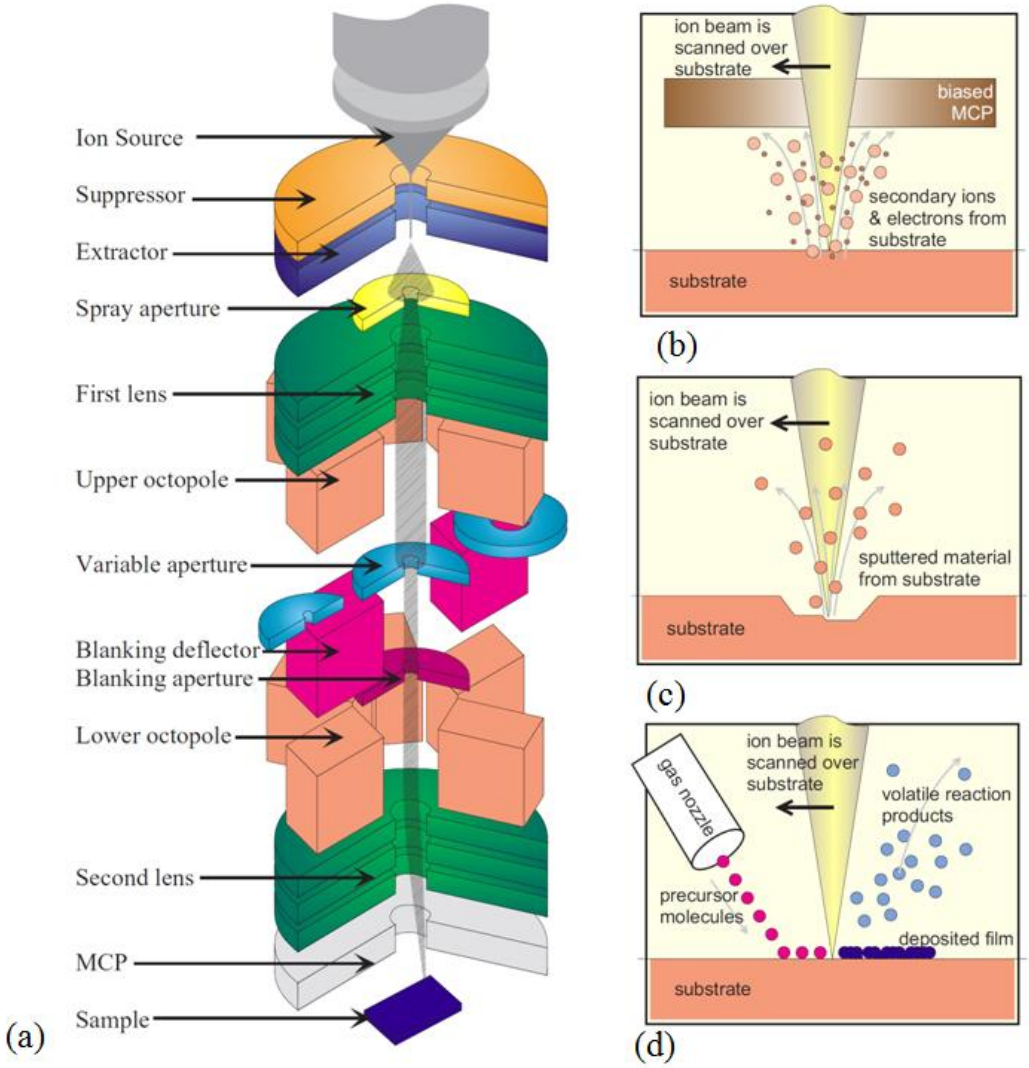

Figure 2.3: Schematic drawing of a (a) typical ion column. The operating modes of an FIB machine are also shown: (b) imaging; (c) milling; (d) deposition. [23]

A schematic drawing of such an ion column is shown in Figure 2.3(a), it shows all the main components that are necessary to achieve the scanning of a focussed ion beam. The ion beam is filtered and condensed by electromagnetic lenses and apertures. Typical ion beam energies are between 10 and 50 keV and currents

between 1 pA and 10 nA. These values are achieved by changing the apertures and acceleration voltages. The current and energy of the ions are the main characteristics of the ion beam. An octopole is used to scan the ion beam across the sample in the user defined pattern. Typical electromagnetic focussing lenses achieve high precision beams with resolutions below 10 nm. A multichannel plate is used to collect the secondary ions and particles for imaging. Most FIBs have a five axis stage system in the work chamber allowing rotation and translation of the samples bigger than the machining area of the scanning beam. The entire work chamber as well as the ion column is placed in a vacuum in the range of 10^{-7} mbar. Such a vacuum is typically established after several minutes of vacuum pumping. For material deposition assist gases can be fed to the working chamber.

The three modes an FIB can operate in are explained in Figure 2.3(b)-(d), however the process of interest for the work presented here is the micromachining mode. The material removal process is driven by the beam of ions that travel at high speeds and therefore carry a high energy, which leads to ion implantation and to sputtering. This removes material, however redeposition occurs as well which lowers the removal rate. Material removal rates strongly depend on the experimental conditions such as the angle of incidence, the current used and the material that is being machined. The variety of materials that can be machined using FIB is large. The materials that are of interest for the work presented here are transparent dielectrics and ceramics. The material removal rate that is achieved in fused silica is 0.172 $\mu m^3 s^{-1}$ [22]. This was achieved with a current of 450 pA, other experiments show that this could be increased by a factor of 2 using assist gases such as I_2 or XeF_2 [24]. Milling rates achieved in sapphire without assist gas are 0.09 $\mu m^3 s^{-1}$. This was increased by a factor of 1.75 by using XeF_2 assist gas and removal rates can be as high as 0.15 $\mu m^3 s^{-1}$ [24].

The material removal using FIB milling is extremely slow, and machining of larger features commonly takes several hours[21, 25, 26]. However the advantages of FIB milling is in the amount of control and the fine features that can be achieved. The feature sizes are in the order of several tens of nm [27] and surface roughness is

usually below 10 nm rms [28]. Further to that it is a technology that allows design parameters to be altered very quickly; also it is a maskless process. The integrated SEM allows on-line monitoring and correction of machining parameters in-process.

2.2.5 Photolithography

The pattern transfer technique, photolithography, is commonly used in the semiconductor industry. This has been the driving force behind the electronics minituarization that has been so important for the growth of the economy in recent years. Photolithograhpy is a multistep process using a mask, exposure and etching. Strictly speaking the etching is not part of the photolithography but is most often considered as such. The entire process usually starts with a wafer or a substrate. A photoresist is applied to the substrate, a mask is brought close to the resist and parts of the resist are exposed to light. The chemistry inside the resist changes due to the light exposure and in a developing and rinse process the depending on the resist the exposed or unexposed parts of the photoresist are washed away. After that the whole sample is exposed to the etchant, however the etchant preferentially etches the parts that are not covered by the photoresist. After that the resist is removed and the desired structure remains on the sample. By repeating these steps with multiple coatings it is possible to produce complex structures. Photolithography techniques are especially useful for mass manufacture because it is a process in which large areas can be machined in parallel. The etching step can be either carried out by "dry" plasma etching or "wet" chemical etching.

The disadvantage of the photolithographic process is that the investment in the masks is large, these are usually written with expensive equipment such as e-beam writers or laser beam writers and a projection system is used to project a miniaturized image of the mask onto the sample. Current chip technology uses excimer lasers as light sources to achieve feature sizes < 50 nm. These are complicated laser systems that also add to the cost of a lithography system. Testing and developing of mask designs is also an expensive process.

2.3 Laser micro machining

The laser can be a very useful tool for manufacturing, this was proven almost immediately after its invention. The capability to tightly focus the laser emission into a small spot, and therefore remotely deliver high energies onto small areas allows very localized material removal. Initial use of this was in spectroscopy of material samples, but the range of applications quickly grew. The historic development of the laser from a niche product to a common tool in manufacturing is outlined in the next section.

2.3.1 History of the laser in manufacturing

The laser was developed from 1958 to 1960 with the first working laser shown by Maiman [29]. However it is impossible to relate the development to a single person. The main theoretical input towards the development of the laser was made by Schawlow and Townes who wrote a theoretical paper about infrared and optical masers [30]. Maiman's laser was a ruby laser, soon after this gas lasers were developed in 1961 [31]. A sort of euphoria spread in these early years and many ideas of possible applications were invented. However the surrounding circumstances limited the possibilities [32]. Many of the projects that were initially started were drawn back or funding was cancelled. In these years the laser was labelled "A solution in search of a problem". Research continued and the number of laser related publications especially in the field of physics grew. Some of the key developments of today's lasers were new crystal materials such as yttrium aluminium garnet (YAG) which is still one of the most common solid state laser materials in the present. The YAG material can be doped with different dopant atoms including neodymium (Nd) and erbium (Er). The first Nd:YAG laser was developed in 1964 [33].

Other improvements especially around gas lasers lead to a quick development of the first laser cutting machines which were reported in 1964 [32]. Metal cutting machines using an assist oxygen gas jet and CO_2-lasers were developed by different

companies in the early 70's. The aircraft industry was one of the first industries to use laser cutting machines for industrial manufacturing, for cutting of titanium alloys. Further milestones in the success story of the lasers were pulsing lasers, with mode-locking and q-switching of lasers enabling shorter pulses and therefore extremely high intensities on the sample. The modelocking technique took off when Anthony J. DeMaria achieved picosecond laser pulses with Nd:glass lasers[34]. These achieved gigawatt peak powers in each pulse.

The development of short and ultra-short laser pulses with enabling techniques such as q-switching and mode-locking are important for the field of micromachining. Because the interaction time of the laser with the material is shorter; the thermal effect of a short pulse on the material is minimized. The effect of the pulse length on laser processing is discussed in more detail in the next two sections.

2.3.2 Laser material interactions

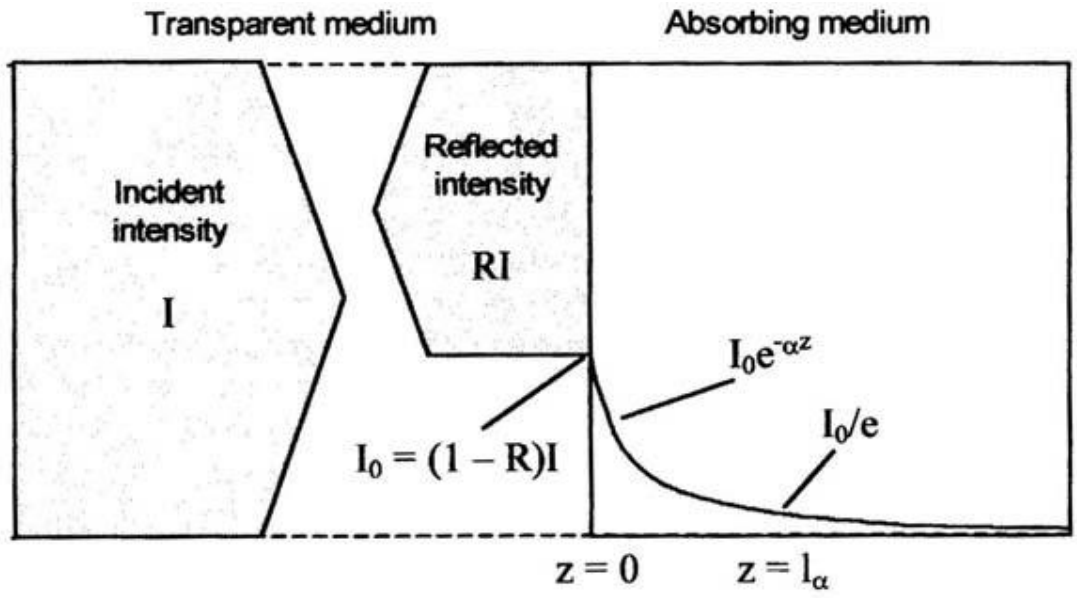

Figure 2.4: Intensity distribution and attenuation process inside the absorbing material [35].

As illustrated in Figure 2.4, the Fresnel reflection coefficient R, and the absorption coefficient α, are important for the success or otherwise of a laser process. Figure 2.5 shows the reflectivity of some metals as a function of wavelength, for most metals the reflectivity is reduced at lower wavelengths and hence the absorption increases.

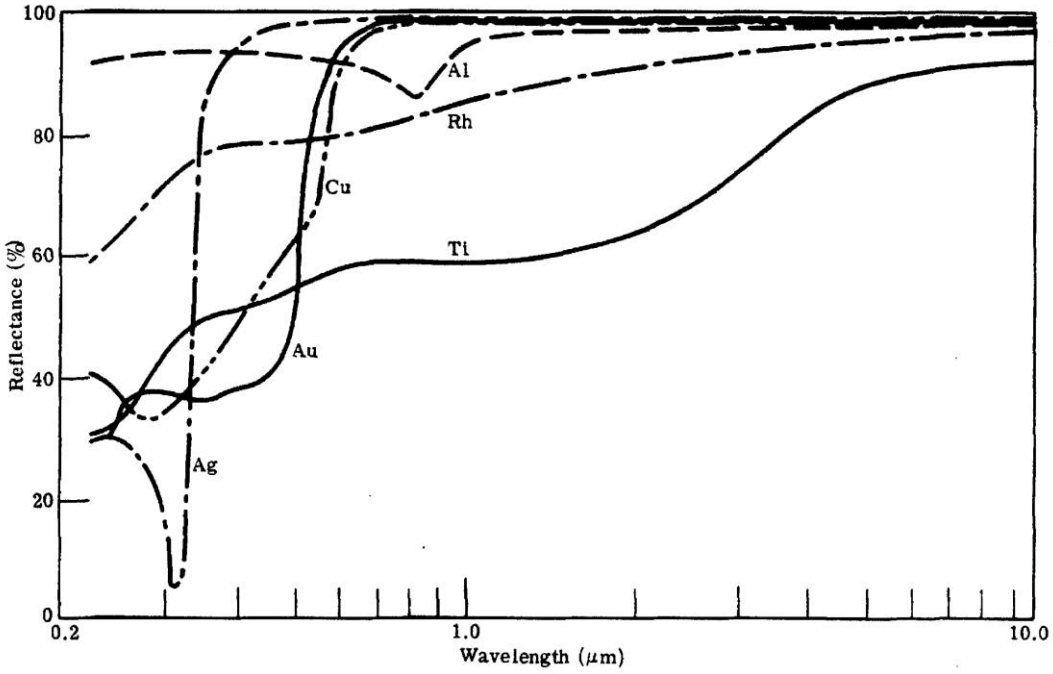

Figure 2.5: Reflectance of some metals as a function of the wavelength [36].

As shown in Figure 2.6, the reflectivity of metals is temperature dependent. In addition an abrupt increase in absorption is typically observed when the melting point is reached [36], which can result in thermal run-away and hence a sudden onset of vapourisation. As shown in Figure 2.6 the lower reflectivity at shorter wavelengths when the temperature is below the material melting point results in a more predictable process.

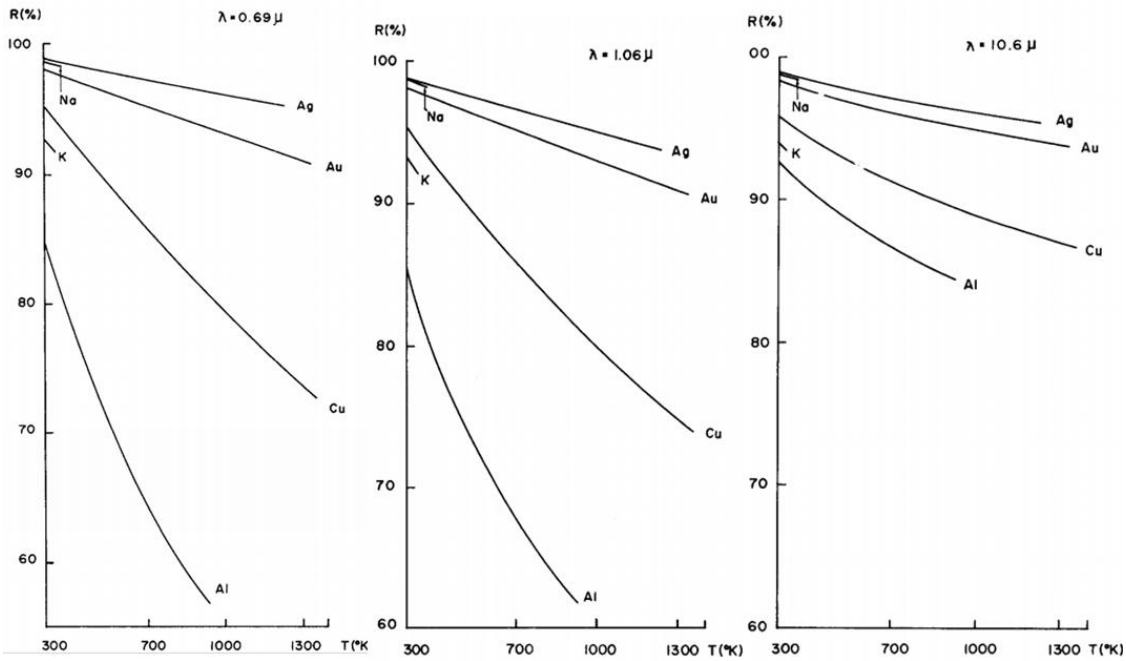

Figure 2.6: Reflectivity of some metals in as a function of temperature for wavelengths of (a) 690 nm; (b) 1060 nm; (c) 10.6 μm[37].

The absorption of light is expressed by the Beer-Lambert law [38]:

$$I(z) = I_0 e^{-\alpha z} \tag{2.1}$$

In this simple equation the intensity I at the depth z is expressed in relation to the incident intensity I_0 and the absorption coefficient α. The absorption coefficient itself depends on: the material, the wavelength, the temperature of the material and many more factors. It is a rather complicated function: however in most cases only a rough approximation is required. A very important and often mentioned value of laser processing is derived from this equation. It is the length or thickness of material over which a significant amount of energy is absorbed inside the material, the so called "attenuation length" [39]

$$L = \frac{1}{\alpha} \tag{2.2}$$

The attenuation length in metals and other highly absorbing materials is only a few nanometers. For an optical fibre meanwhile the attenuation coefficient is often less than 0.5 dB km^{-1}[40]. Laser micromachining of optical fibres and similar low absorption materials is made possible by non linear absorption, which occurs at the very high intensities available from ultrashort lasers, especially in the femtosecond regime. This will be discussed in more detail in section 2.3.5.

Two material removal processes can occur, either a thermally-driven process shown schematically in Figure 2.7, or via a modification of the material on a molecular level i.e. the breaking of chemical bonds. Often a combination with one of the process regimes dominating actually takes place.

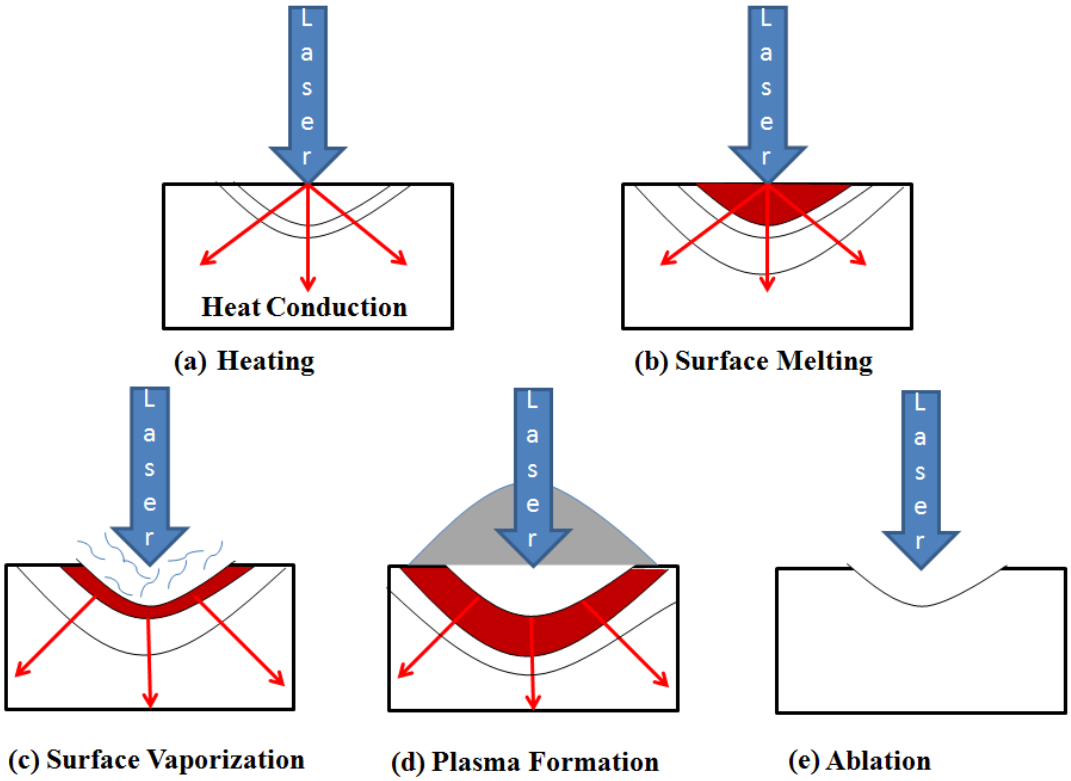

Figure 2.7: Effects during laser matter interactions: (a) heating; (b) surface melting; (c) surface vaporization; (d) plasma formation; (e) ablation. Redrawn from [32].

The length of a laser pulse is a significant factor of laser machining, it is also the main parameter with which lasers are compared because the processing can change

significantly with the pulse length. A short overview of the different processing schemes is given in sections 2.3.3 - 2.3.5.

2.3.3 Continuous wave and long pulsed laser processes up to microsecond pulse length

Processes that rely on long pulsed lasers are mostly thermally driven processes, with a laser pulse that is longer than 100 nanoseconds considered to be a long laser pulse. These processes when used to remove material typically rely on a high average power. Most sheet metal processes are carried out with long laser pulses often longer than micro seconds or even continuous wave lasers because the cut quality that can be achieved is sufficient for many applications. CO_2-lasers are often used for sheet metal processes as mentioned previously. Such lasers were the first to overcome the cooling challenges that arise with high power densities within the gain material. The gas can be quickly exchanged through a flow system, this can be used to remove the heat from the laser cavity and cooling problems that exist with solid state lasers can be overcome, however more modern designs are generally diffusion cooled, often in a design similar to the slab laser where the gas is in a thin layer between the two large area electrodes. Therefore CO_2-lasers can achieve multiple kW average powers. This is sufficient to quickly melt or vaporize metal. With the assistance of gas jets the molten material can quickly be removed from the cut front and very quick processing even of thick steel plates is possible with CO_2 laser machines. This kind of cutting laser often is used in combination with an assist gas which can be used to achieve higher processing rates by encouraging oxidation. A typical setup of a gas nozzle laser head is shown in Figure 2.8 (left) [41] and the results that are typically achieved with this type of setup are shown in Figure 2.8 (right) [42].

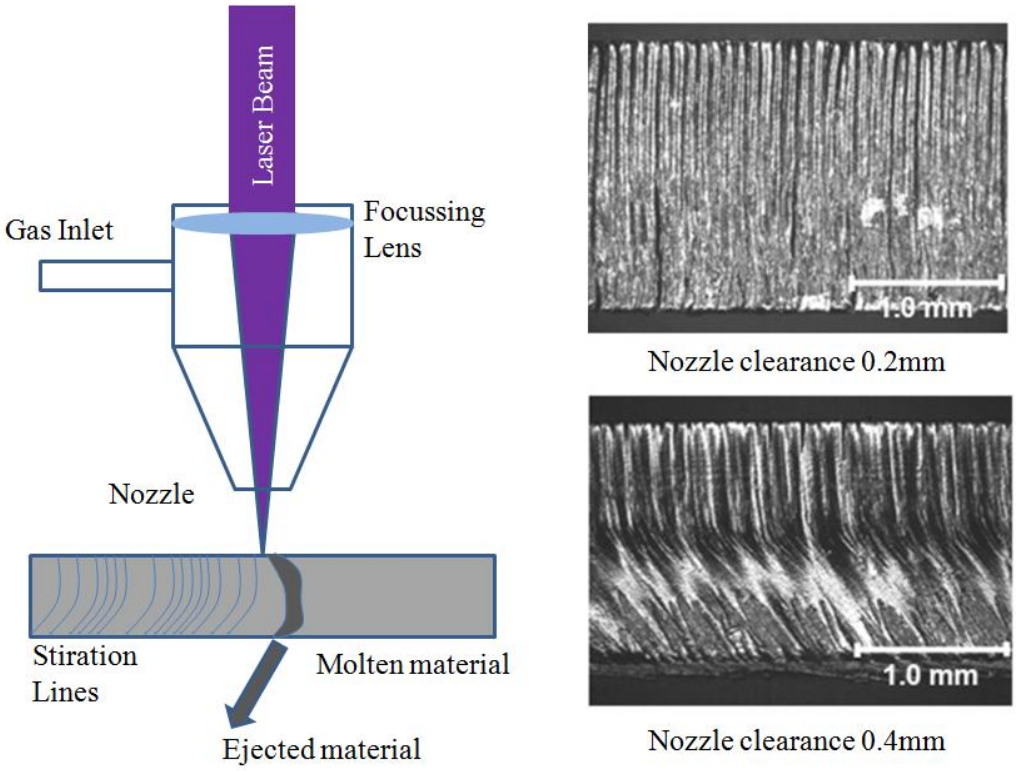

Figure 2.8: (Left) Typical laser cutting setup using a nozzle to create an assist gas jet onto the surface; (right) examples of cut results achieved with laser and gas jets [42].

In the car manufacturing industry, as well as in many others long laser pulses are used very efficiently to cut steel sheets but they also find widespread applications in welding. As a non contact method they offer a high flexibility and near zero tool wear while maintaining a good process control. Welding is a purely thermal process in which no material is to be removed. Hence it lends itself very well to long laser processes.

A very attractive and fairly new process using 100 ns pulses up to cw laser irradiation [43, 44] is additive manufacturing, the process itself is not as new, however, it became more interesting recently with demand for custom parts. A part is formed from a powder by laser melting/sintering, using either a powder jet or a powder bed. With such processes it is possible to build up micro parts through a well focused spot and controlled melting, with feature sizes down to 50 µm [45]. The specific parameters of the process depend on many different factors including the powder parameters as well as the parameters of the finished solid.

2.3.4 Short pulsed laser processes long picoseconds to nanosecond

A very interesting laser pulse length regime is the range from 100's of nanoseconds to 50 picoseconds. In this range most processes have a partial or totally thermal behaviour. The limited pulse length however means that the energy is transferred quickly and therefore the heating takes place in a short time span. This can result in a shallower melt depth or in quick expulsion of the melt pool when vaporization occurs. These short pulses also mean that at high intensities, which are easily achieved at short pulses, the increase of temperature can be sudden and a shock wave is often introduced resulting in cracks. Hence process control becomes more important and parameters such as pulse to pulse stability influence the reliability of the entire process. The advantage of this pulse length regime is that high intensities can be achieved with the very well known technique of q-switching [46]. In this mode of operation a laser emits pulses due to fast switching loss mechanisms. Pumping energy is conserved in the rod and once the q-switch is activated a pulse of very high energy is released from the cavity.

The pulse length range from 100 ns to 50 ps can be used for many applications because the interaction with the material can be tailored, from immediate ablation with some melting on the edges to a pure melting process. In Figure 2.9 images are shown with increasing pulse length, and from 35 ps a molten layer is clearly visible around the hole. For many applications this is however acceptable. Melting does not occur in every material however.

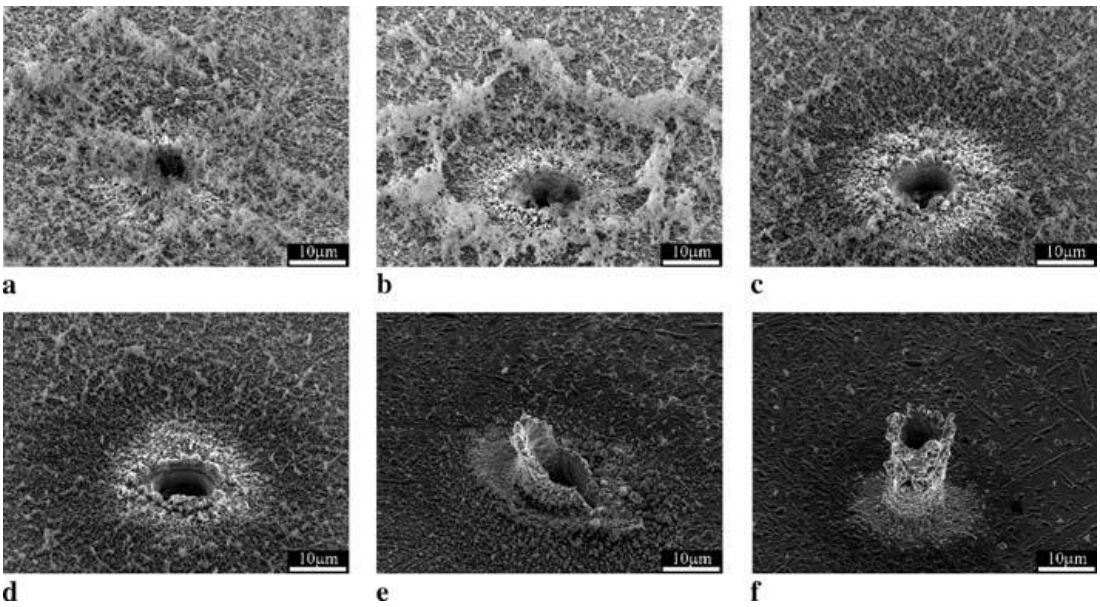

Figure 2.9: SEM images taken from the entrance of a hole drilled through copper with pulse lengths of (a) 150 fs; (b) 1 ps; (c) 10 ps; (d) 35 ps; (e) 220 ps and (f) 7 ns [47]

Melting, however, is not always an unwanted by-product of a laser process, several research groups have shown that the melting can be used for polishing of metals [48-50].

The main advantage of this pulse length over shorter pulses is that in some cases the heating effect can be used to achieve higher machining rates. Drilling and cutting of metals becomes more efficient after melting because the absorption is higher; drilling rates increase with longer pulses. The advantage over longer pulses is that smaller feature sizes can be achieved and melting of just a thin surface layer is possible. In selected materials the same processing regime can be achieved as with ultrashort laser pulses and no or very little difference is visible to ultrashort pulsed laser processing.

The use of this processing regime in high accuracy manufacturing is discussed in more detail in chapter 3.

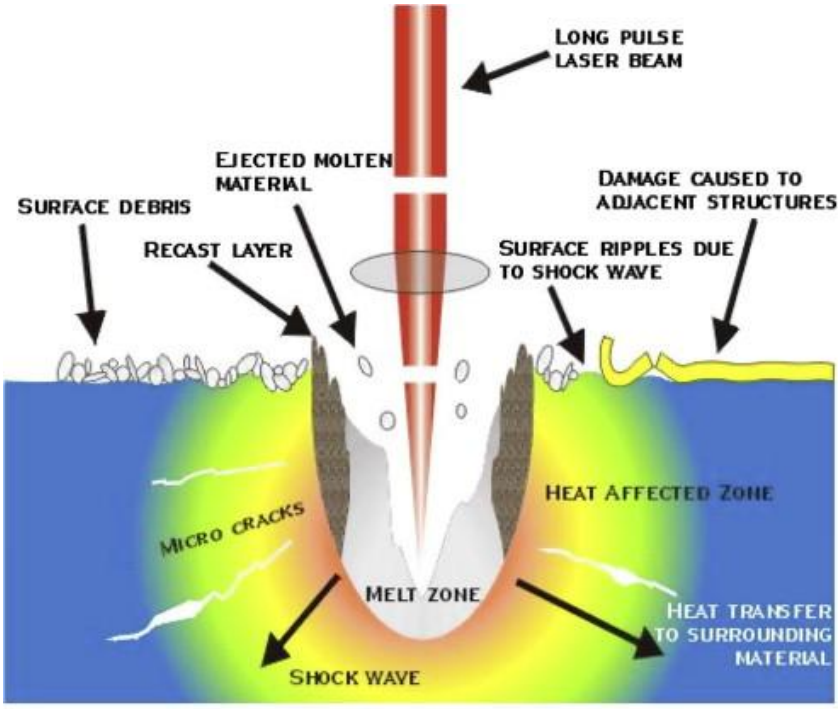

Figure 2.10: Typical laser-material interaction effects with pulses longer than ~10 ns. Depending on the material and the laser pulse not all of these might occur. [51]

In the range from a few nanosecond to several tens of picoseconds most materials behave in a similar way as with longer pulses. The main difference is that the shorter and more intense pulse leads to a faster process and less heat conduction. This often results in higher precision machining.

Some materials behave for nanosecond pulse lengths already like others for pico- or femtosecond pulses. The parameter that is responsible for the behaviour of the material is the electron cooling time which will be discussed in more detail in the next section.

The boundaries between the processes are not only given by the pulse length but also by the specific material that is being machined. For every material the processing parameters, the processing regime and the terms used to describe the behaviour are different. A further parameter that is often used to compare the type of processing is the so called heat affected zone. This is the volume of the material that shows a change from its original structure, density or chemical composition, after laser

processing. The term heat affected zone usefully describes the influence that a laser pulse can have on material that is not removed. Nanosecond laser pulses often show a heat affected zone although it is significantly smaller than that of longer laser pulses.

2.3.5 Ultrashort pulsed laser processes

As mentioned in the previous section the definition of an ultrashort laser pulse is somewhat difficult and in the literature many different terms and time scales are given. The best way for the application of micromachining to classify a laser pulse as ultrashort is by the interaction it has with a material. If the laser pulse is shorter than the electron cooling time, the pulse is an ultrashort laser pulse [52]. This means that the heat transfer from the laser pulse to the material is as short as it can get. Hence the ablation of metals achieved with ultrashort pulses is often referred to as cold ablation, although some heat transfer will occur. In dielectrics, however, the laser pulse excites electrons out of chemical bonds, these electrons are removed from the material and the bonds are broken. The positively charged ions that are left remaining will repel each other and leave the material in a coulomb explosion. This process in dielectrics is cold ablation. For a better understanding an idealized drawing of the ultrashort pulsed laser material interaction is shown in Figure 2.11 . In reality some heating still occurs although it is not always caused by the laser pulse, there can be indirect heating from the hot plume above the machining surface. In many cases however very good results with no or minimal heat influence can be achieved by appropriately selected parameters.

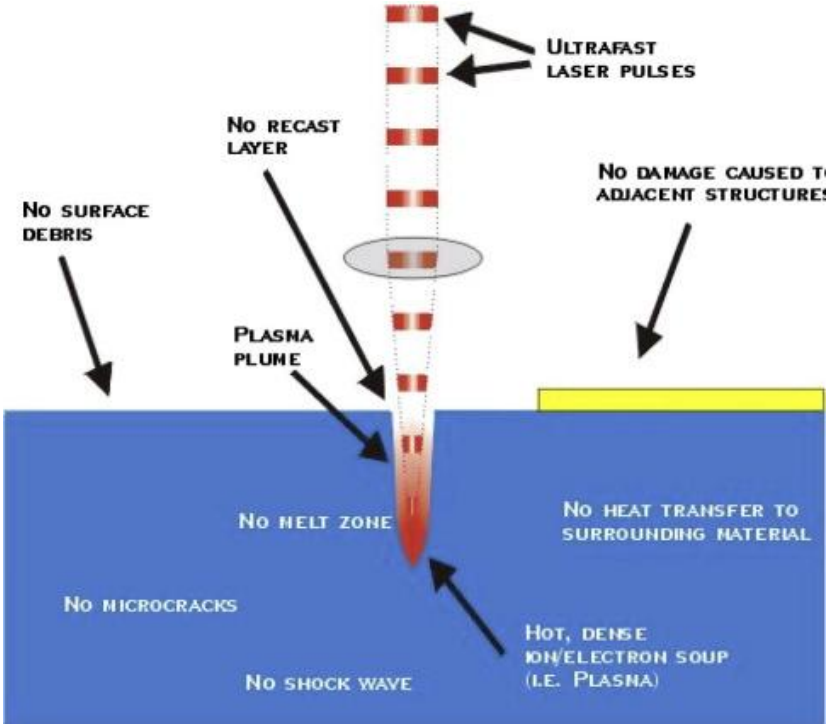

Figure 2.11: Idealized ultrashort pulse laser material interaction. In most cases there is no melting and no heat-affected zone is visible. [51]

The opposite is true as well, it is also possible to achieve melting when using ultrashort pulses, in particular as a result of thermal accumulation of high repetition rate pulses. Some results of this heat effect can cause interesting features such as: bubbles inside glass, densification of the material or nanogratings inside the glass [53, 54]. These effects can be used for interesting processes such as laser induced birefringence, waveguide writing, welding of glasses and to generate voids inside glass. However all of these features are best shown when machining at or below ablation threshold.

2.3.6 Short and ultrahort laser pulse sources

To generate ultrashort laser pulses several different techniques are available. Some of these are explained in this section with an emphasis on the thin disk type laser that was used to generate the picosecond laser pulses that are used in the experimental chapters.

Ultrashort laser pulses are not a recent invention, indeed femtosecond lasers have been used in research, specifically for spectroscopy, since the early 1970's. Hoewever these lasers had either low repetition rates or low pulse energies. Applications were hence very limited. Recent developments, however, enabled high energy and high repetition rate lasers emitting ultrashort laser pulses. To get into this regime, similarly to the development with CO_2, the heat generated from the gain medium has to be transported away. A major shortcoming of the early lasers was how to avoid the build up of heat inside the gain medium. In a rod type laser the heat generated inside the gain medium itself cannot be extracted through heat conduction fast enough therefore three possibilities exist: i) Form a disk out of the gain medium this way the heat can be extracted much more efficiently, this type is called a thin disk laser [55]; ii) A very long, thin gain medium is used as in fibre lasers; iii) A slab laser uses a thin slab of gain material and the laser passes through the longitudinal axis of the slab and is reflected several times through the same slab. All three types of lasers are highly discussed in the laser applications field. Often the fibre laser is the preferred choice as fibres can be manufactured fairly easily and the entire laser can be build without any bulk optics. At laser customer sites a fibre laser can be plugged into an existing fibre delivery system making a replacement in case of a problem very easy. However the highest energy pulses cannot be generated in very thin fibres as the high intensities reach the damage limit of the fibre end face. To avoid damage the diameter of the fibre can be increased but this may result in multimode operation. The thin disk laser similar to the fibre laser overcomes the heat conduction problem by reducing one of the dimensions. Because the absorption of pump light in a thin disk is very low a special pump design which lets a single pump beam pass several times through the gain medium achieves efficient pumping. A typical pump setup of a thin disk laser is shown in Figure 2.12. The laser cavity of a thin disk laser is formed by bulk optics.

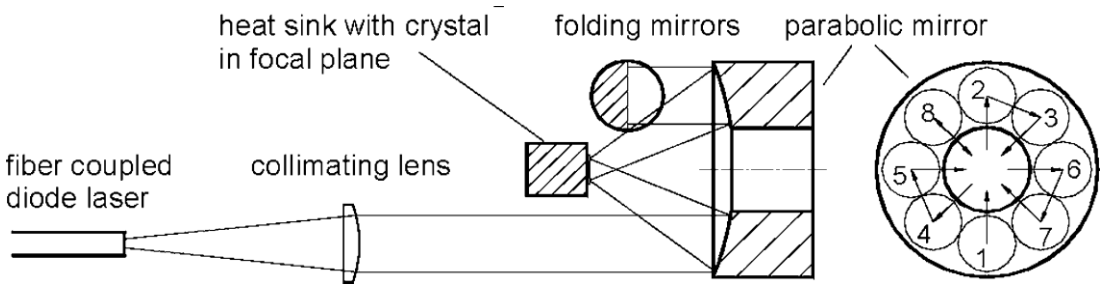

Figure 2.12: The parabolic mirror mounted in a thin disk type laser focuses the pump beam onto the thin disk laser crystal, which is mounted on the heat sink[55].

In a slab laser the laser light passes several times through the same slab but through different areas of the gain medium, cooling is very efficient because the large top and bottom surfaces can be cooled the gain medium can be kept very thin which allows efficient heat removal [56-58]. The thin disk laser type is used in the experimental picosecond laser processing station in this thesis, with more details given later in **Section XXX**

All of the arrangements mentioned above are very good at amplifying an existing laser pulse. A laser pulse in the range of pico- to femtoseconds, however, has to be generated first. This can be achieved with a technique called mode locking. A short pulse is generated by locking several modes of a laser onto each other. This means that the modes of the laser instead of randomly oscillating independent of each other have a fixed phase relationship. This leads to the case where the modes will all interfere constructively with one another hence producing a laser pulse of very high intensity. This will occur periodically. There are two techniques to achieve this:

(i) By actively mode locking the laser using an acousto optic modulator[59] or an electro optic modulator.

(ii) By passively mode locking the laser through a change of the material in the cavity, which can be a Kerr lens effect [60] or a saturable absorber [61].

Passive mode locking can achieve the shorter pulse lengths and is also the preferred technique because it does not require high cost electronics. A gain medium that is ideal because it is self modelocking is Ti:Sapphire. It has also a very broad emission spectrum that is important for the shortest pulses. Similarly fibres are ideal for the production of femtosecond lasers because the either Ytterbium or Erbium doped fibres also have a very broad spectrum. A femtosecond fibre oscillator can be built, also used as a seeding laser in amplifier systems.

Laser systems that use modelocking to generate ultrashort laser pulses often have very high repetition rates, in order to achieve high pulse energies it is necessary to reduce the repetition rate to allow more time for the gain medium to recover and achieve a more efficient amplification of the laser pulse. Since ultrashort pulse oscillators typically provides pulses at rates between 10 MHz and 10 GHz, a pulse picker is used to reduce the repetition rate or select certain pulses or pulse trains. A pulse picker in most cases is an electro optic or acousto optic modulator, driven with a frequency suitable for selection of the desired pulses.

The subsequent amplification can in some cases be done with an ultrashort pulse throughout the entire system, but amplification to the extremely high intensities is not possible lasers as the damage thresholds of the gain medium would be reached. In such cases these limitations can be overcome by stretching the pulse, amplifying it and compressing it again. The technique is called chirped pulse amplification (CPA) [62].

With these developments kW average powers of femotosecond laser pulses are possible [63] and repetition rates of MHz are often achieved. This however leads to further problems. The problem with high repetition rates is moving the laser beam across the work piece fast enough to achieve optimum processing conditions. The build up of heat is not always wanted and also the efficiency drops when a successive laser pulse is shielded by the plasma and plume that is still evident after the first laser pulse. This can be used in some cases for specialized applications such as welding of glasses [64, 65].

Ultra-short laser pulses offer interesting possibilities because they have extreme intensities and enable novel processing regimes. At such short time scales "cold" ablation is possible, where the remaining (unmachined) material does not see any heat during or after the laser pulse.

Commercial lasers with pulses in the gigawatt range are available. These high peak powers often come at the expense of repetition rate and this limits throughput. Recent developments in slab amplifiers show promise to deliver high pulse energy and high repetition rates. One such laser system with two amplifiers has been reported to provide fs pulses at an average power of 1.1 kW with a repetition rate of 20 MHz [63]. Possible applications were shown when a 400 W slab laser was used to manufacture printing rolls [66].

2.3.7 Ablation

The main processing regime that is examined in chapter 3 and 4 is ablation. Ablation is material removal and usually used in the sense of photo-thermal or photo-chemical interactions. The process that is mainly discussed in this research work is so called "cold" ablation, an explanation of this was already given in section 2.3.5. The process is strongly dependent on the material, to be machined. Research showed evidence of melting effects at the edge of laser machined areas even with femtosecond laser pulses. When high repetition rates are used without an appropriately high scanning speed, heat accumulation can occur in the material.

Pulses in the short femtosecond range are very difficult to control as they tend to stretch when passing through optics because parts of the laser beam have to pass a larger amount of material and hence arrive before other parts of the beam, e.g. when passing through a microscope objective a 9 fs pulse is stretched to 62 fs, a factor larger than 6 [67], admittedly a microscope objective is a rather extreme optic however this effect is evident for all optics that are not specially designed for such pulses.

To ablate material two methods are possible, one is to break the chemical bonds immediately through the energy that is carried in the photons and the other is through a very short thermal shock. When processing thin films the thermal shock regime is used, it produces stress between two layers, one layer is quickly removed through the stress build up at the interface. This technology is used in laser induced forward transfer (LIFT) [68, 69]. Many materials can be processed this way: however metals, are the most common materials for LIFT. They absorb the laser pulse well and their electronic conductivity is an interesting property that can be utilized in "printing" electronic circuits.

Photo-chemical ablation is the more interesting process because it introduces less or no thermal damage to the material. This type removes material by breaking the chemical bonds causing molecular fragmentation. To break chemical bonds the energy carried by the photon has to match the molecular binding energy. The photon energy is given by equation (2.3) where h is the Planck constant, c is the speed of light and λ is the wavelength of the laser light.

$$E = \frac{h\,c}{\lambda} \qquad \textbf{(2.3)}$$

For example the photons in the UV range with a wavelength between 193 nm and 355 nm have a photon energy between 6.4 eV and 3.5 eV. This exceeds the binding energy of many molecular structures enabling direct photo-chemical processing of these materials with very little heating [70, 71].

It is well known that photo-chemical processes can even occur when the energy of the photons is not sufficient to directly break the bonds [72], provided that the intensity is high enough. This process has been observed with wavelengths into the IR region [73]. It is due to a process called multi-photon absorption, where the simultaneous absorption of several photons reaches the binding energy by combining the energy of all absorbed photons. This enables processing with long wavelengths but also, and this is more important for the purpose of the work presented here,

allows machining of materials with much higher binding energies. A graph showing some materials that can be processed in a multiphoton process with an 800 nm femtosecond laser is shown in Figure 2.13 [74]. Multi photon absorption is a non-linear process and the higher the order (number of photons required) the less likely is the process to happen. Therefore to achieve multi photon absorption the intensity on the target needs to be very high compared to linear absorption. Figure 2.13 shows that the threshold intensities are in the range of 10^{17} W m^{-2}. These high intensities are only possible by strong focussing of very short pulses and are usually confined to a small volume.

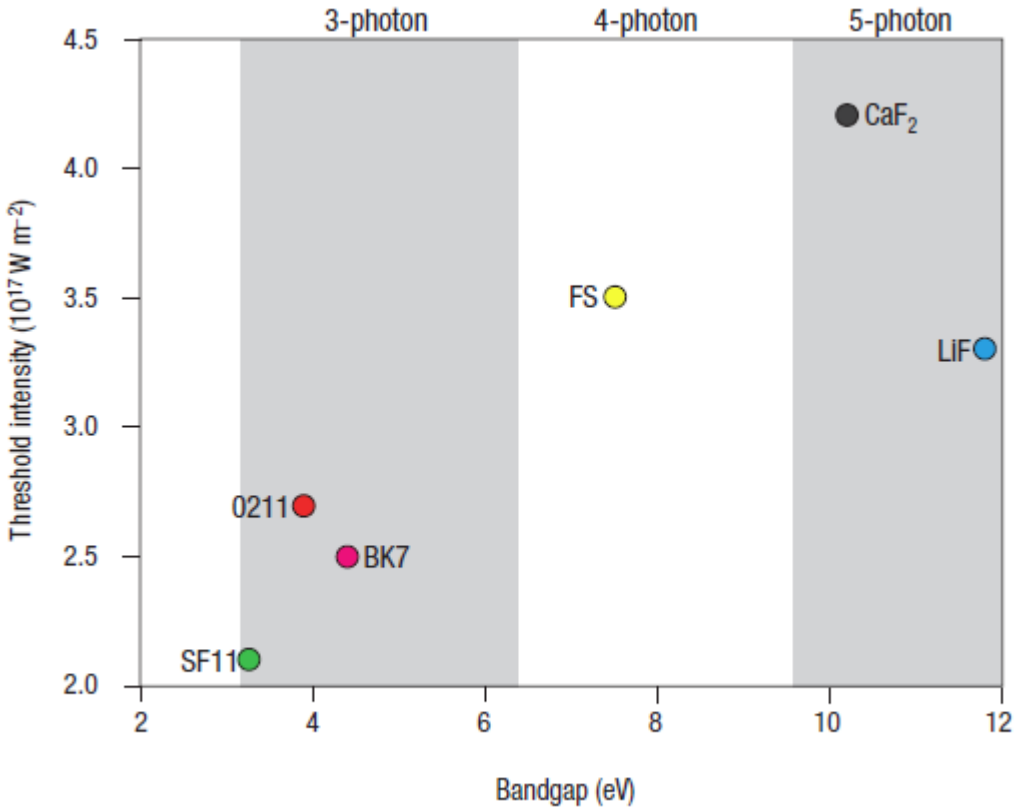

Figure 2.13: Threshold intensity for processing of various transparent materials as a function of the bandgap energy for a laser wavelength of 800 nm and a pulse duration of 100 fs. Ranging through several multi-photon steps [74].

In addition to these very high intensities that are achieved with ultrashort pulsed lasers a major difference in comparison with longer laser pulses for machining is the

timescale of the energy deposition in the material. The atomic relaxation times are in the order of the timescales of the ultrashort laser pulses. This causes many ultrashort laser processes to be photo-thermal and photo-chemical at the same time [75]. Both processing regimes take place but no heat is transferred deeper into the bulk of the material. The majority of the material removal takes place after the laser pulse as the pulses are so short no mechanical movement is possible on the timescale of the laser pulse. In ultrashort laser processing of non-metals the photo-thermal process takes place when the hot matter leaves the machining area and collisions occur. In metals the photo-thermal process can be described as collisions between electrons and phonons causing an increase in heat above the vaporization point, and material is removed through vaporization. During the photo-chemical process in non-metals bonds are broken and the electrons that are then free are excited and finally the atom is ionized by absorbed photons. These free electrons are accelerated and can collide, transfer and ionize further atoms. A so called avalanche ionization process can be started resulting in first electrons leaving the material and pulling ions with them. Du et al found that the avalanche process dominates the ablation of fused silica from nanosecond pulses to femtosecond pulses using the 800 nm wavelength [76]. They also found a strong threshold behaviour as shown in Figure 2.14. Surprisingly almost no change in transmitted energy is observed which indicates that process takes the entire pulse duration to reach threshold behaviour.

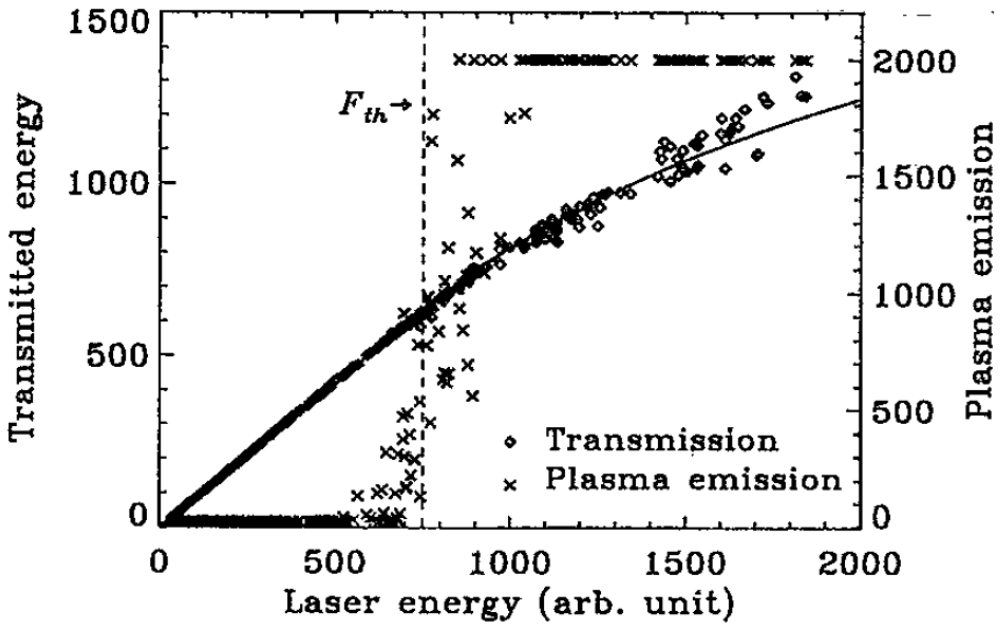

Figure 2.14: Threshold behaviour of plasma emission for a 300 femtosecond laser pulse. Shown is the transmitted energy of the laser pulse and the plasma emission. A strong threshold behaviour is visible for the plasma emission however the transmitted energy does not show this behaviour. [76]

Du et al. also measured the threshold behaviour for different pulse lengths in their work and confirmed the empirical scaling of the threshold following the square root of the pulse duration as shown in equation (2.4).

$$F_{th} \propto \sqrt{t_p} \tag{2.4}$$

In this law F_{th} is the ablation threshold fluence and t_p is the pulse duration. This empirical relationship is true for pulses from long pulse durations to the picosecond range. For shorter pulses the relationship is different, it is better described by (2.5).

$$F_{th} \propto {t_p}^{-1} \tag{2.5}$$

The relationship between pulse length and threshold that *Du et. al.* found is shown in Figure 2.15.

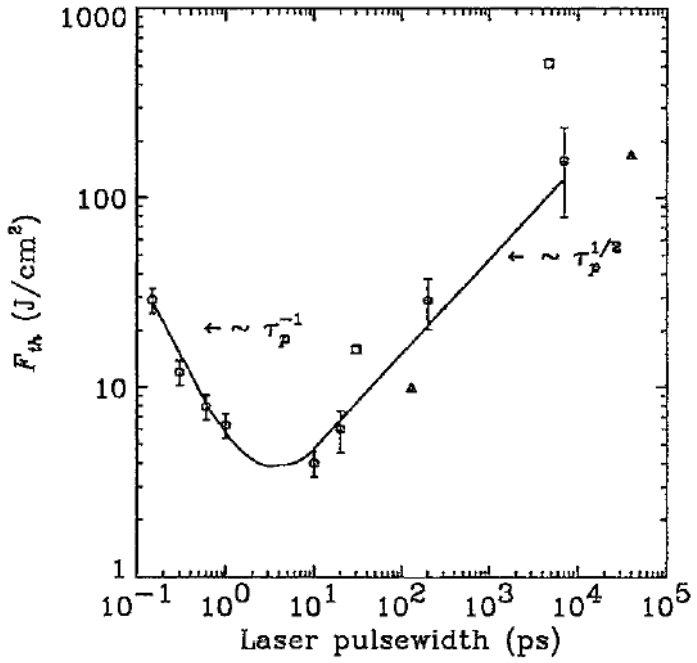

Figure 2.15: Ablation threshold fluence as a function of pulse length for 780 nm wavelength laser light.

Because the focussed ultrashort laser pulse reaches very high intensities it can be used to machine any material. Materials that are difficult to machine with other methods are of particular interest, for example brittle materials such as ceramics or glass. Machining with a single pulse in glass is possible[77], however not very practical. Incubation effects with successive pulses can play a major role and need to be taken into account when laser milling or drilling materials because a single pulse and multiple pulses show very different machining properties and ablation thresholds can drop by as much as a factor of 4 from single pulse to 100 pulses [78].

Ultrafast laser machining of transparent materials is one of the best examples where other manufacturing methods cannot achieve the same results. Alternative (non-laser) methods are extremely slow, like FIB machining (discussed in 2.2.4), or they cannot produce such small features (discussed in 2.2.1 and 2.2.2) or are too

complicated for small volume production, like photolithographic methods (discussed in 2.2.5). One very popular example where machining of transparent samples is desired is the manufacture of microfluidic devices which can be achieved by direct laser machining [79-84]. Microfluidic devices have become increasingly popular in recent years. They offer novel investigation techniques for biological and chemical analysis of specimen with minimal amounts of liquid. They are also often used in research of novel materials they can be used to efficiently mix very small volumes of liquid. While in general microfluidic devices can be build out of many materials, glasses are seldom used because they are difficult to machine, even though they offer advantages such as integration with optical waveguides for sensing.

Direct laser machining of glass microfluidic devices is very attractive. It has some shortcomings: 3-dimensional structures are not possible and the average surface roughness R_a is typically in the range of several 100's of nm. For some applications this is still not sufficient. The flow parameters inside machined channels are influenced by this roughness hence a manufacturing method that can achieve better surface quality is desirable. Such a method is discussed in the next section.

2.3.7.1 Laser induced changes in material properties of transparent materials

A high intensity laser beam that passes through a transparent material can cause changes of the material properties without any immediately visible damage or ablation of the material. The change of material properties depends on the strength of the interaction and can be either an increase or decrease in density of the material. The creation of these structures can be due to the plasma generation in the focal volume causing an explosive expansion [85]. The different densities also change the local refractive index. This allows some interesting applications such as waveguide writing [74, 86]. By scanning the tightly focused spot three dimensional waveguides can be written into the material. Waveguides written into the bulk of glasses have many applications they can be used as fan outs for optical fibres or to establish lab-on-a-chip devices with photonic based addressing and many more applications in integrated optics. Another application idea for laser written refractive index changes

is the manufacture of three dimensional optical data storage which was first demonstrated in 1996 by Glezer et al.[87].

The writing of waveguides and the introduction of material changes without material removal cannot be considered micromachining. However the density change enables the micro manufacture of complicated structures through preferential etching of the exposed parts of the material [54, 88]. Using chemicals such as hydrofluoric acid that usually etch glass slowly rates that are more than a hundred times faster than normal were found [54, 89]. This preferential etching can be used to machine completely arbitrary structures almost without any limitation to the geometry inside fused silica and other glasses with a feature size only slightly larger than 1 µm [90]. It is especially suitable for narrow channels through the material. Because the unexposed material is etched during the process even though at a much slower rate than the exposed material a taper occurs. This can be compensated for by exposing a larger volume the deeper into the material the structure gets. The process relies on very tight focussing of weak laser pulses (100-300 nJ) compared to direct ablation. The tight focussing requires microscope objectives and high precision stages for sample positioning. A higher intensity would cause a bigger damage site and therefore reduce the minimum feature size. The speed at which such a structure is written is usually very slow (~200 μms^{-1}) because highest precision is required. The following etching step is however much slower with etching rates in the order of a few µm/min [91]. It is obvious that etching of deep structures is slow, however etching of large areas and multiple parts at once in parallel is possible, providing high material removal rates, strongly dependant on the geometry that is being produced.

The exposure and etching technique is particularly useful when more expensive equipment like FIB is not available or when true three dimensional microstructures are required. These are not possible with any other manufacturing technique.

References

1. R. Rahnama, M. Sajjadi, and S. Park, "Chatter suppression in micro end milling with process damping," Journal of Materials Processing Technology **209**, 5766-5776 (2009).
2. C. R. Friedrich, and M. J. Vasile, "Development of the micromilling process for high-aspect-ratio microstructures," J Microelectromech S **5**, 33-38 (1996).
3. C. R. Friedrich, P. J. Coane, and M. J. Vasile "Micromilling development and applications for microfabriaction" Microelectronic Engineering 35, 367-372 (1997).
4. A. Perveen, M. P. Jahan, M. Rahman, and Y. S. Wong, "A study on microgrinding of brittle and difficult-to-cut glasses using on-machine fabricated poly crystalline diamond (PCD) tool," Journal of Materials Processing Technology **212**, 580-593 (2012).
5. E. Brousseau, S. Dimov, and D. Pham, "Some recent advances in multi-material micro- and nano-manufacturing," Int J Adv Manuf Technol **47**, 161-180 (2010).
6. J. Gan, X. Wang, M. Zhou, B. Ngoi, and Z. Zhong, "Ultraprecision Diamond Turning of Glass with Ultrasonic Vibration," Int J Adv Manuf Technol **21**, 952-955 (2003).
7. K. Foy, Z. Wei, T. Matsumura, and Y. Huang, "Effect of tilt angle on cutting regime transition in glass micromilling," Int J Mach Tool Manu **49**, 315-324 (2009).
8. W. Pei, Z. Yu, J. Li, C. Ma, W. Xu, X. Wang, and W. Natsu, "Influence of Abrasive Particle Movement in Micro USM," Procedia CIRP **6**, 551-555 (2013).
9. H. Zarepour, and S. H. Yeo, "Single abrasive particle impingements as a benchmark to determine material removal modes in micro ultrasonic machining," Wear **288**, 1-8 (2012).
10. T. B. Thoe, D. K. Aspinwall, and M. L. H. Wise, "Review on ultrasonic machining," International Journal of Machine Tools and Manufacture **38**, 239-255 (1998).
11. H. Wensink, J. W. Berenschot, H. V. Jansen, and M. C. Elwenspoek, "High resolution powder blast micromachining," in *Micro Electro Mechanical Systems, 2000. MEMS 2000. The Thirteenth Annual International Conference on*(2000), pp. 769-774.
12. E. Belloy, A. Sayah, and M. A. M. Gijs, "Powder blasting for three-dimensional microstructuring of glass," Sensors and Actuators A: Physical **86**, 231-237 (2000).
13. E. Belloy, S. Thurre, E. Walckiers, A. Sayah, and M. A. M. Gijs, "The introduction of powder blasting for sensor and microsystem applications," Sensors and Actuators A: Physical **84**, 330-337 (2000).
14. Y. Hiromasa, S. Koji, H. Shigehiko, and T. Osamu, "Micropowder blasting with nanoparticles dispersed polymer mask for rapid prototyping of glass chip," Journal of Micromechanics and Microengineering **15**, 1236 (2005).
15. D. Solignac, A. Sayah, S. Constantin, R. Freitag, and M. A. M. Gijs, "Powder blasting for the realisation of microchips for bio-analytic applications," Sensors and Actuators A: Physical **92**, 388-393 (2001).

16. F. Han, L. Chen, D. Yu, and X. Zhou, "Basic study on pulse generator for micro-EDM," Int J Adv Manuf Technol **33**, 474-479 (2007).
17. C. Ferri, A. Ivanov, and A. Petrelli, "Electrical measurements in μ-EDM," Journal of Micromechanics and Microengineering **18**, 085007 (2008).
18. S. Di, X. Chu, D. Wei, Z. Wang, G. Chi, and Y. Liu, "Analysis of kerf width in micro-WEDM," International Journal of Machine Tools and Manufacture **49**, 788-792 (2009).
19. Y. Jeong, B. HanYoo, H. Lee, B. Min, D. Cho, and S. Lee, "Deburring microfeatures using micro-EDM," Journal of Materials Processing Technology **209**, 5399-5406 (2009).
20. S. Reyntjens, and R. Puers, "A review of focused ion beam applications in microsystem technology," Journal of Micromechanics and Microengineering **11**, 287-300 (2001).
21. Y. Fu, and K. A. B. Ngoi, "Focused ion beam direct fabrication of micro-optical elements: features compared with laser beam and electron beam direct writing," in *Innovation in Manufacturing Systems and Technology (IMST)*(2004).
22. B. Geil, "Focused-Ion-Beam Material Removal Rates," U. S. A. R. Laboratory, ed. (U.S. Army Research Laboratory, DEFENSE TECHNICAL INFORMATION CENTER, 1993).
23. R. Puers, and S. Reyntjens, "Fabrication and testing of custom vacuum encapsulations deposited by focused ion beam direct-write CVD," Sensor Actuat a-Phys **92**, 249-256 (2001).
24. T. Dai, X. Kang, B. Zhang, J. Xu, K. Bao, C. Xiong, and Z. Gan, "Study and formation of 2D microstructures of sapphire by focused ion beam milling," Microelectron Eng **85**, 640-645 (2008).
25. D. Iannuzzi, K. Heeck, M. Slaman, S. de Man, J. H. Rector, H. Schreuders, J. W. Berenschot, V. J. Gadgil, R. G. P. Sanders, M. C. Elwenspoek, and S. Deladi, "Fibre-top cantilevers: design, fabrication and applications," Meas Sci Technol **18**, 3247-3252 (2007).
26. Y. Q. Fu, and B. K. A. Ngoi, "Investigation of diffractive-refractive microlens array fabricated by focused ion beam technology," Opt Eng **40**, 511-516 (2001).
27. Ampere A. Tseng, "Recent developments in micromilling using focused ion beam technology," Journal of Micromechanics and Microengineering **14**, R15-R34 (2004).
28. W. X. Li, G. Lalev, S. Dimov, H. Zhao, and D. T. Pham, "A study of fused silica micro/nano patterning by focused-ion-beam," Appl Surf Sci **253**, 3608-3614 (2007).
29. T. H. Maiman, "Stimulated Optical Radiation in Ruby," Nature **187**, 493-494 (1960).
30. A. L. Schawlow, and C. H. Townes, "Infrared and Optical Masers," Physical Review **112**, 1940-1949 (1958).
31. A. Javan, W. R. Bennett, Jr., and D. R. Herriott, "Population Inversion and Continuous Optical Maser Oscillation in a Gas Discharge Containing a He-Ne Mixture," Phys Rev Lett **6**, 106-110 (1961).
32. N. B. Dahotre, and S. P. Harimkar, *Laser fabrication and machining of materials*, Chapter 3 (Springer, 2008).

33. Z. J. Kiss, and R. J. Pressley, "Crystalline solid lasers," Proceedings of the IEEE **54**, 1236-1248 (1966).
34. A. J. Demaria, W. H. Glenn, Jr., M. J. Brienza, and M. E. Mack, "Picosecond laser pulses," Proceedings of the IEEE **57**, 2-25 (1969).
35. D. Schuöcker, *Handbook of the EuroLaser Academy* (Chapman & Hall, 1998).
36. L. Lazov, and N. Angelov, "Physical model about laser impact on metals and alloys," Contemporary Materials **1**, 2 (2010).
37. K. Ujihara, "Reflectivity of metals at high temperatures," Journal of Applied Physics **43**, 2376-2383 (2003).
38. W. M. Steen, and J. Mazumder, "Basic Laser Optics," in *Laser Material Processing*(Springer London, 2010), pp. 79-130.
39. M. Lax, "Temperature rise induced by a laser beam," Journal of Applied Physics **48**, 3919-3924 (1977).
40. "Corning SMF-28 Optical Fibre Product Information," (Corning Incorporated, USA, 2002).
41. A. K. Pandey, and A. K. Dubey, "Taguchi based fuzzy logic optimization of multiple quality characteristics in laser cutting of Duralumin sheet," Opt Laser Eng **50**, 328-335 (2012).
42. D. J. Thomas, M. T. Whittaker, G. W. Bright, and Y. Gao, "The influence of mechanical and CO2 laser cut-edge characteristics on the fatigue life performance of high strength automotive steels," Journal of Materials Processing Technology **211**, 263-274 (2011).
43. P. Fischer, N. Karapatis, V. Romano, R. Glardon, and H. P. Weber, "A model for the interaction of near-infrared laser pulses with metal powders in selective laser sintering," Appl Phys A **74**, 467-474 (2002).
44. J. P. Kruth, L. Froyen, J. Van Vaerenbergh, P. Mercelis, M. Rombouts, and B. Lauwers, "Selective laser melting of iron-based powder," Journal of Materials Processing Technology **149**, 616-622 (2004).
45. E. C. Santos, M. Shiomi, K. Osakada, and T. Laoui, "Rapid manufacturing of metal components by laser forming," International Journal of Machine Tools and Manufacture **46**, 1459-1468 (2006).
46. F. J. McClung, and R. W. Hellwarth, "Giant Optical Pulsations from Ruby," Journal of Applied Physics **33**, 828-829 (1962).
47. A. Weck, T. H. R. Crawford, D. S. Wilkinson, H. K. Haugen, and J. S. Preston, "Laser drilling of high aspect ratio holes in copper with femtosecond, picosecond and nanosecond pulses," Appl Phys A **90**, 537-543 (2008).
48. T. M. Shao, M. Hua, H. Y. Tam, and E. H. M. Cheung, "An approach to modelling of laser polishing of metals," Surface and Coatings Technology **197**, 77-84 (2005).
49. A. Lamikiz, J. A. Sánchez, L. N. López de Lacalle, and J. L. Arana, "Laser polishing of parts built up by selective laser sintering," International Journal of Machine Tools and Manufacture **47**, 2040-2050 (2007).
50. E. Brinksmeier, O. Riemer, A. Gessenharter, and L. Autschbach, "Polishing of Structured Molds," CIRP Annals - Manufacturing Technology **53**, 247-250 (2004).

51. B. Fernández, F. Claverie, C. Pécheyran, and O. F. X. Donard, "Direct analysis of solid samples by fs-LA-ICP-MS," TrAC Trends in Analytical Chemistry **26**, 951-966 (2007).
52. B. N. Chichkov, C. Momma, S. Nolte, F. Alvensleben, and A. Tünnermann, "Femtosecond, picosecond and nanosecond laser ablation of solids," Appl Phys A **63**, 109-115 (1996).
53. Y. Bellouard, A. A. Said, M. Dugan, and P. Bado, "Femtosecond Laser Micromaching: Photonic and Microfluidic Devices in Transparent Materials," Top Appl Phys **123**, 443-465 (2012).
54. C. Hnatovsky, R. S. Taylor, P. P. Rajeev, E. Simova, V. R. Bhardwaj, D. M. Rayner, and P. B. Corkum, "Pulse duration dependence of femtosecond-laser-fabricated nanogratings in fused silica," Applied Physics Letters **87**, - (2005).
55. A. Giesen, and J. Speiser, "Fifteen Years of Work on Thin-Disk Lasers: Results and Scaling Laws," IEEE Journal of Selected Topics in Quantum Electronics **13**, 598-609 (2007).
56. K. Du, N. Wu, J. Xu, J. Giesekus, P. Loosen, and R. Poprawe, "Partially end-pumped Nd:YAG slab laser with a hybrid resonator," Optics Letters **23**, 370-372 (1998).
57. A. Faulstich, H. J. Baker, and D. R. Hall, "Face pumping of thin, solid-state slab lasers with laser diodes," Optics Letters **21**, 594-596 (1996).
58. B. J. Comaskey, R. Beach, G. Albrecht, W. J. Benett, B. L. Freitas, C. Petty, D. VanLue, D. Mundinger, and R. W. Solarz, "High average powers diode pumped slab laser," Quantum Electronics, IEEE Journal of **28**, 992-996 (1992).
59. R. A. Coppock, and E. D. Reed (1982), "Acousto-optic mode-locked laser," The US Patent and Trademark Office **US19800155985**.
60. T. Brabec, C. Spielmann, P. Curley, and F. Krausz, "Kerr lens mode locking," Optics Letters **17**, 1292-1294 (1992).
61. H. A. Haus, "Theory of mode locking with a fast saturable absorber," Journal of Applied Physics **46**, 3049-3058 (1975).
62. P. Maine, D. Strickland, P. Bado, M. Pessot, and G. Mourou, "Generation of ultrahigh peak power pulses by chirped pulse amplification," IEEE J. Quantum Electronics, **24**, 398-403 (1988).
63. P. Russbueldt, T. Mans, H.-D. Hoffmann, and R. Poprawe, "1100 W Yb:YAG femtosecond Innoslab amplifier," Proc. SPIE 7912, Solid State Lasers XX: Technology and Devices, (2011), pp. 79120R-79120R-79129.
64. I. Miyamoto, A. Horn, J. Gottmann, D. Wortmann, and F. Yoshino, "Fusion Welding of Glass Using Femtosecond Laser Pulses with High-repetition Rates," Journal of Laser Mirco / Nanoengineering **2**, pp 57-63.
65. T. Tamaki, W. Watanabe, and K. Itoh, "Laser micro-welding of transparent materials by a localized heat accumulation effect using a femtosecond fiber laser at 1558 nm," Opt Express **14**, 10460-10468 (2006).
66. K. Du, "Ultrakurzpulslaser mit 400 W Leistung," in *Laser+Photonik*, Carl Hanser Verlag, (2011), pp. 58-59.
67. N. R. Tadepalli, D. Alexander, D. Doerr, J. Li, and H. Zhang, "Femtosecond pulse stretching in microscope objectives used for micro/nanomachining," J Laser Appl **17**, 270-272 (2005).

68. H. Gerhard, D. Matthias, K. Jan, S. Sebastian, S. Jürgen, and P. H. Heinz, "Laser lift-off initiated by direct induced ablation of different metal thin films with ultra-short laser pulses," Journal of Physics D: Applied Physics **45**, 315303 (2012).
69. S. Al Tarazi, D. Batani, Y. Al Hadithi, R. Jafer, L. Antonelli, B. Vodopivec, M. Vitobello, and M. Iqbal, "Laser-induced forward transfer (LIFT) of material using ablation of thin films," Radiation Effects and Defects in Solids **165**, 501-508 (2010).
70. Y. G. Yingling, and B. J. Garrison, "Photochemical ablation of organic solids," Nuclear Instruments and Methods in Physics Research Section B: Beam Interactions with Materials and Atoms **202**, 188-194 (2003).
71. A. Vogel, and V. Venugopalan, "Mechanisms of Pulsed Laser Ablation of Biological Tissues," Chemical Reviews **103**, 577-644 (2003).
72. M. Göppert-Mayer, "Über elementarakte mit zwei quantensprüngen," Annalen der Physik **401**, 273-294 (1931).
73. R. DeSalvo, A. A. Said, D. J. Hagan, E. W. Van Stryland, and M. Sheik-Bahae, "Infrared to ultraviolet measurements of two-photon absorption and n_2 in wide bandgap solids," IEEE J. Quantum Electronics, **32**, 1324-1333 (1996).
74. R. R. Gattass, and E. Mazur, "Femtosecond laser micromachining in transparent materials," Nat Photon **2**, 219-225 (2008).
75. K. Sugioka, M. Meunier, and A. Piqué, *Laser precision microfabrication* (Springer, 2010).
76. D. Du, X. Liu, G. Korn, J. Squier, and G. Mourou, "Laser-induced breakdown by impact ionization in SiO2 with pulse widths from 7 ns to 150 fs," Applied Physics Letters **64**, 3071-3073 (1994).
77. S. Campbell, F. C. Dear, D. P. Hand, and D. T. Reid, "Single-pulse femtosecond laser machining of glass," Journal of Optics A: Pure and Applied Optics **7**, 162 (2005).
78. D. Ashkenasi, M. Lorenz, R. Stoian, and A. Rosenfeld, "Surface damage threshold and structuring of dielectrics using femtosecond laser pulses: the role of incubation," Appl Surf Sci **150**, 101-106 (1999).
79. L. Shah, J. Tawney, M. Richardson, and K. Richardson, "Femtosecond laser deep hole drilling of silicate glasses in air," Appl Surf Sci **183**, 151-164 (2001).
80. M. S. Giridhar, K. Seong, A. Schülzgen, P. Khulbe, N. Peyghambarian, and M. Mansuripur, "Femtosecond pulsed laser micromachining of glass substrates with application to microfluidic devices," Appl Optics **43**, 4584-4589 (2004).
81. D. M. Karnakis, M. R. H. Knowles, K. T. Alty, M. Schlaf, and H. V. Snelling, "Comparison of glass processing using high repetition femtosecond (800nm) and UV (255nm) nanosecond pulsed lasers," Microfluidics, BioMEMS, and Medical Microsystems III **5718**, 216-227 (2005).
82. S. Nikumb, Q. Chen, C. Li, H. Reshef, H. Y. Zheng, H. Qiu, and D. Low, "Precision glass machining, drilling and profile cutting by short pulse lasers," Thin Solid Films **477**, 216-221 (2005).
83. R. An, Y. Li, Y. Dou, D. Liu, H. Yang, and Q. Gong, "Water-assisted drilling of microfluidic chambers inside silica glass with femtosecond laser pulses," Appl Phys A **83**, 27-29 (2006).

84. D. Schafer, E. A. Gibson, E. A. Salim, A. E. Palmer, R. Jimenez, and J. Squier, "Microfluidic cell counter with embedded optical fibers fabricated by femtosecond laser ablation and anodic bonding," Opt Express **17**, 6068 (2009).
85. S. Vukelić, P. Kongsuwan, and Y. L. Yao, "Ultrafast Laser Induced Structural Modification of Fused Silica—Part I: Feature Formation Mechanisms," Journal of Manufacturing Science and Engineering **132**, 061012-061012 (2010).
86. S. Nolte, M. Will, J. Burghoff, and A. Tuennermann, "Femtosecond waveguide writing: a new avenue to three-dimensional integrated optics," Appl Phys A **77**, 109-111 (2003).
87. E. N. Glezer, M. Milosavljevic, L. Huang, R. J. Finlay, T. H. Her, J. P. Callan, and E. Mazur, "Three-dimensional optical storage inside transparentmaterials," Optics Letters **21**, 2023-2025 (1996).
88. Y. Bellouard, A. Said, M. Dugan, and P. Bado, "Fabrication of high-aspect ratio, micro-fluidic channels and tunnels using femtosecond laser pulses and chemical etching," Opt Express **12**, 2120-2129 (2004).
89. Z. Y. Dong, S. Z. Zou, Z. H. Han, H. J. Yu, L. Sun, W. Hou, X. C. Lin, and J. M. Li, "High power, high energy nanosecond pulsed fiber amplifier with a 20-μm-core fiber," Laser Phys **21**, 536-539 (2011).
90. A. Marcinkevicius, S. Juodkazis, M. Watanabe, M. Miwa, S. Matsuo, H. Misawa, and J. Nishii, "Femtosecond laser-assisted three-dimensional microfabrication in silica," Optics Letters **26**, 277-279 (2001).
91. X. Yu, Y. Liao, F. He, B. Zeng, Y. Cheng, Z. Xu, K. Sugioka, and K. Midorikawa, "Tuning etch selectivity of fused silica irradiated by femtosecond laser pulses by controlling polarization of the writing pulses," Journal of Applied Physics **109**, 053114-053115 (2011).

Chapter 3: Laser machining of two transparent materials: fused silica and sapphire

An example where laser processing has major advantages over conventional machining methods, or in fact is the only way to machine the material in a reliable and precise way, is the machining of transparent materials. Many glasses are hard and brittle; therefore machining methods like milling with conventional rotating tools is not very precise and causes cracking or in the recently developed ductile machining regime is slow. The main problem with machining with conventional milling is that the tool wear is very high, breakage within the tools is very difficult to detect and machining rates are very low. In general most methods have very low machining rates. For industrial processes, however, the machining rate can be a main factor influencing the cost of a part. The recent developments in microfluidics and the application of optic sensing on these devices requires transparent materials to be machined efficiently. As this technique evolves from laboratory manufacture into a commercialised system and on to industrial production, machining rates will be a main factor of cost reduction. In this chapter we investigate machining of fused silica and sapphire, using the nanosecond and picosecond laser.

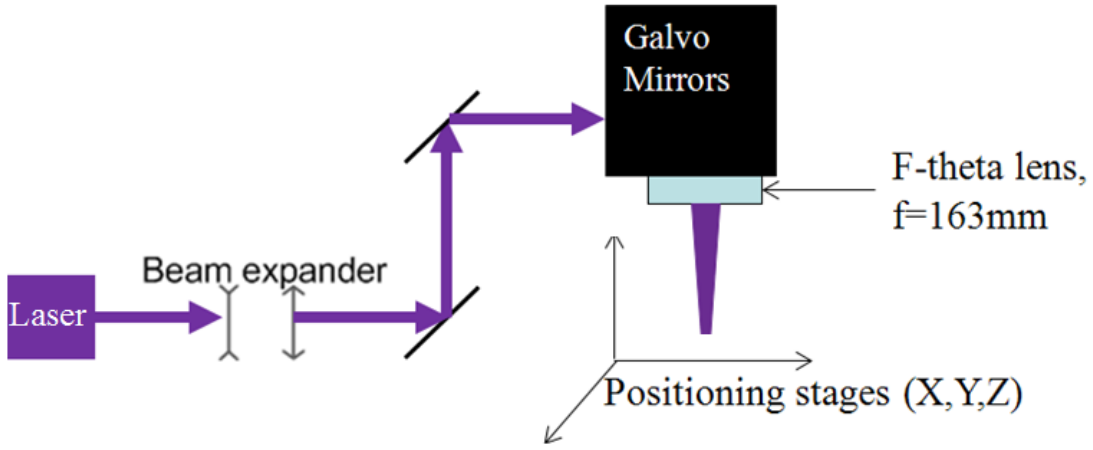

Figure 3.1: Schematic drawing of the laser machining setup used in this thesis. Each wavelength 343 nm, 515 nm, and 1030 nm had separate beam paths that followed the same schematic.

A schematic drawing of the laser setup that was used is shown in Figure 3.1. The laser that is used throughout this thesis is a Trumpf TruMicro 5050 3C. The laser is a thin disk type laser (Section 2.3.6). The fundamental wavelength of the laser is 1030 nm and it emits laser pulses of 125 µJ pulse energy that are 6 ps long. The maximum possible pulse repetition rate is 400 kHz. The energy of the laser pulse is independent of the repetition rate because the laser internally always operates at the same repetition rate. A repetition rate lower than 400 kHz can be selected by using the software 'TruMicro Control' supplied by the manufacturer. The fundamental wavelength can be converted into 515 nm (green) and 343 nm achieving an average power of 30 W and 12 W respectively. The energy selection is done through the same software, it is done in percent of the maximum power in the 1030 nm wavelength which is internally linearized. Because the efficiency of frequency conversion changes with input energy the energy relationship in 515 nm and 343 nm is not linear, a calibration for these wavelength was done, measuring the average power and dividing it by the repetition rate. The error of the pulse energy is related to the error of the power measurement which is estimated to be 0.5 W, the error of the pulse energy is smaller than 2 µJ.

Each wavelength that the laser can emit has its own output window therefore providing three different beam paths. All optics that are used are with a wavelength specific coating hence it is necessary to provide thee separate beam paths which run through the same basic components shown in Figure 3.1. The active wavelength can be selected through the laser software.

The laser beam is expanded to match the aperture of the galvanometer scan head. The laser beam diameter before expansion is 5 mm in each wavelength. The galvanometer scan head for 343 nm has an aperture of 14 mm, the two for 515 nm and 1030 nm have an aperture of 10 mm. Each galvanometer scan head is equipped with a 160 mm f-theta lens, that allows scanning of an 90 mm by 90 mm with a scanning speed of up to 3000 mms^{-1}.

The samples that are machined are mounted on a precision x-y-z linear table, with a position repeatability better than 10 µm. The sample is brought into focus by this stage system. The best focal position is found by stepping a sample through different z-positions and measuring the size of the damage crater on the sample. A reference microscope is then mounted at a fixed position and used to observe the position and repeatability of the laser machined craters.

When machining was carried out the laser beam was scanned across the work piece using the galvanometer scan heads (chapter 3 and chapter 4). For measurements of the damage crater size the beam was stationary and the sample was stepped using the positioning tables (section 3.3.1 and section 3.4.1). For measurements of the spot size the laser beam was stationary and the knife edge was scanned through the beam with the XY-table.

The beam size at the focal plane was measured using a knife edge method. In this method a sharp edge is mounted on the XY table, and translated through the laser beam. A power meter that is placed underneath the knife edge is used to measure power. The knowledge of the recorded power profile (Figure 3.2(a)) can be transferred to an intensity profile (Figure 3.2(b)) by building the derivative. A

Gaussian fit to this profile is applied to achieve a better estimate of the laser spot size. The estimated e^{-2}-width of this profile is 7 µm. It is worth noting that the error on this measurement is fairly large because it relys on several factors, the positioning accuracy of the knife edge, the accuracy of the power measurement and the possibility of power fluctuations of the laser. The positioning accuracy has probably the largest error, as the table manufacturer's specifications are an error of 500 nm for each table direction. In our case the stages are stacked and therefore the error is larger than that of a single stage. The error of the beam width is ± 2 µm. Giving a spot size of 7± 2 µm at 343 nmSimilar measurements were carried out for 1030 nm and 515 nm wavelength with the result of 30 µm ± 2 µm for 1030 nm and 16 µm ± 2 µm for 515 nm.

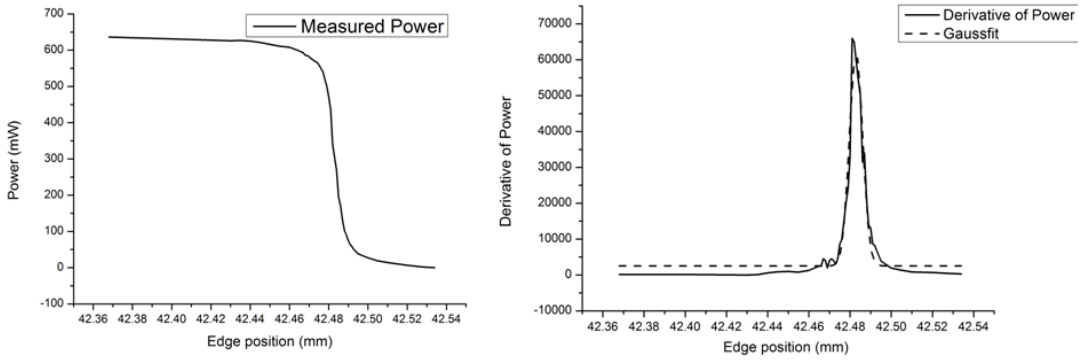

Figure 3.2: Measurement of the laser power when a knife edge is translate through the laser beam as a function of knife position; and the derivative of this function showing the beam profile.

3.2 Determining ablation thresholds

The principle that is used was established by Liu et al. [2]. It relies on the intensity profile that the laser beam has on the work piece. Liu et al. have investigated the ablation threshold behaviour and found a relationship between the damaged spot diameter and the fluence profile [2]. Assuming a Gaussian spot the spatial fluence profile Φ(r) on the sample is given by Equation (3.1).

$$\Phi(r) = \Phi_0 \, e^{\frac{-2r^2}{w_0^2}} \qquad \textbf{(3.1)}$$

With a peak fluence of Φ_0 and a Gaussian beam waist of w_0, r is the radial distance from the centre of the laser spot. The peak fluence and the pulse energy are related through Equation (3.2).

$$\Phi_0 = \frac{2\,E_P}{\pi\,w_0^2} \qquad \textbf{(3.2)}$$

It can then be shown that the diameter, D, of the damaged crater and the threshold fluence have the relationship shown in Equation (3.3). Instead of the peak fluence throughout this thesis the average fluence was used because in most of the comparable literature the average fluence is used. The average fluence is defined as half the peak fluence.

$$D^2 = 2\,w_0^2 \ln\left(\frac{\Phi_0}{\Phi_{th}}\right) \qquad \textbf{(3.3)}$$

A plot of the squared diameter of the ablation craters as a function of fluence should therefore show a logarithmic dependency, obviously the area of a damaged crater can be used as well, but this is much more difficult to measure than the diameter. From equation (3.3) we can also derive the beam waist radius w_0 through the slope of the regression curve. This can be used to calculate the e^{-2} area of the laser spot, and this can be used to calculate the fluence, because the energy of a laser pulse is much easier to measure than its fluence. The values that are measured easiest are the average laser power, from which the energy can be calculated; and the diameter of the damage crater.

When multiple successive pulses hit the same area on the sample of course this model does not work as well. This is because an effect called incubation or energy

accumulation occurs. The effect that can have two different causes, in many cases it is called energy accumulation when the effect is caused by generated heat, where successive pulses interact with the material at a different temperature. The case of an incubation effect appears when statistical defects are more likely to occur with successive pulses. Basically the first pulses cause a non observable change of the material and at some point the damage occurs. In addition, the damage threshold of already damaged material is significantly lower than that of a material in pristine condition. It is however not certain that both of these effects are observable on their own, and in many cases a combination of both is what is actually taking place. The literature uses two different models to describe the threshold behaviour, the probabilistic damage threshold model and the defect accumulation model. The accumulation behaviour of a material can be explained by an incubation model [3]. The ablation threshold fluence for a number, N, of laser shots is related to the single shot ablation threshold by equation (3.4). [4, 5]

$$\Phi_{\mathrm{th}}(\mathrm{N}) = \Phi_{\mathrm{th}}(1)\, \mathrm{N}^{S-1} \tag{3.4}$$

The incubation coefficient S is a measure of the incubation behaviour. There are several forms of incubation which are often related to heat accumulation but can also be a change that is caused by heat like densification of the material. For a factor of S=1 there is no incubation effect. This damage accumulation behaviour model is called the probabilistic model. The second model that is frequently used to describe damage thresholds and the accumulation behaviour of several pulses is the so called exponential defect accumulation model. This model is based on the observation that even for an infinite amount of pulses there is a intensity requirement to cause damage. The formula is slightly different to equation (3.4), as the number of pulses is in the exponent as well as an incubation factor and a saturation level is used as well. This model is described by equation (3.5). [6-8]

$$\Phi_{\mathrm{th}}(\mathrm{N}) = \left(\Phi_{\mathrm{th}}(1) - \Phi_{\mathrm{th}}(\infty)\right) \mathrm{e}^{-\mathrm{k}(\mathrm{N}-1)} + \Phi_{\mathrm{th}}(\infty) \tag{3.5}$$

In this case the incubation factor is k, and at k = 0 there is no accumulative behaviour. The values of the threshold fluence $\Phi_{th}(\infty)$ and $\Phi_{th}(1)$ are for single and for an infinite number of pulses respectively. The theory that is plotted in Figure 3.7 is called the probabilistic defect accumulation model. It is inaccurate for large number of pulses because it does not reach a saturation level. The exponential defect accumulation model which is calculated by equation (3.5) takes this saturation into account. A saturation level should be reached because for very low fluences even a very large number of pulses does not necessarily cause damage. A plot of the exponential defect accumulation model is shown in Figure 3.8.

3.3 Machining fused silica

3.3.1 Picosecond laser ablation thresholds for fused silica

To find ablation thresholds a pattern, easily programmed using available software, was machined into fused silica. It consists of several spots with sufficient separation to prevent any cross-talk, in this case a distance of 100 µm. The pulse energy and therefore the fluence was changed in steps of 2 % of the full output laser energy. The steps of 2% are for the 1030 nm wavelength which is controlled internally, this is a linearized and measured system. In the other wavelengths the output power is not linear because the frequency doubling and tripling are nonlinear processes.

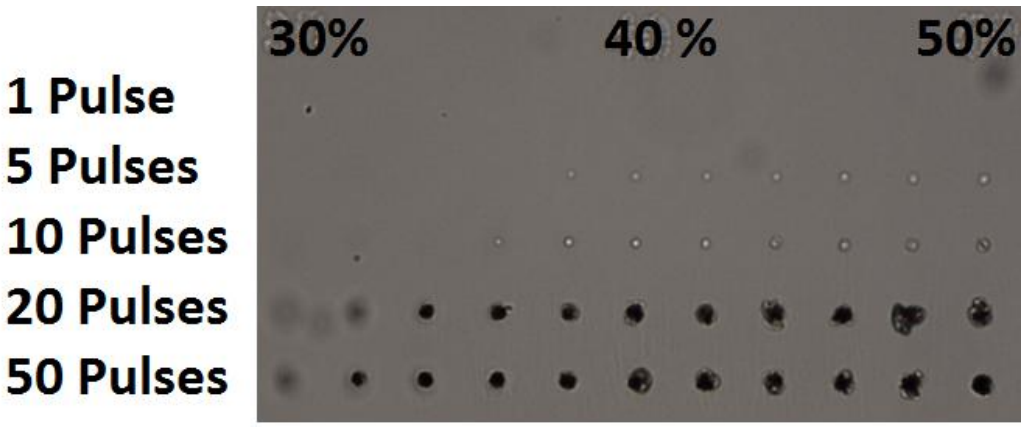

Figure 3.3: Microscope image of an ablation threshold map containing pulses from 30% to 50% of the available pulse energy in UV. The map contains craters for 1, 5, 10, 20, 50 laser pulses. The craters from the single ablation threshold are not visible because they are too shallow to be resolved by the optical microscope.

Maps, such as the one shown in Figure 3.3 were machined for an extended range of energies, with a separate map for each wavelength. Instead of measuring the diameter of the crater, the area was measured and the diameter calculated. To measure the area a light microscope (Leica DM6000 B) with a differential interference contrast method was used. The system has an optical resolution better than 1 µm. Equipped with a high resolution camera and computer software for processing of images. A contrast border can be set by which the software decides what area to measure. These measurements do still have an error that is estimated to be less than 20 μm^2. This method works well for low fluence measurements however when cracking occurs the measurement of the area is often large because whole chunks of material are removed. Therefore the error can only be estimated, I estimate the error of D^2 to be 50 μm^2. The error on fluence is dominated by the error made in the beam waist measurements in section 3.1. The measurement of the pulse energy is much more accurate as the repetition rate and average power measurements have only a very small error. The error on pulse energy is estimated to be less than 1 % whilst the error of the spot size measurements at 343 nm is 29 %, at 515 nm it is 13 % and at 1030 nm it is 7%.

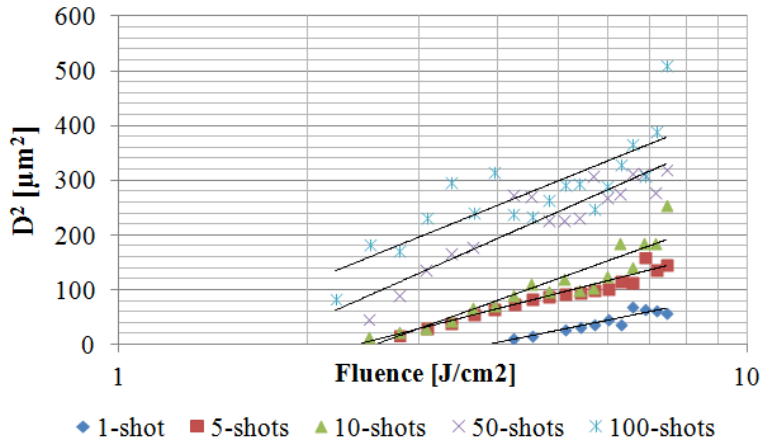

Figure 3.4: Plot of squared crater diameter as a function of fluence for fused silica, machined with 343 nm. The shift of the ablation threshold is clearly visible from single to multiple shots. The beam waist w_0 of 7 µm was used for calculations. Solid lines represent a least square fit.

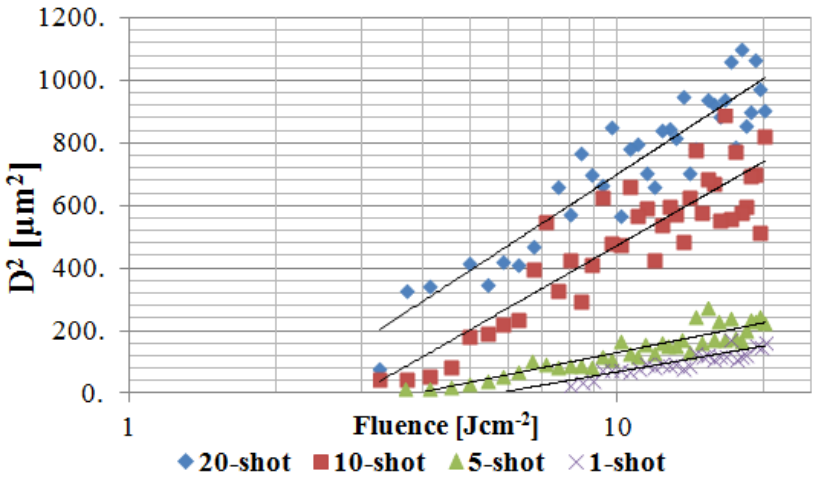

Figure 3.5: Plot of the squared diameter of the damage craters in fused silica machined with the 515 nm wavelength as a function of the fluence. The measured beam waist for the 515 nm wavelength is 16 µm. Solid lines represent a least square fit.

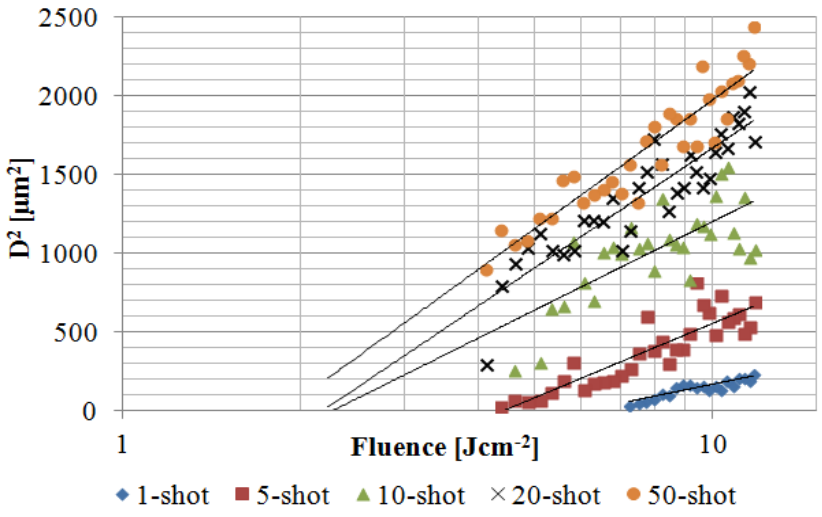

Figure 3.6: Plot of the squared diameter of the ablation craters machined with 1030 nm laser pulses in fused silica as a function of the fluence. The beam waist w_0 in IR is 30 µm which was independently measured in section 3.1. Solid lines represent a least square fit.

The plot of the damage thresholds in UV is shown in Figure 3.4. It is clearly visible that the damage craters are bigger for higher fluences, and for increasing number of pulses. The shift towards lower ablation thresholds for a higher number of pulses is also obvious; it is due to the accumulation behaviour. The ablation threshold for single pulses in UV is $F_{Th,1} = 3.7 \pm 1.1$ Jcm^{-2} decreasing to $F_{Th,100} = 1.1 \pm 0.3$ Jcm^{-2} for 100 successive pulses on the same spot, the error was calculated by error progression of the errors discussed earlier. The ablation threshold values for the other wavelengths are higher. For the 515 nm wavelength the ablation threshold for single pulses is 5.8 ± 0.8 Jcm^{-2} and the accumulation behaviour introduces an even more significant decrease down to 1.9 ± 0.3 Jcm^{-2} for 50 pulses. The 1030 nm wavelength shows very similar values to the 515 nm wavelength. The single pulse ablation threshold is at 6.0 ± 0.5 Jcm^{-2} and the 50 pulse threshold is 1.9 ± 0.2 Jcm^{-2}. The development of the ablation thresholds is shown in Figure 3.7. The solid lines shown in Figure 3.7 are modelled according to equation (3.4), using an accumulation factor of S = 0.75, which provides a good fit to the experimental data.

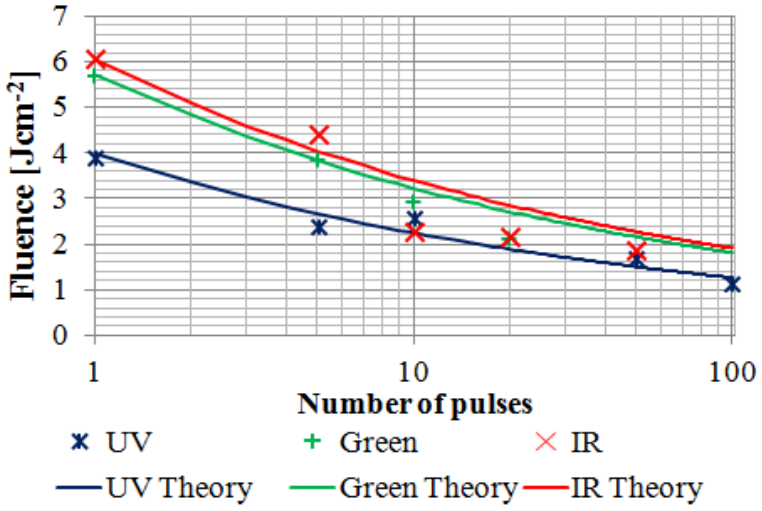

Figure 3.7: Development of the ablation thresholds for the wavelengths 1030 nm, 515 nm, 343 nm. The solid lines represent the accumulation behaviour according to the probabilistic defect accumulation model according to equation (3.4).

Figure 3.7 and Figure 3.8 show the two different models that can be used to model ablation threshold dependence on the number of pulses. Which are modelled according to equations (3.4) and (3.5).

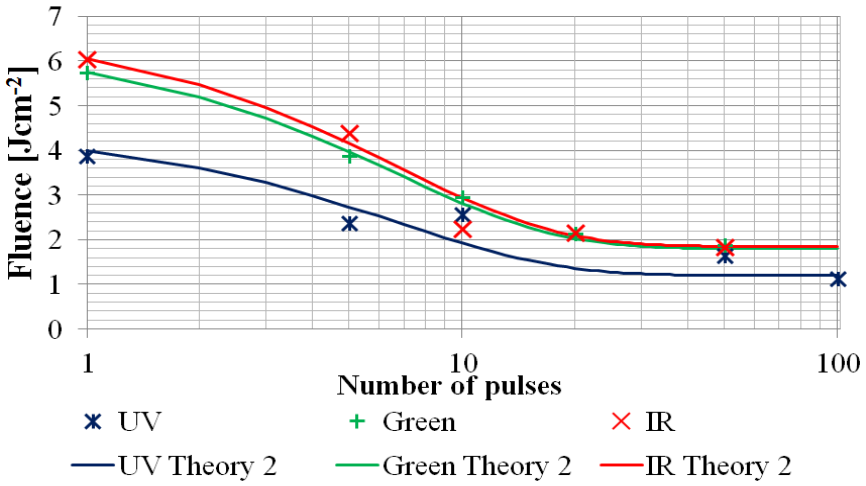

Figure 3.8: Damage threshold measurements vs the number of laser pulses incident on the sample. The Lines represent the development of the thresholds according to the exponential defect accumulation model which is represented by equation (3.5).

The exponential defect accumulation model describes our case slightly better, but the differences are small. Especially for the 515 nm wavelength and the 1030 nm wavelength the exponential defect accumulation model matches the experimental data very closely the average deviation is just 0.1 Jcm^{-2} for 515 nm compared to 0.3 Jcm^{-2} for the probabilistic model. In IR the average deviation is 0.32 Jcm^{-2} for the exponential and 0.65 Jcm^{-2} for the probabilistic damage threshold model. In UV the average deviation is smaller for the probabilistic model with 0.21 Jcm^{-2} and 0.38 Jcm^{-2} for the exponential model. The saturation level is already reached after roughly 20 pulses. The difference in ablation thresholds between the wavelengths and between multiple pulses can have major influences on the strategy of micromilling.

3.3.2 Material removal rates

The ablation rates and the efficiencies are very important factors in order to optimize a laser process or to make a decision on what laser source is required for a particular process. The results presented in section 3.3.1 above indicate that there should be a change in removal rate with a change in spot overlap. The spot overlap is one of the main factors that can be changed in order to optimize the laser milling strategy, including material removal rates and surface quality of the machined surfaces. It is the result of a combination of the scanning speed and the repetition rate, as shown in Figure 3.9. The spot-to-spot displacement is calculated by dividing the scanning speed by the repetition rate. A typical example is a scanning speed of 100 mms^{-1} and a repetition rate of 40 kHz which will result in a spot-to-spot displacement of 2.5 µm. This value is of limited use when comparing different wavelengths with different spot diameters. To improve the comparability the factor of spot overlap is introduced. It is calculated according to equation (3.6) with spot spacing d_S and spot radius w as shown in Figure 3.9. The line overlap can be calculated with the same formula replacing the spot-to-spot distance d_s with the line spacing d_L.

$$\text{spot overlap} = \left(1 - \frac{d_s}{2w}\right) \times 100\% \quad \textbf{(3.6)}$$

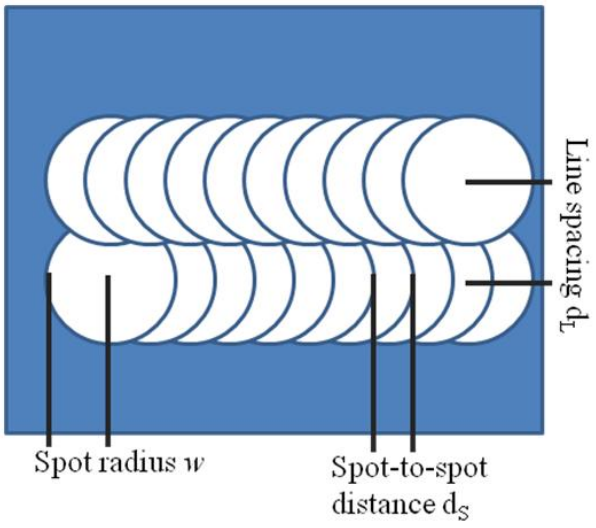

Figure 3.9: Laser scanning strategy to scan the laser beam in parallel lines across the sample. Also showing the important terms of line spacing and spot spacing to calculate spot overlap.

To determine the material removal rates ramps are machined into the sample. Each ramp consists of several lines close to each other with constant spot and line overlap. Every 75 µm the energy is increased. This allows a specific energy value to be assigned to every location and depth that was machined. The surface roughness is also higher than the step height, therefore determining single steps is impossible. Out of these ramps a number of factors can be found, not only is it possible to determine the machining threshold and material removal rate at that particular spot overlap, it is also possible to calculate the efficiency of material removal. Ablation rates were calculated by dividing the machined depth by the time it takes to scan the beam over a 1 mm^2 area. Figure 3.10(a) shows a model of the material removal ramps. A machined ramp is shown in Figure 3.10(b). The machined depth profile was measured with a Dektak 3000 surface profilometer. A plot of the machined depth is shown in Figure 3.10(c). Ramps were machined with each wavelength for different spot overlap values, achieved by different scanning speeds and therefore different processing times. The scan speeds that were used are 10 mms^{-1}, 40 mms^{-1},

100 mms^{-1}, 250 mms^{-1}, 400 mms^{-1} and in some cases also 200 mms^{-1} and 300 mms^{-1}. This was to get a closer match in spot overlap values; because each wavelength has a different spot diameter the spot overlap is different when using the same scanning speed.

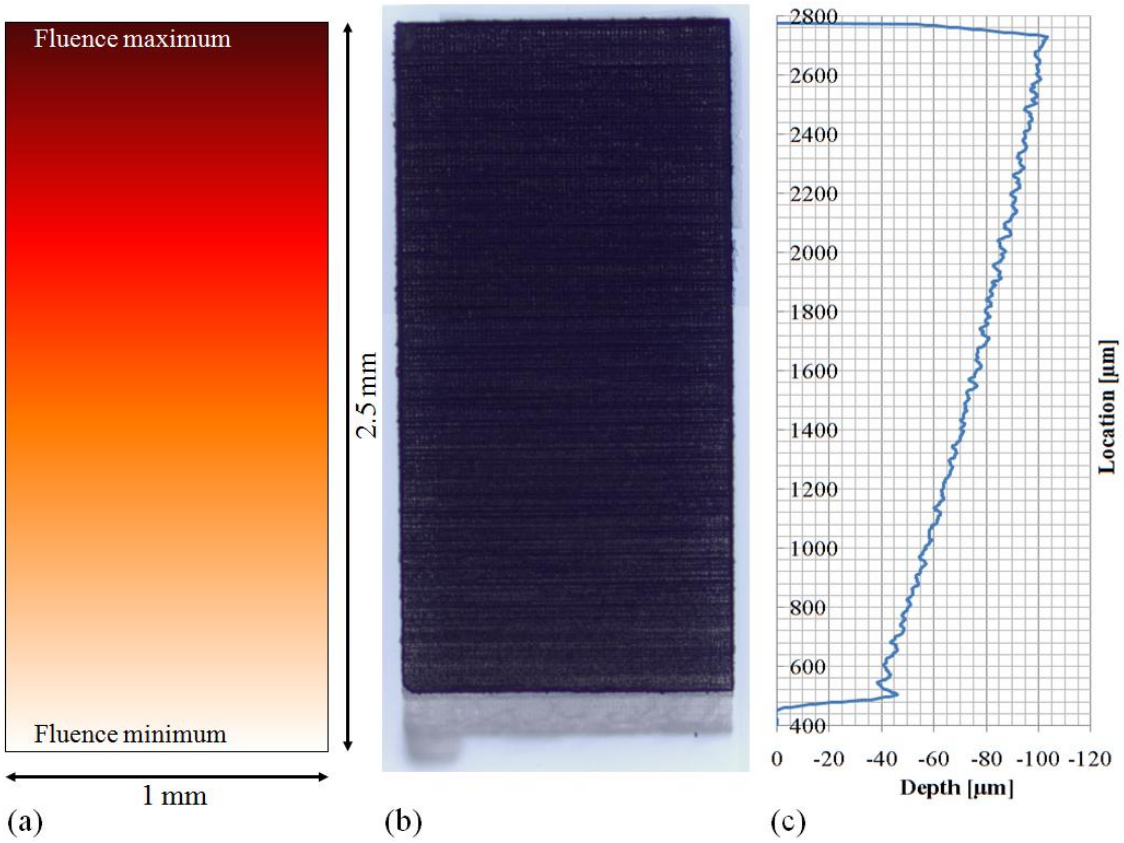

Figure 3.10: (a) theoretical idea of the ramp, linear increase in fluence machining a depth map; (b) machined depth ramp the laser was scanned in lines from left to right; clearly visible is the machining threshold, and the machining below the threshold and below the still intact surface in the picture at the bottom; (c) the actual machined depth profile showing the ramp and the level of roughness.

A comparison between the scanning speeds is not particularly useful, hence we calculated the corresponding spot overlaps and compared these. A plot of the material removal rates for the 1030 nm wavelength is shown in Figure 3.11, for 515 nm in Figure 3.12 and for 343 nm in Figure 3.13. The general trend is as expected; the higher the fluence the higher the removal rate. The increase in removal rate is not linear with fluence, however this is also expected as the depth

that can be removed by a single pulse also does not increase linearly. This was clearly shown in the ablation threshold studies in section 3.3.1. The shift in machining threshold can also be seen. As we would expect as less pulses are interacting at lower spot overlap values the accumulation effect is lower and the threshold increases. It is however more complex than just comparing the spot overlap values because also the line overlap has an influence on the machining thresholds as is discussed later in this section. The line spacing used for these graphs is 3 µm.

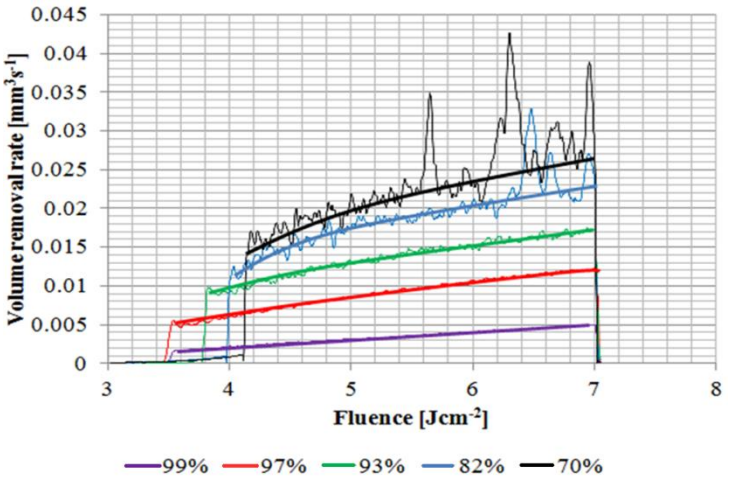

Figure 3.11: 1030 nm removal rates for spot overlap values from 99% to 70%. The thin lines show the machined profile, while the thick lines represent the general trend as a visual guideline.

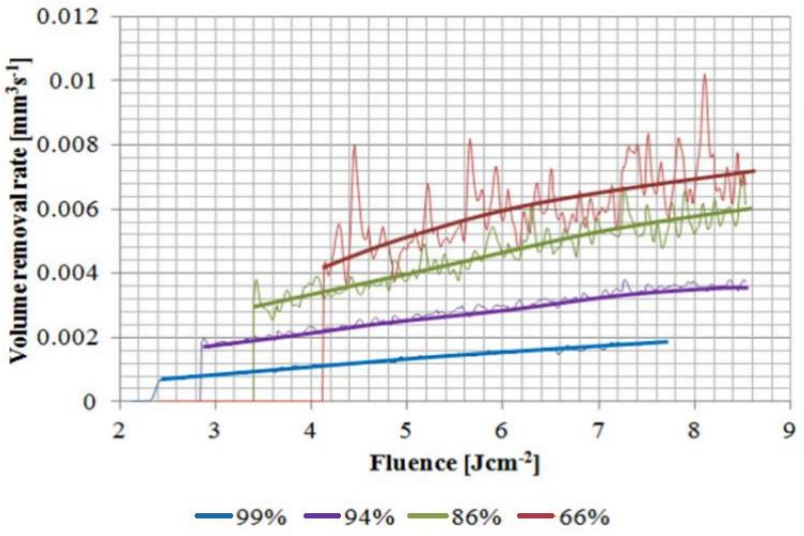

Figure 3.12: Removal rates with the 515 nm wavelength for spot overlaps between 99% and 66%. The thick lines show the trend and thin lines the machined profiles.

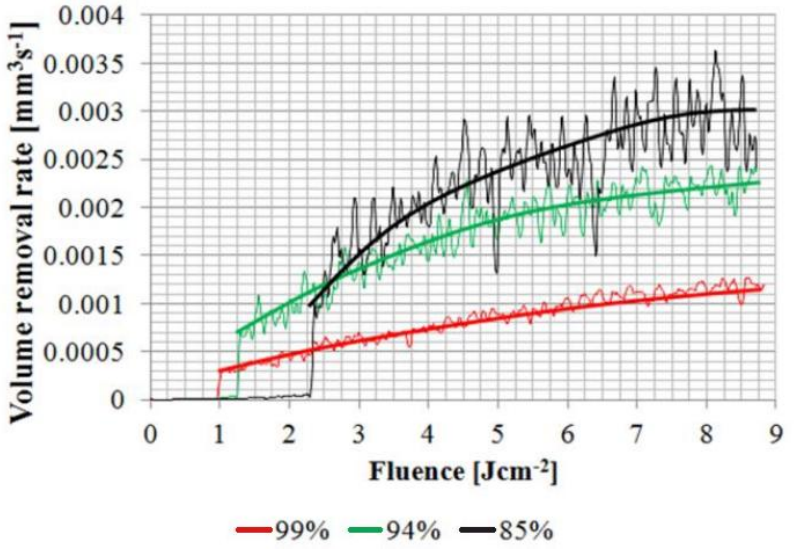

Figure 3.13: Removal rates achieved with the 343 nm wavelength. The thick lines show the trend and thin lines the machined profiles.

In Figure 3.11 the removal rates for 1030 nm are shown. The machining threshold for the highest spot overlap value is 3.5 Jcm^{-2} which is higher than the threshold that was found for a corresponding number of successive pulses on the same spot in the ablation threshold testing. A spot overlap of 99% in the IR relates to more than 400 pulses interacting with each other. The machining threshold shifts to 4.2 Jcm^{-2} for a

70% spot overlap. For the 515 nm wavelength this shift is even larger, for a spot overlap of 66% we get a machining threshold at a fluence of 4.1 $Jcm^{-2}$and a much lower value of 2.4 Jcm^{-2} for a 99% spot overlap. These values are very close to the values we would expect from the ablation threshold measurements. At 343 nm we also see a shift from 2.2 Jcm^{-2} at 85% spot overlap to 1.0 Jcm^{-2} at 99% spot overlap. These values again are in close agreements with the ablation threshold measurements. In all cases the increase in removal rate is not linear with increasing fluence, as expected because the efficiency usually decreases with increasing fluence.

	pulses	1030 nm		515 nm		343 nm
stationary	1	6,00 J/cm²		5,90 J/cm²		3,90 J/cm²
beam	5	4,50 J/cm²		3,90 J/cm²		2,40 J/cm²
	10	2,20 J/cm²		2,90 J/cm²		2,60 J/cm²
	20	2,10 J/cm²		2,10 J/cm²		
	50	1,90 J/cm²		1,90 J/cm²		1,80 J/cm²
	100					1,10 J/cm²
moving beam	**Spot overlap**	**1030 nm**	**Spot overlap**	**515 nm**	**Spot overlap**	**343 nm**
	99%	3,50 J/cm²	99%	2,40 J/cm²	99%	1,00 J/cm²
	97%	3,50 J/cm²	94%	2,80 J/cm²	94%	1,20 J/cm²
	93%	3,80 J/cm²	86%	3,40 J/cm²	85%	2,20 J/cm²
	82%	4,00 J/cm²	66%	4,10 J/cm²		
	70%	4,10 J/cm²				

Table 3.1: Summary of different ablation thresholds of fused silica found in the previous sections for the moving beam thresholds a line spacing of 3 µm was used.

The thresholds that were found in this section do show a very close relationship between the moving and the stationary beam although comparison of the thresholds is not easy as the dependency on the two dimensional overlap was not further investigated. It shows however that the thresholds found in both methods the moving beam and the stationary beam are very close to each other. It also shows that for the moving beam a spot overlap related ablation threshold needs to be taken into account, when developing a laser machining process.

3.3.3 Material removal efficiency

The material removal rate is only part of a complete process. In cases where a specific laser source is bought in order to achieve a given goal the removal rate is important but only secondary. In many cases the average power of a laser, especially with ultrashort pulsed laser sources, largely determines its price. In industrial applications it might be preferred to use two lasers in parallel rather than one high average power system. This has many reasons: (i) often two laser sources of lower average power are cheaper than one high average power system; (ii) if one laser needs maintenance the second one can still be used for production; (iii) more flexibility in case of changing demand. We can calculate the efficiency from the material removal rate data that was presented in the previous section 3.3.2. Using this together with a knowledge of the repetition rate and pulse energy we can easily calculate the energy that is necessary to remove a mm^3. For better comparability we compare the different wavelengths at similar spot overlap values, see Figure 3.14.

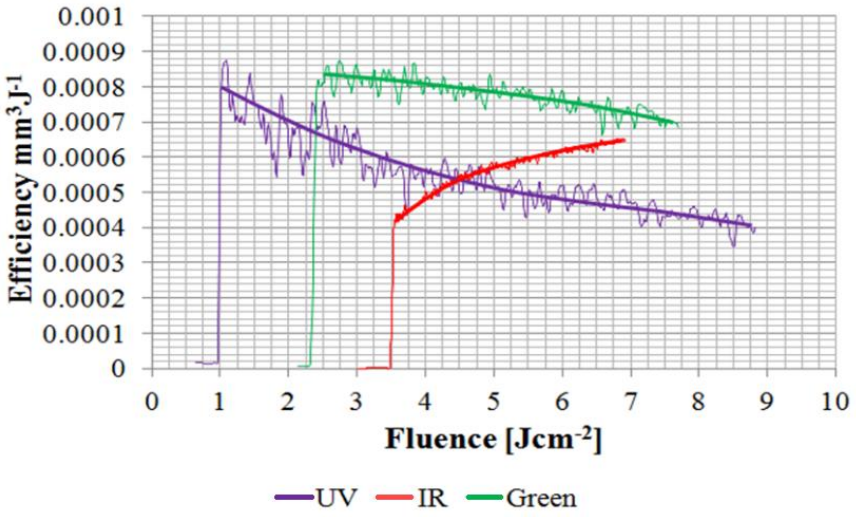

Figure 3.14: Wavelength comparison of removal efficiency for 99% spot overlap.

At a large spot overlap of 99% (Figure 3.14) the maximum removal efficiency is roughly 0.8 $mm^{-3}kJ^{-1}$. The highest efficiency is achieved close to the threshold values. Both the 343 nm wavelength and the 515 nm wavelength have similar maximum values. The 343 nm efficiency drops with increasing fluence to roughly

half its maximum value. The efficiency at the 515 nm wavelength also decreases but at a lower rate than the 343 nm. By contrast at the 1030 nm wavelength the efficiency increases with increasing fluence, however because the maximum efficiency is not reached, it is difficult to judge whether the maximum efficiency is higher or lower than the maximum in green and UV. At the lower pulse overlap of 94% (Figure 3.15) one change is obvious; the efficiency for all wavelengths is almost a factor of 10 higher with a maximum of 6.4 mm^3kJ^{-1}.

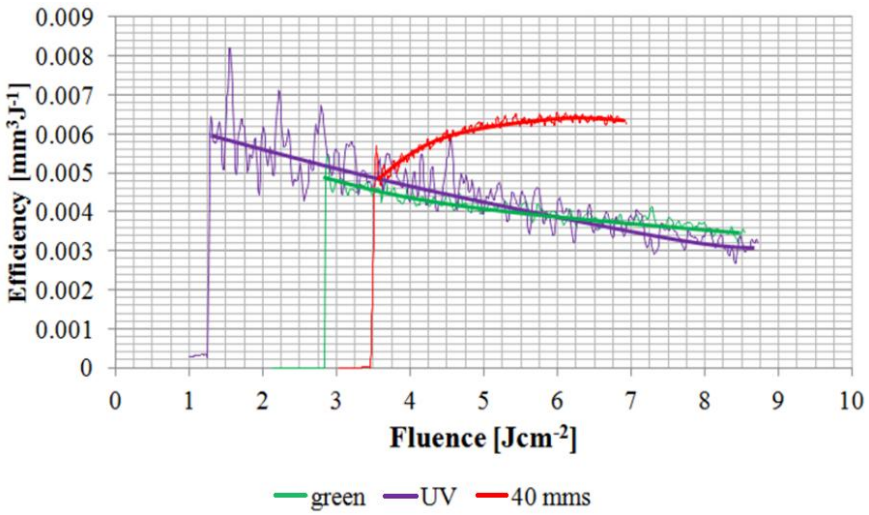

Figure 3.15: Material removal efficiency for a spot overlap of 94%, comparison for three wavelengths.

In this case again the 343 nm and the 515 nm efficiencies are very close to each other and they both show a similar drop to the one shown in the 99% plot (Figure 3.14). Again the efficiency decrease with increasing fluence in green is less than the one in UV. The IR efficiencies show a slightly different behaviour with a non linear increase in removal efficiency from the threshold at 3.5 Jcm^{-2} with an efficiency of 5.0 mm^3kJ^{-1} to the maximum of 6.4 mm^3kJ^{-1} at a fluence of roughly 6 Jcm^{-2}. Interestingly at this spot overlap we reach the maximum efficiency with the IR and a slight decrease in efficiency is visible at higher fluence. In cases of even lower spot overlap this trend continues with a spot overlap of 85% as shown in Figure 3.16.

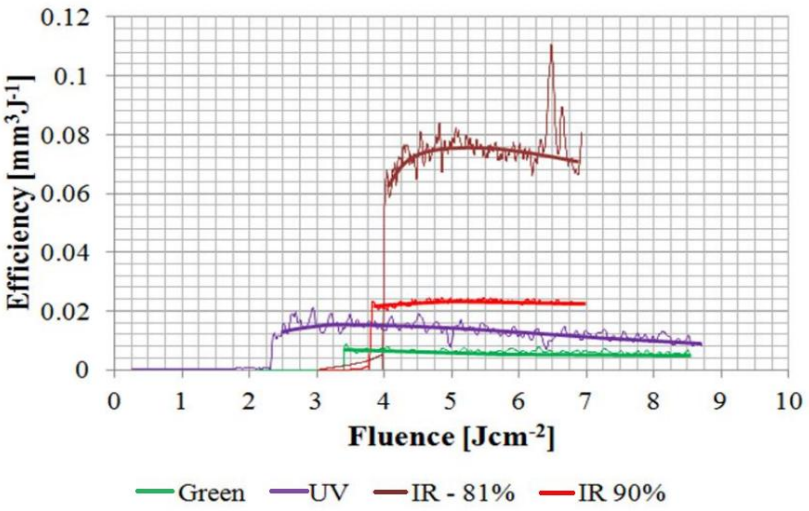

Figure 3.16: Removal efficiency for spot overlap values of 85% for 515 nm and 343 nm compared with 81% and 90% in IR.

At a pulse overlap of 85% we observe that the UV is more efficient than green. The maximum efficiency achieved with in green at this spot overlap is 8 mm^3kJ^{-1}. In the UV the removal efficiency maximum is 16 mm^3kJ^{-1}. In Figure 3.16 the efficiencies provided by a green and UV spot overlap of 85% we compared with the efficiencies with the IR at pulse overlaps of 81% and 90%. For IR the efficiency further increases with lower spot overlap values giving a maximum removal efficiency of 80 mm^3kJ^{-1}. For the higher spot overlap of 90% the maximum efficiency is still bigger than in both the green and UV, roughly 24 mm^3kJ^{-1}. It is also worth pointing out that with a spot overlap of 81% in the IR an increase in the surface roughness is observed especially at a high fluence. This increase in surface roughness, which we can see in sudden spikes in the machined profile, is due to large chips of material chipping off. The direction of the chipping is along the machining direction. Such chipping will also increase the amount of material that is removed in that case. For many machining applications the spot overlap is one parameter that can be tuned without changing anything in the laser layout, whilst the second important factor that can be changed is the line overlap. It is obvious that these are similar and likely to be related to each other. In order to study the effect of line overlap we machined squares with a 1 mm side length and varying line displacement. The line displacement was increased in steps of 1 µm, 18 squares were machined while

varying the fluence and spot overlap whilst keeping all the other parameters constant. An example of such a machined pattern is shown in Figure 3.17.

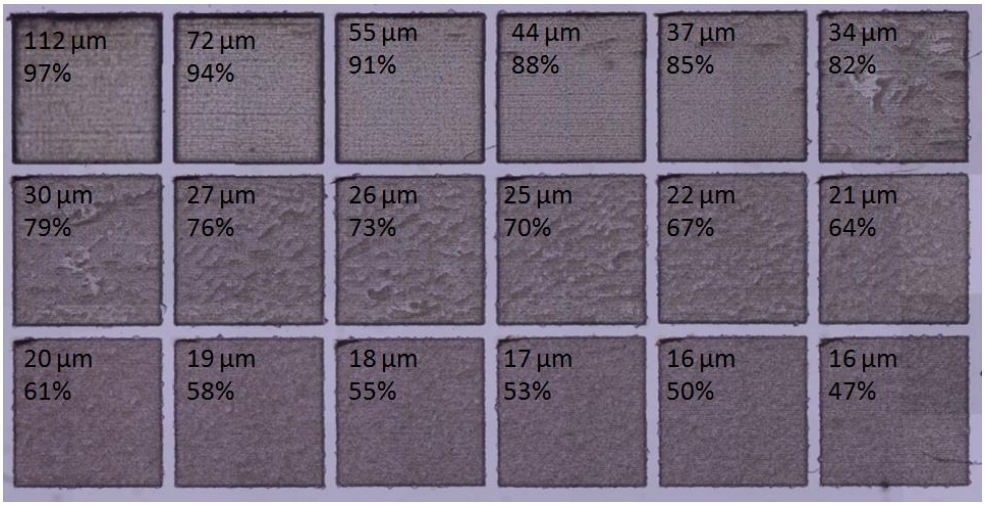

Figure 3.17: Micromilled sample in which each square was machined with a different line overlap, decreasing from top left to bottom right. The first number indicates machining depth, the second number is line overlap in %. This example was machined with the 1030 nm wavelength and a fluence of 6 Jcm^{-2}

From this study the dependency of the removal efficiency with line overlap can be calculated. A plot of this is shown in Figure 3.18. This shows the trend indicated in the study of the removal efficiencies as a function of spot overlap (Figure 3.14 - Figure 3.16). The removal efficiency increases with decreasing line overlap until a point is reached just below the machining threshold. At that point the efficiency decreases quickly. In IR we reach a maximum efficiency of over 12 mm^{3}kJ^{-1} at a 47% line overlap; in green and UV the maximum efficiency value is at a 60% line overlap and the maximum efficiency reached in both wavelengths is about 6 mm^{3}kJ^{-1}.

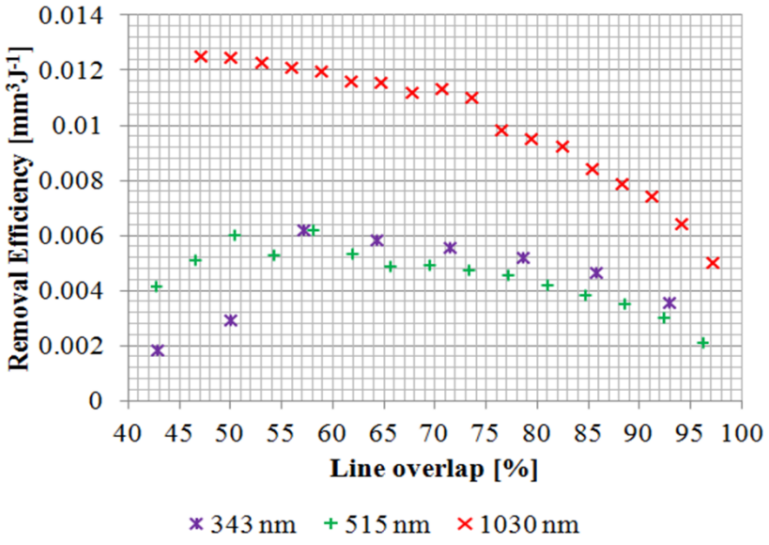

Figure 3.18: Removal efficiency for the three wavelengths as a function of the line overlap.

3.3.4 Surface roughness of laser machined fused silica

The removal rate and the efficiency are clearly important factors but thereare other factors of interest when manufacturing devices. In particular, the surface roughness and quality of machining are clearly factors that need to be considered when developing a process. A low surface roughness, high quality machining process might require little or no post processing. The surface roughness data from the spot overlap experiments does however not provide the desired information since the fluence was varied. The R_q roughness of all wavelengths and over all spot overlaps was in the range between 1 µm and 2 µm (Figure 3.19). The only notable difference was that the roughness with the IR was always higher than that generated by both green and UV. At low spot overlaps a chipping effect occurred that caused the R_q roughness to be 2.6 µm for a 70% spot overlap. Green and UV surface roughness levels were always in the same range.

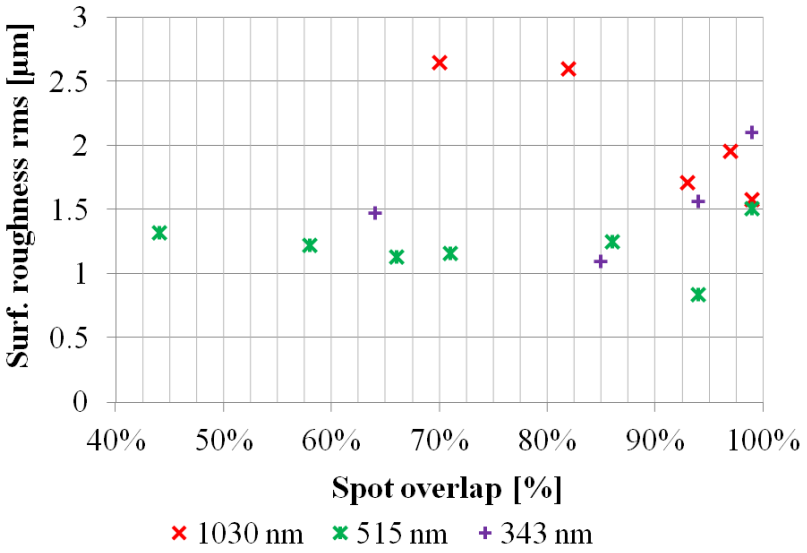

Figure 3.19: Surface roughness R_q of the machined surfaces in dependence of the spot overlap.

The data plotted in Figure 3.20, meanwhile, shows the surface roughness as a function of line spacing whilst all other parameters were kept constant.

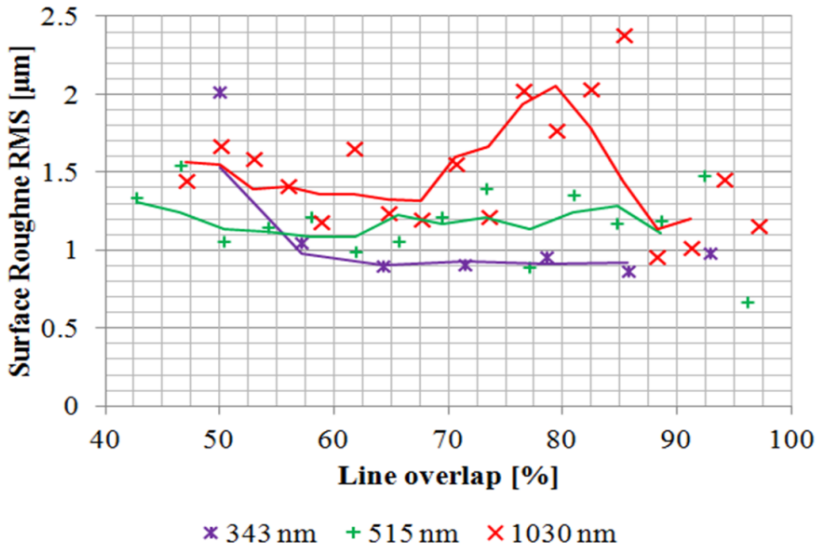

Figure 3.20: Comparison of surface roughness R_q (rms) values between IR, green and UV as a function of the line overlap. The trend lines show a moving average with a period of 3 data points.

The 343 nm wavelength consistently yields a surface roughness below 1 µm when machining above the threshold line overlap of 60 %. At these high line overlaps the surface roughness is 0.94 µm and deviates only little from this averare value. The 515 nm yields a higher surface roughness R_q of 1.22 µm and a standard deviation of 0.19 µm. The R_q average value that we achieved with the 1030 nm was higher at 1.50 µm and a standard deviation of 0.38 µm. An interesting feature that shows in the peak in the surface roughness of the IR wavelength machined areas is the surface chipping that occurs at certain fluences and at certain line overlap values. This effect is also visible on the example of the machining pattern shown in Figure 3.17.

3.3.5 Discussion of depth control in laser ablation of fused silica

The lateral precision of laser micromilling is mainly controlled by the laser beam steering setup. In our case the laser scan heads limit the lateral beam position accuracy to better than 2.8 µm [9]. In order to find the repeatability error of the high precision linear stages a repeatability test was carried out, moving the sample between the machining area and the microscope 10 times giving an error of ± 1.8 µm standard deviation. In most cases this is sufficient especially given the spot sizes used in this case.

Gaining precise control over the machining depth can be a very interesting task, for example in many microfluidics applications the flow velocity of a liquid through a channel is controlled by the depth of that channel. Hence a larger depth reduces the velocity through that channel. Many other applications can be thought of where accurate depth control can be desired. When laser machining, however, accurate control of machining depth is very difficult to achieve. It is common to describe the precision of a process in terms of the depth of material removal with each pulse, for example see Figure 3.21.

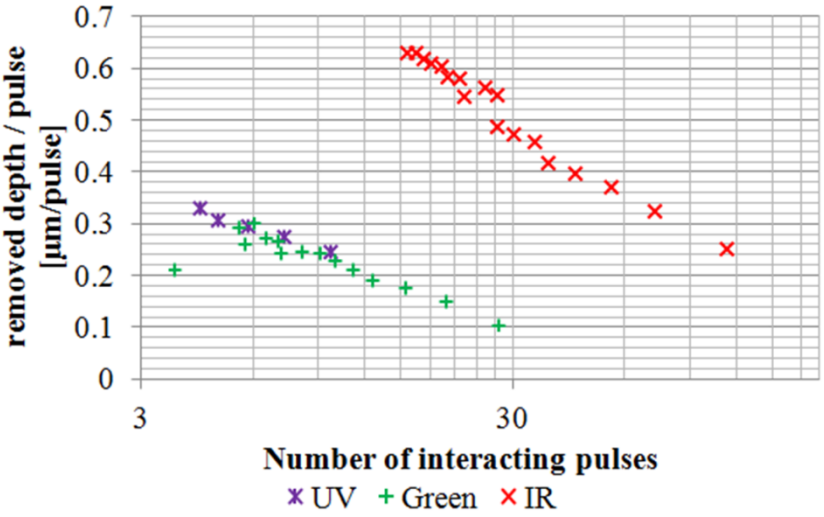

Figure 3.21: Precision of material removal as a function of the number of the interacting pulses used for micromilling. The precision is measured in removed depth per pulse.

To gain an understanding of the precision we need to know how many pulses were incident on each unit area. This value can be estimated using the spot and line overlap values. The intensity that was outside the e^{-2} intensity radius was ignored because its influence is very small. The number of interacting pulses can therefore be estimated by the following equation:

$$N_{interacting} = \frac{1}{(1 - \text{spot overlap}) * (1 - \text{line overlap})} \quad \textbf{(3.7)}$$

It is obvious that this equation overestimates the contribution of each pulse because the pulses are not square and do not have uniform intensity. This equation also plays a role in the results shown in subsections 3.3.2 and 3.3.3, where the ablation thresholds with a moving laser beam were discussed.

This measurement of precision obviously only represents an estimate of the ablation control once ablation has started. One of the difficulties in machining glasses is that due to the sudden onset of ablation a step is machined into the glass. The control over this step height is not very accurate. The smallest step heights we could achieve were 10 µm when using the IR wavelength, 6 µm with 515 nm light and roughly

4 µm when using 343 nm. Once the machining threshold is exceeded it is possible to control the average depth of machining very accurately.

3.3.6 Discussion of picosecond laser machining of fused silica

Picosecond laser milling of fused silica offers a good opportunity to achieve high precision material removal, with some limitations in respect to control of very shallow structures. Different wavelengths can be utilized for different applications. If a high material removal rate is essential but surface quality and surface roughness only has a secondary role then machining with the infrared wavelength can achieve material removal rates higher than 1 mm^3s^{-1}. This material removal rate is high in comparison to other micromachining techniques, and can even compete with some macro machining techniques. When the highest precision, or better control over the ablation depth and surface roughness is required, the UV offers advantages. This is because the ablation process in the UV is more controlled, due to an easier initiation of machining since fewer photons are required to create the initial damage to the material and start the process.

However when considering the overall efficiency it is important to point out that the efficiency of the frequency conversion from the IR wavelength to green and to UV is not linear. The production of green photons from the IR is fairly efficient; in the case of our laser system we achieved a conversion of 50 W IR average laser power to 33 W, which is a 66% efficiency, in green. And 15 W, which is a 30 % efficiency in UV. The efficiency or volume removed per J laser energy is important however when the efficiency of frequency conversion is also taken into account the entire process is more efficient in IR than in both other wavelengths.

The efficiency of material removal increases with decreasing spot overlap. Hence a spot overlap that is close to the machining threshold is desirable for the highest efficiency. This however often causes problems in the quality of laser machining because the surface roughness increases with decreasing spot overlap. Depending on

the application the spot overlap can be decreased for quick removal or increased for best quality.

3.4 Picosecond laser micromilling of sapphire

Another interesting material on which studies of micromachining were performed as part of this work is sapphire. In contrast to fused silica, sapphire is a crystalline material. Whilst being more expensive than fused silica it offers advantages with a higher transmission in the range from 2 µm to 5 µm. The transmission spectra of fused silica and sapphire are compared in Figure 3.22. The spectra shown are for a UV grade fused silica and synthetic sapphire sample, special IR grade fused silica is also available which will improve the transmission in the IR wavelength range.

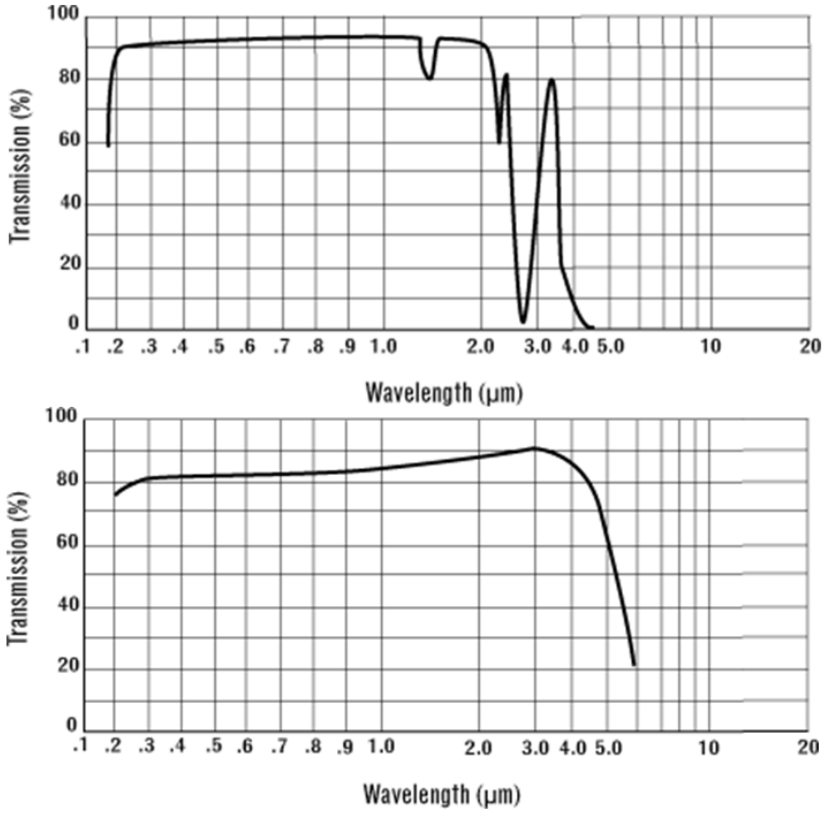

Figure 3.22: Transmission spectra of (top) UV grade fused silica and (bottom) synthetic sapphire. [1]

The transmission of sapphire peaks at roughly 3 µm, almost exactly where the fused silica has a strong dip. In the range from 1.7 µm to 6 µm the transmission is superior to fused silica. The refractive index of sapphire is higher than 1.7 which can be advantageous if a strong refraction is desired. In addition sapphire offers better mechanical properties such as a higher hardness, no softening up to temperatures as high as 2000 °C, (close to its melting point at 2030 °C) and the Young's modulus and shear modulus are an order of magnitude higher than those of fused silica. These stronger mechanical properties make it very difficult, close to impossible, to machine sapphire by mechanical machining methods.

In recent years the development of GaN LEDs is also increasing the demand for sapphire substrates and one possible application of the laser in this field is high speed cutting and cleaving of sapphire samples for semiconductor growth. A further application of this material, however, is due to the unique transmission properties in

the IR wavelengths. Micro fluidic device machined out of sapphire are easily imaginable as a future application. These devices are interesting because some materials strongly absorb these wavelengths whilst only weakly absorbing visible wavelengths, one such material is water the absorption spectrum of water is shown in Figure 3.23.

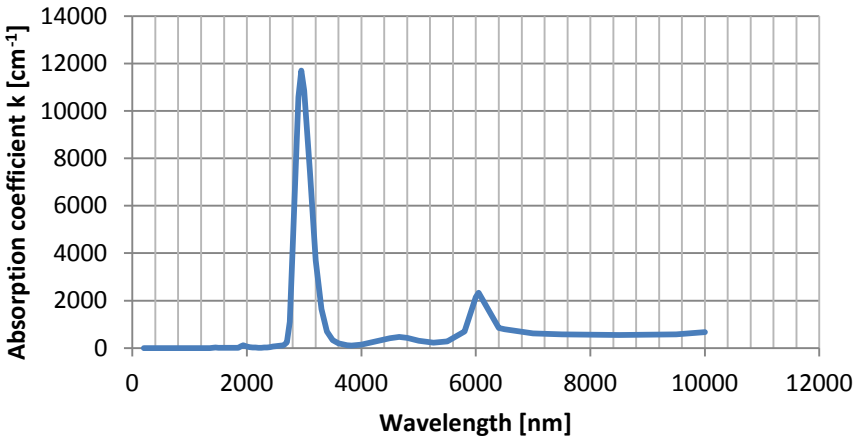

Figure 3.23: Absorption spectrum of water [11]

In order to efficiently manufacture these devices it is essential to understand the possibilities and limitations of a micromilling process. The following section describes and investigation of picosecond laser milling of synthetic sapphire.

3.4.1 Determination of ablation thresholds

As with fused silica, the ablation thresholds are found by using the damage regression model, in which the diameter of a laser machined crater is measured. By doing this measurement for varying laser fluences a pattern can be found. The relation shown in Equation (3.3) applies here as well and the threshold fluence as well as the spot diameter can be extracted from a plot of the squared diameter of the crater as a function of the fluence. Again similar to the investigation that was carried out for fused silica we determined the ablation threshold for 343 nm, 515 nm and

1030 nm wavelengths. For each of these wavelengths thresholds from single laser pulses to 50 interacting pulses was determined.

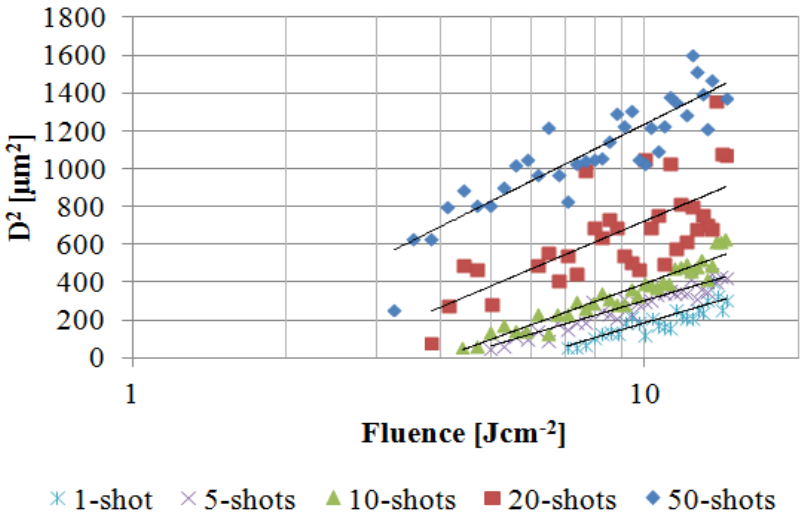

Figure 3.24: Graph showing the squared diameter of damage sites as a function of fluence used for machining, for different numbers of interacting pulses from 1 to 50. The shift towards lower thresholds for more pulses is visible.

The plot of the squared damage site diameters is shown in Figure 3.24 for the 1030 nm wavelength. From this plot we find an average spot diameter of 30 ± 3 µm. The damage threshold for single pulses is 5.9 Jcm^{-2}. The incubation behaviour that we already observed in fused silica is also apparent in sapphire and for 5 interacting pulses the thresholds drops to 4.2 Jcm^{-2}; for 10 pulses it drops further to 3.9 Jcm^{-2}; 2.3 Jcm^{-2} for 20 pulses; and 1.23 Jcm^{-2} for 50 interacting pulses. A very similar behaviour and similar values were found when the 515 nm wavelength was used.

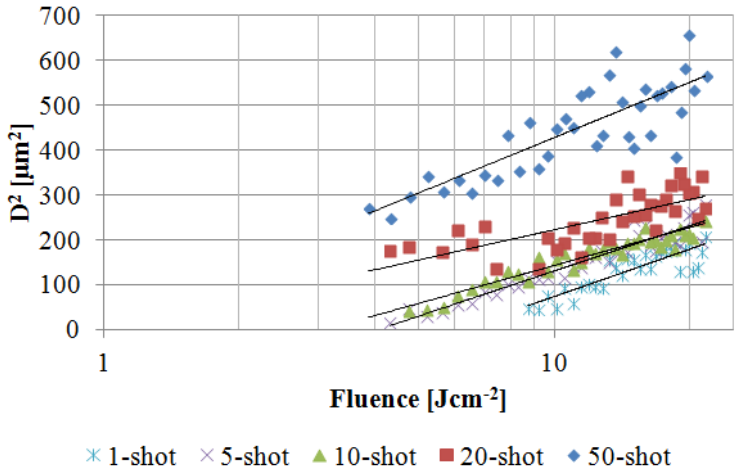

Figure 3.25: Squared diameter of laser craters machined with the 515 nm wavelength as a function of fluence. For 1 to 50 successive laser pulses on the same spot.

We find a single pulse ablation threshold of 5.9 Jcm^{-2} which decreases to 3.9 Jcm^{-2} for 5 pulses; 3.0 Jcm^{-2} for 10 pulses; 1.0 Jcm^{-2} for 20 pulses; and 0.9 Jcm^{-2} for 50 pulses. This drop is very similar to the one that was observed at 1030 nm. The spot diameter that can be extracted from the slope of the plots was used to calculate these threshold fluencies since only the energy was well known and measuring the spot size at these small sizes is difficult. The calculated spot diameter is 16 ± 2 µm.

When using 343 nm we find again very similar results, the plot of squared crater diameters is shown in Figure 3.26.

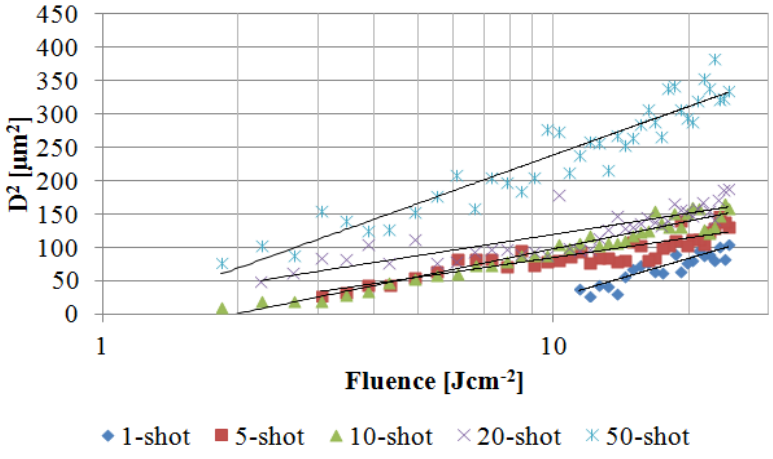

Figure 3.26: Squared diameter of damage spots as a function of the fluence for single to 50 interacting pulses.

When using the UV we find that the ablation threshold development is very similar to that at 515 nm and 1030 nm. The single pulse ablation threshold is 5.8 Jcm^{-2}; the 5 pulses threshold is 2.2 Jcm^{-2}; for 10 pulses we get a threshold value of 2.1 Jcm^{-2}; for 20 pulses 1.1 Jcm^{-2}; and for 50 pulses we get a value of just 0.6 Jcm^{-2}. The spot diameter that is extracted from these plots is 11.4 ± 1.2 µm. The threshold reduction is steeper than at both other wavelengths which suggests that the incubation behaviour is stronger. Comparing the values shown in Figure 3.27 it is clear that the three damage thresholds are very similar and have a similar development with increasing number of pulses. The solid lines are fitted to the exponential defect accumulation model which is described by equation (3.5) and was discussed in section 3.2 and discussed in more detail on fused silica in section 3.3.1, but a different incubation factor is found in each case, 0.18 for the UV, 0.13 for the green and 0.09 for the IR. Note that an incubation factor of 0 would represent no incubation behaviour. A stronger incubation effect and lower threshold fluences are expected for shorter wavelengths. The values for green and IR are very similar to the damage threshold that was found for fused silica. The single pulse threshold for the UV in sapphire, however, is higher than in fused silica. This could be due to the fact that the band gap energy of fused silica (~7.5 eV) is less than that of sapphire (9.9 eV) and it is possible to machine some fused silica materials with a two photon process whilst to machine sapphire a minimum of 3 photons at 343 nm (3.61 eV) are required.

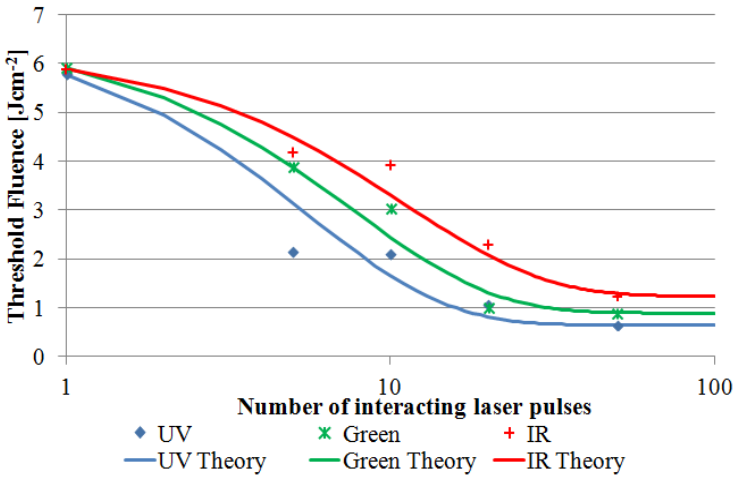

Figure 3.27: Ablation thresholds as a function of the number of pulses. Solid lines show a best fit using the exponential defect accumulation behaviour.

If only single pulses are used to machine a sample the choice of wavelength would not be that important, however, multiple pulses are typically used. Machining an area of a sample requires a scanning beam and an overlap of pulses, a very common strategy for laser micro machining.

3.4.2 Ablation rates and efficiencies in dependence of laser fluence

The machining parameters of sapphire are determined in an experiment very similar to that performed on the fused silica samples. The dependence of the ablation threshold and ablation rates on the fluence was found by machining a ramp into sapphire by increasing the energy of successive lines scanned in close proximity to each other. For easier comparison with the results presented on fused silica the distance between the lines was chosen to be 3 µm. The fluence was ramped up from 1.5 Jcm^{-2} , which is below the ablation threshold, to 5 Jcm^{-2} . The repetition rate of the laser was chosen to be 40 kHz. Although our laser can emit pulses at repetition rates of up to 400 kHz, this lower rate offers the advantage of higher precision during beam scans. This is because the galvanometer scanners have to scan at higher speeds to achieve the same spot overlap values, and they become less precise at high speeds and small errors on delays will have a bigger effect. The study here is meant to outline the possibilities of a process rather than giving a fully optimized process. The

scan heads can be further optimized for a specific scanning speed, which can be done once the potential of the laser process is known. A fair estimate of the maximum machining rates can hence be made by scaling our results up by a factor of 10. The efficiency of a process should not however change. To determine the influence of spot overlap on the machining rates the scanning speed was changed from 10 mms^{-1} to speeds as high as 400 mms^{-1} resulting in different spot overlap values for each wavelength. A table of the spot overlaps (equation (3.6)) achieved with each wavelength used for machining as a function of the scan speed and the corresponding spot sizes is shown in Table 3.2.

Scan speed [mm s^{-1}]	1030 nm (30 µm)	515 nm (16 µm)	343 nm(11 µm)
10	99.2%	98.4%	97.8%
40	96.7%	93.8%	91.2%
100	91.7%	84.5%	78.1%
250	79.2%	61.4%	45.1%
400	66.7%	38.2%	12.2%

Table 3.2: Table showing scan speeds for the minimum spot sizes achieved with the three wavelengths emitted by the picosecond laser.

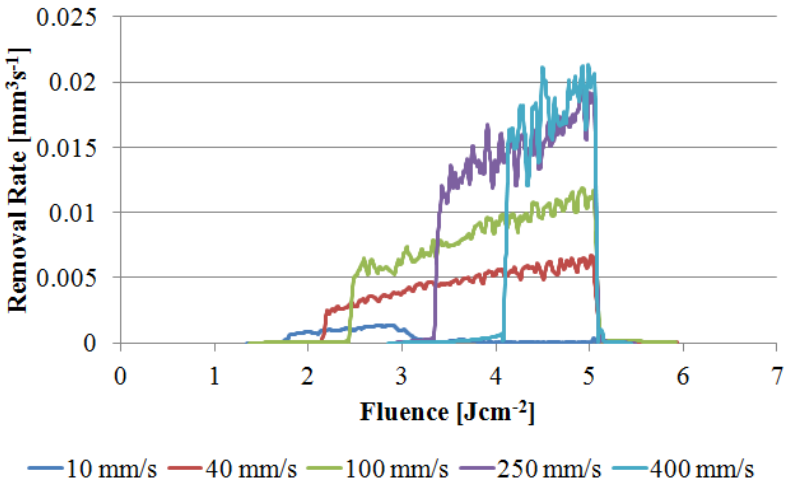

Figure 3.28: Removal rates as a function of fluence when machining sapphire with 1030 nm at different scanning speeds.

In Figure 3.28 the observed increase in removal rates with increasing scan speeds is mainly due to the fact that the higher spot overlap at short scan speeds results in a

shielding of successive pulses. The shielding effect is caused by debris and ablation plume that reflects some of the incident laser intensity away from the machining area. At high scan speeds there is no increase in removal rate between 250 mms^{-1} and 400 mms^{-1}. This indicates that already at the lower scan speed no shielding between successive pulses occurs. The incubation effect is also apparent; the machining threshold shifts from 1.7 Jcm^{-2} at 10 mms^{-1} to 4.1 Jcm^{-2} at 400 mms^{-1}. At 10 mms^{-1} the removal rate drops to zero after initial material removal. This is due to the material being removed and the debris immediately re-depositing, leading to a whitening of the material but no removal. This only occurs at high fluence and high spot overlap values. This machining window needs to be avoided when machining structures but could become useful if a highly optically scattering surface is desired. This debris is firmly attached to the work piece and could not be removed by ultrasonic cleaning. The maximum removal rate that was achieved with the 1030 nm wavelength was 0.02 mm^3s^{-1}. It is possible to imagine that with the up-scaling promised by the increase in repetition rate to 400 kHz it could be possible to remove 1 mm^3 of sapphire in 5 seconds, which is a very quick rate at these precision levels. Actual machining rates of more complicated structures would of course be lower as the scan heads cause delays when moving between the lines adding to the real manufacturing time.

The machining rate does give an understanding of possible machining speeds that can be reached. A better indicator to be investigated is how much material can be removed per unit of energy. Therefore we investigated process efficiency, and a plot of the efficiencies for the 1030 nm is shown in Figure 3.29.

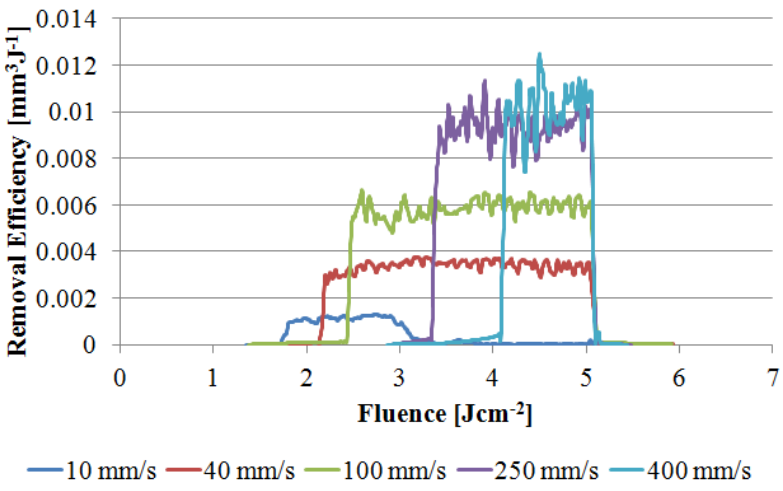

Figure 3.29: Material removal efficiency using the 1030 nm wavelength as a function of fluence for different values of scanning speed.

The removal efficiency increases up to 250 mms^{-1} and then levels out at higher scan speeds. The case of 250 mms^{-1} seems to be close to the ideal because the efficiency is high with a value of 0.01 mm^3J^{-1} while the threshold fluence is low. It is also worth noting that an increase in fluence does not lead to a significant change in efficiency therefore it is up to the user to decide which fluence is best. The laser can deliver a maximum pulse energy of 125 µJ at a repetition rate of 400 kHz which would result in a maximum energy delivery of 0.5 Js^{-1} and therefore a volume of 1 mm^3 could be removed in 2 s, however the beam delivery has losses due to the mirrors and lenses used.

In order to find out if other wavelengths offer advantages over 1030 nm the same tests were carried out with 515 nm and 343 nm. The removal rates achieved with 515 nm are shown in Figure 3.30. The removal rates for green increase with increasing fluence and increasing speed the efficiency decreases with increasing fluence, suggesting that some laser energy is lost, the results in 343 nm show a similar decreasing efficiency with increasing fluence. The removal rates for 1030 nm increase with increasing fluence, however, the efficiency remains almost constant. The achieved removal rate, at 515 nm is only 70% of the maximum removal rate achieved at 1030 nm.

Between 250 mms^{-1} and 400 mms^{-1} the removal rate does not increase much, indeed even the removal rate at 100 mms^{-1} is very close to that achieved by both faster scan speeds, indicating that the ideal point is probably reached for a scan speed between 100 mms^{-1} and 250 mms^{-1}. At very low scan speeds the debris deposition is large enough to fill up the entire machined volume.

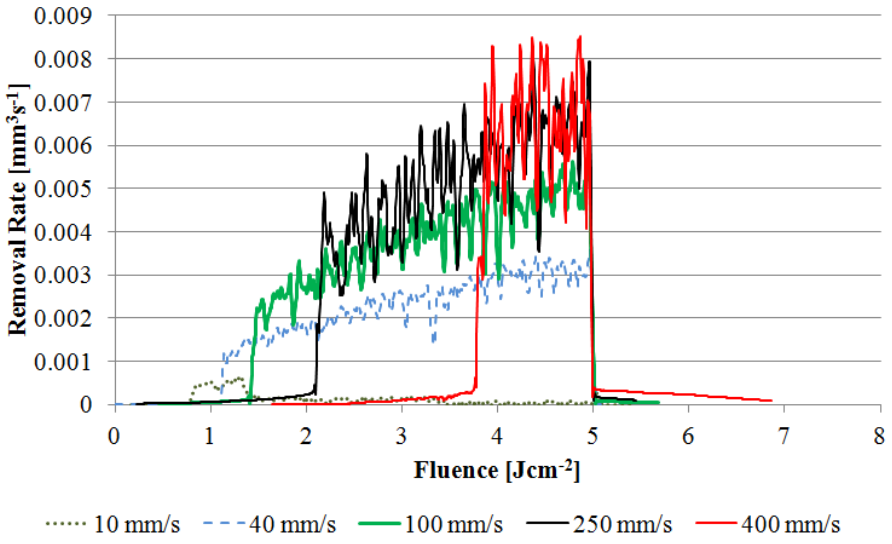

Figure 3.30: Material removal rate as a function of fluence when using the 515 nm wavelength for different scanning speeds.

The removal rate and the slight increase with higher scanning speed hints at an increase in the efficiency. A plot of the efficiency as a function of fluence for different scanning speeds is shown in Figure 3.31.

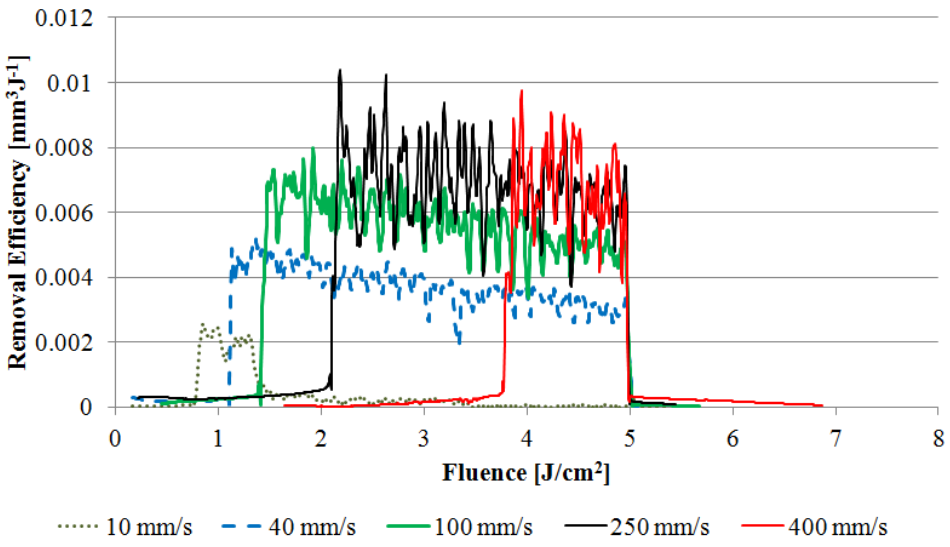

Figure 3.31: Material removal efficiency when using the 515 nm wavelength as a function of fluence for different scanning speeds.

The development of the efficiency using 515 nm light is slightly different to the development of the machining efficiency with 1030 nm light. The highest efficiency is reached at fluences just above the machining threshold and then slowly drops with increasing fluence. This could be an indication that more energy is deposited as heat in the surrounding material, which could lead to increased cracking at increased fluence, as observed experimentally.

It is interesting that the machining efficiency using 515 nm is slightly lower than that using 1030 nm. Due to the stronger incubation effect it was expected that the efficiency would be higher. In general the process with 515 nm is more expensive than the process using 1030 nm as the conversion of photons leads to a lower energy output and can be expensive; conversion of the light to 343 nm is even more expensive.

To investigate the behaviour when using UV wavelengths the same studies were carried out using the 343 nm wavelength. Again, the same ramps with the same line spacing were machined. A plot of the removal rates as a function of fluence is shown in Figure 3.32.

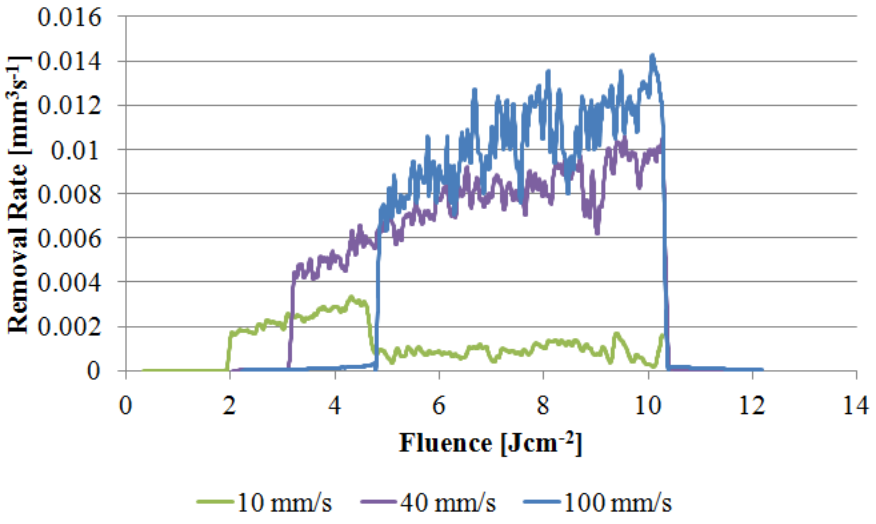

Figure 3.32: Material removal rates when machining sapphire using a wavelength of 343 nm showing the dependence of removal rate on the fluence used for different scanning speeds.

The material removal rates achieved with the UV are encouragingly high. This is due to the increased fluence that was used, however they are higher than the removal rates that were achieved with 1030 nm. The maximum removal rate that was achieved is more than 25 % higher than the removal rate achieved with 1030 nm. In the UV, however, the spot size is much smaller than for the 1030 nm results as shown discussed in section 3.1. Therefore only a very small beam overlap was achieved for scan speeds higher than 100 mms^{-1}. The small beam overlap results in no effective machining as several pulses are required to achieve a significant material removal. If the pulse overlap is too low and the pulses do not interact with each other, only small indentations are made on the sample with depths of roughly 100 nm. The maximum depths in this 'gentle machining' regime are a few hundred nm. Once the pulses overlap enough to achieve strong machining a layer of several micron thickness is removed from the sample. The maximum material removal of 0.012 mm^3s^{-1} was achieved using a scan speed of 100 mms^{-1} and a fluence of 10 Jcm^{-2}.

The material removal rate does not increase linearly suggesting a drop in efficiency at higher fluence and a deposition of the energy in a heating process which in turn

could limit the precision of the process. Hence a comparison of the removal efficiencies was carried out and the results are shown in Figure 3.33.

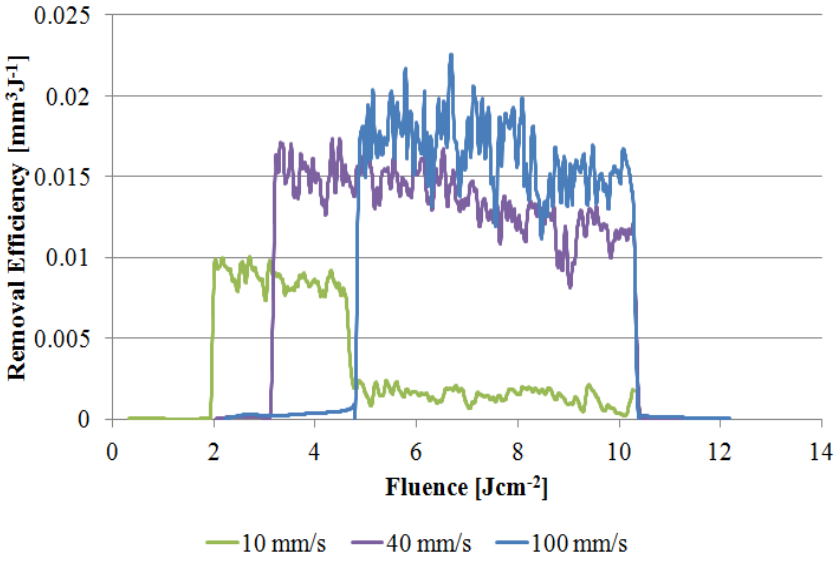

Figure 3.33: Removal efficiencies vs fluence on the sample, for different scanning speeds. The efficiencies shown here were achieved using the 343 nm wavelength.

As expected from the material removal rates shown in Figure 3.32 the efficiency is not constant over the entire range of fluences that can be used. The efficiencies obtained with both 40 mms^{-1} and 100 mms^{-1} scanning speeds are however constant until a fluence of roughly 6 Jcm^{-2} is reached. It is also worth noting that the maximum removal efficiency is almost twice as high as that obtained with the 515 nm wavelength. It is also significantly more effective than machining with the 1030 nm wavelength. The maximum material removal efficiency of 0.02 mm^3J^{-1} was achieved with the 343 nm wavelength using a scanning speed of 100 mms^{-1} and a fluence of roughly 6 Jcm^{-2}.

In conclusion, if all three wavelengths are available it is advisable to machine with 343 nm because the efficiency is the highest. 1030 nm however procides a higher average power and therefore achieves higher material removal rates. Machining with the 343 nm wavelength also resulted in more controlled and less cracked machining. Cracking in all cases was less pronounced than with fused silica and no chipping was observed. However the deposition of debris was much larger than with fused silica.

In many cases when machining fused silica it was possible to remove the debris from the sample by ultrasonic cleaning in Isopropanol, however the same cleaning process did not work as efficient in sapphire where the deposited debris seems to be more firmly attached to the sample.

3.4.3 The influence of spot overlap and line overlap on machining

Because laser machining is very complex with many influencing factors further investigation is required after finding the ablation thresholds and investigating efficiencies. Often the highest quality or the highest material removal rate is not dependant on a single parameter, but rather on a number of parameters acting together. One factor that was not changed during all experiments above was the line spacing. It is obvious, however, that the line spacing and the spot overlap are very similar, if the pulses are completely isolated there should be no difference between line and spot overlap; because they specify the distance between pulses in x and y direction. The pattern used to investigate the influence of spot and line overlap consists of 9 by 9 squares each of which with an area of 1 mm^2. The scan speed and therefore the spot-to-spot distance was increased along the x-axis and the line distance was increased over the y-axis. The scan speed was varied between 6.75 mms^{-1} and 500 mms^{-1}, providing spot overlap values as shown in Table 3.3. The line overlap was increased in steps of 1 µm, because the spot sizes of the wavelengths used are different the spot overlaps are different. The values obtained are shown in Table 3.4.

λ[nm	speed[mms^{-1}]	6.7	12.5	25	50	100	200	300	400	500
	distance[µm]	0.1	0.312	0.62	1.2	2.5	5	7.5	10	12.
343	spot	98.	97.3	94.5	89.	78.	56.	34.	12.	0.0
515	spot	99.	98.1	96.2	92.	84.	69.	54.	39.	23.
1030	spot	99.	98.9	97.9	95.	91.	82.	74.	65.	57.

Table 3.3: Scanning speeds used for machining test patterns and the corresponding spot-to-spot distances as well as the spot overlap values for each wavelength

λ[nm	Distance[µm]		1	2	3	4	5	6	7	8	9	10
343	Line	overlap	91.	82.	73.	64.	56.	47.	38.	29.	21.	12.
515	Line	overlap	93.	87.	81.	75.	69.	63.	56.	50.	44.	38.
1030	Line	overlap	96.	93.	90.	86.	83.	80.	76.	73.	70.	66.

Table 3.4: Displacement between lines and the corresponding beam overlap for the three wavelengths.

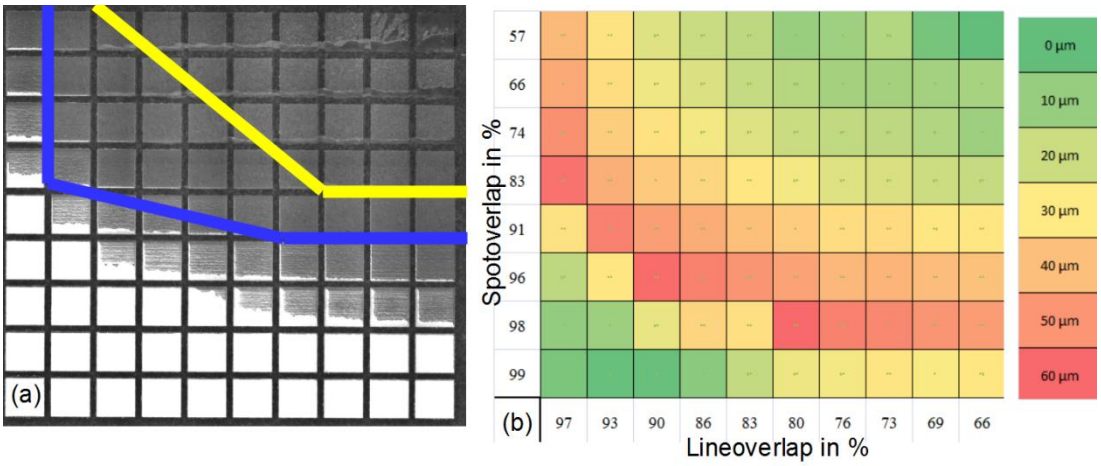

Figure 3.34: Influence of the spot overlap and the line overlap on machining sapphire with the 1030 nm wavelength. (a) Micrograph of machined squares with increased line spacing along the x-axis and increasing spot overlap along the y-axis. Below the blue line strong debris deposition occurs and above the yellow line deep cracking occurs; (b) depth map produced from the machining of (a) the row with the lowest spot overlap was not measured as the debris entirely fills the machined area.

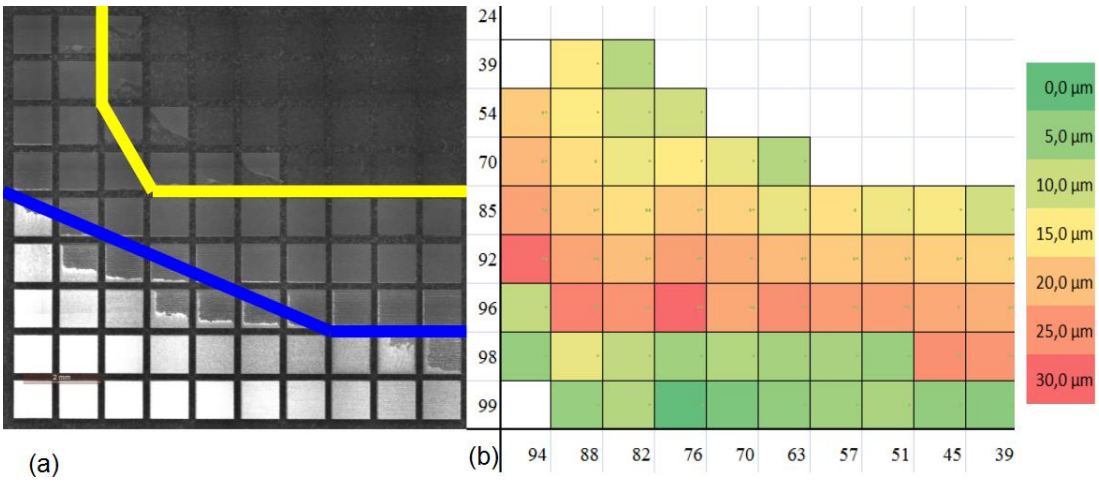

Figure 3.35: The influence of line overlap and spot overlap on machining of sapphire using 515 nm With decreasing line overlap from left to right and increasing line overlap from top to bottom. (a) Micrograph of the machined pattern with indication of increased cracking above the yellow line and increased debris deposition below the blue line; (b) Depth profile established by the pattern of (a), the colour code is shown on the right.

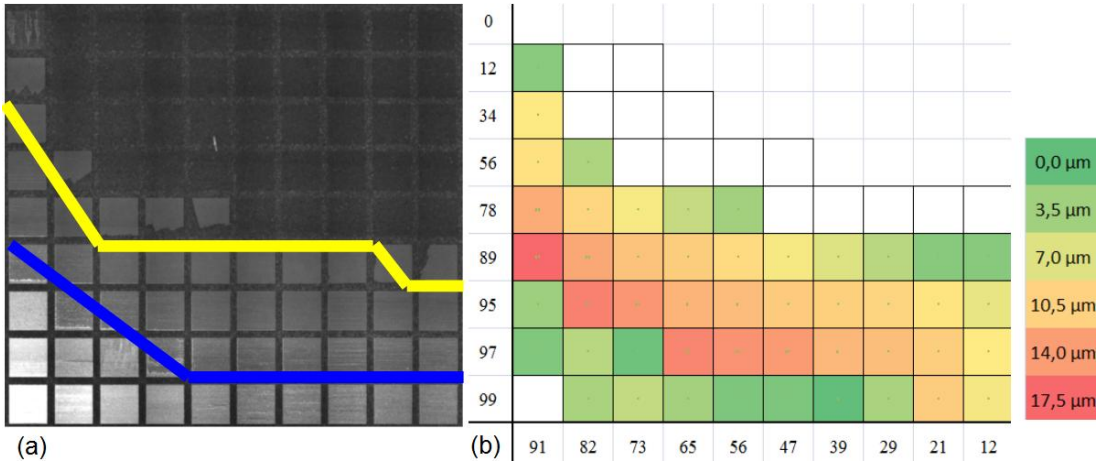

Figure 3.36: (a) Pattern machined with UV. Above the yellow line cracking or no machining occurs whilst below the blue line the amount of debris deposited has a strong effect on the measured depth. (b) The resulting depths of machining with values in µm. The bottom left square has an increased height because the redeposited debris accumulated in the machined square and is higher than the surrounding sapphire.

The machined patterns all show that an increased accumulation of debris occurs when successive pulses are placed in very close proximity. A likely reason for this is that the machining establishes a very deep and narrow trough in which the debris

from the next line or successive pulses is more likely to deposit due to confinement of the expanding plumes, which quickly condense on the rough surfaces of the previously machined area. This is also supported by the fact that the measured profiles often have a peak in depth at the end of the scan. This is confirmed by the last lines which deposit the debris to the side but because no line follows there is no debris to fill up this gap. A typical depth profile of one of the debris filled squares is shown in Figure 3.37.

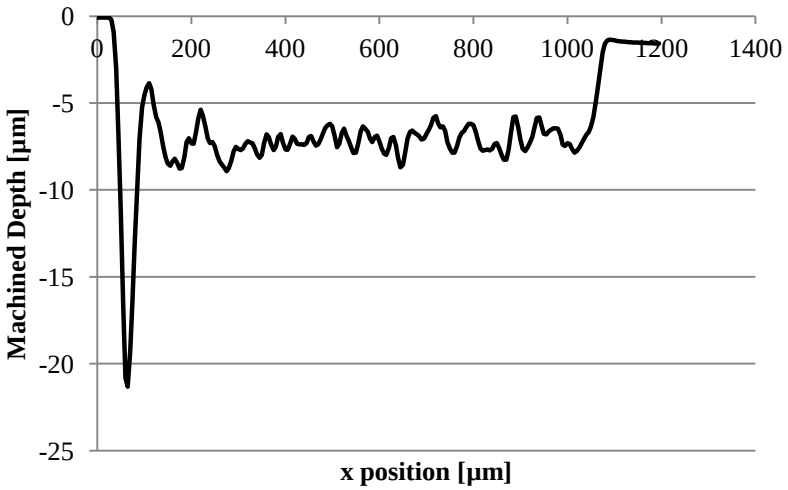

Figure 3.37: Depth profile of a debris filled square that was machined in sapphire with a spot overlap of 98.9 % and a line overlap of 86.3 % using the 1030 nm wavelength showing the peak depth at the last line that was machined.

The profiles that were entirely filled with debris were not measured because the material removal cannot be judged. For squares in which no deep machining occurred the profile was also not measured. Often the spot overlap or the line overlap was not sufficient to allow the accumulation behaviour and deep machining did not start but single spots of a few 100 nm depth were machined. As the resolution of the surface profilometer is not high enough when measuring deep features these were not taken into consideration. From these considerations we can derive that machining with a low line overlap can cause cracking and machining with a too high line overlap is not a very good approach as it leads to excessive deposition of debris.

In the machining depth plots the maximum value identifiable as being laser machined was used to determine the depth value. This is important as some of the squares are half filled with debris or did not machine entirely. For such examples, indicated above the red line or below the green line in (Figure 3.34(a)-Figure 3.36 (a)), the value that was identified as laser machined was used. This leads in some cases to over estimation of the average machining depth however these parameters do not affect the general outcome of this study as they are not ideal anyway and should not be used for machining. This effect is more pronounced when using 1030 nm and 515 nm (Figure 3.35(a) and Figure 3.36(a)). When using the 343 nm wavelength less debris deposition takes place and more combinations of spot and line overlap are possible. Machining did however not occur for low overlap values because pulses were entirely separated.

The depth of machining is only part of optimizing a process as discussed in section 3.3.4 for fused silica. The efficiency, the removal rate or the quality of laser machining are all factors that can be of more importance for a process than the depth that can be achieved in a single scan. The material removal rate and the efficiency of the process are actually very closely related in this case because the laser repetition rate and pulse energy were kept constant, therefore a simple calculation of the energy the laser delivers per second transforms the removal rate into the removal efficiency. Of course this needs to be carried out for each wavelength because the laser energy that was delivered varies for each wavelength.

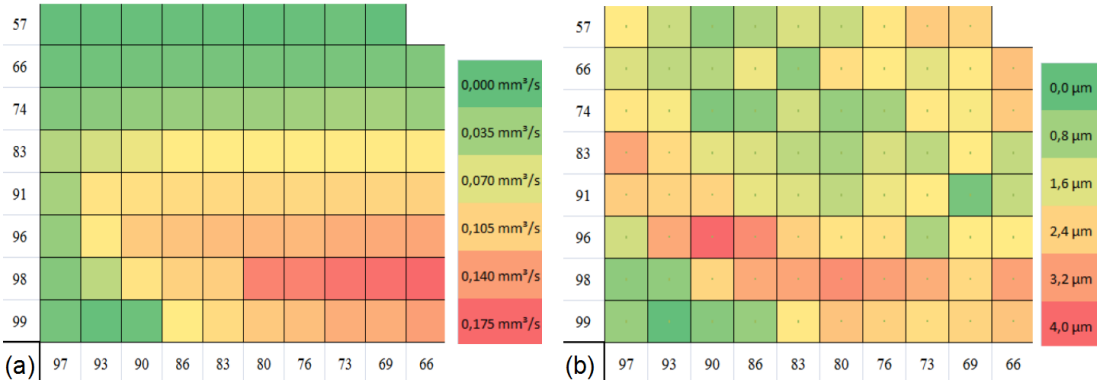

Figure 3.38: (a) Material removal rate map (values in mm^3s^{-1}) for machining sapphire with the 1030 nm wavelength as a function of spot overlap (x-axis) and line overlap (y-axis) for a fluence of 7.1 Jcm-2 and a pulse energy of 47 µJ; (b) the corresponding surface roughness map (values in µm rms).

With the 1030 nm wavelength we achieve a maximum material removal rate of 0.042 mm^3s^{-1} at pulse overlap and line overlaps of roughly 70 %. This value translates into an efficiency of 0.022 mm^3J^{-1}. This gives a maximum removal rate that we could theoretically achieve when running the laser at the full 400 kHz of 0.4 mm^3s^{-1}. It is worth noting that the highest surface roughness values do not necessarily occur where the material removal rate is highest, but rather the highest surface roughness appears close to the squares in which the debris redeposition was strongest. This is likely to be cause by some particles of the debris attaching all across the surface causing a rise in surface roughness. The surface roughness for the most effective machining is around 1.2 µm rms. The lowest surface roughness of 0.8 µm rms is achieved when using a line overlap of 90% and a spot overlap of 75 %. The average value of all surface roughness measurements is roughly 1.5 µm.

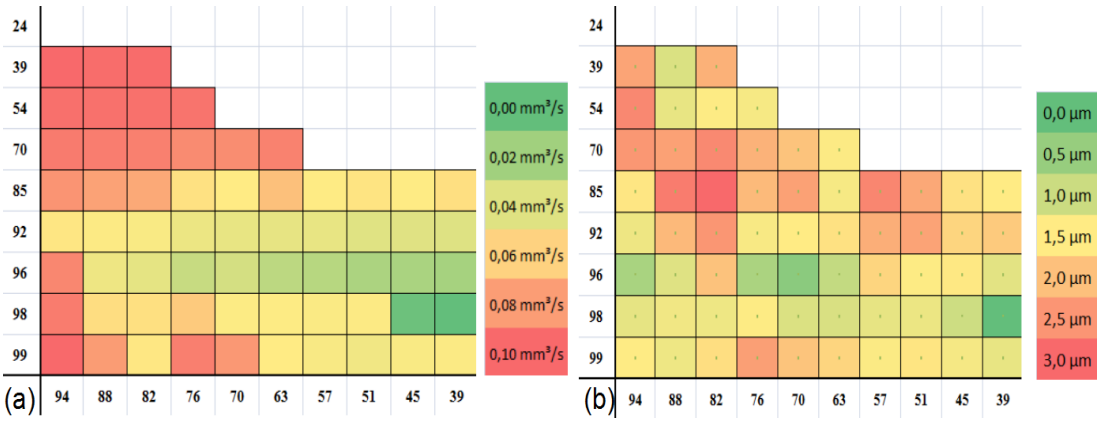

Figure 3.39: (a) Material removal rate map for the 515 nm wavelength; (b) corresponding surface roughness map (µm rms).

When 515 nm is used to machine the pattern a fluence of 10.5 Jcm^{-2} and a pulse energy of 22 µJ were used. The maximum material removal achieved is a band that stretches from a line overlap of 88 % and a spot overlap of 40 % to a spot overlap of 85 % and a line overlap of 40 %. The maximum of 0.0073 mm^3s^{-1} within this band was achieved at a line overlap of 45.1 % and a spot overlap of 84.8 % however the differences are very small. This translates into a removal efficiency of 0.0083 mm^3J^{-1}. However in some cases this might be tolerable especially when a lower surface roughness is required. The 515 nm wavelength consistently achieves lower surface roughness values than 1030 nm; again the highest removal rate and the lowest surface roughness of roughly 500 nm rms are achieved at values of 70 to 80 % for both spot and line overlap. The surface roughness averaged over all values for which a measurement was taken is roughly 1 µm rms.

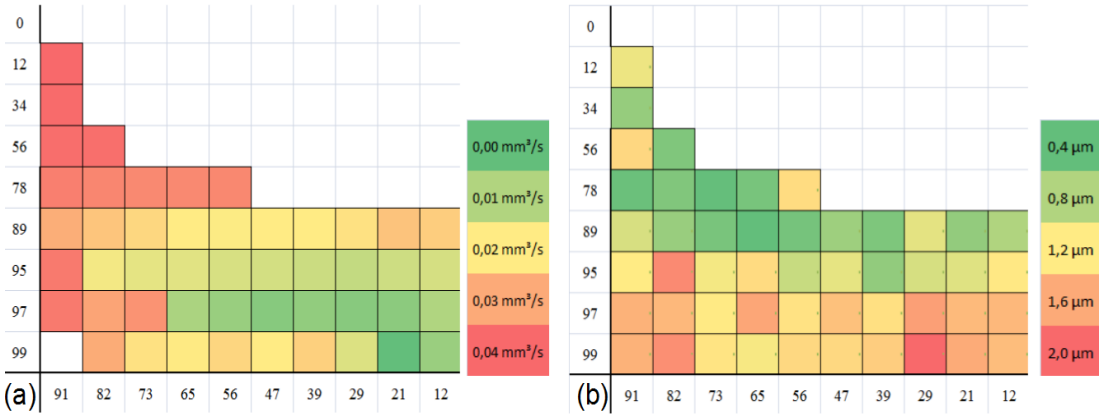

Figure 3.40:(a) Material removal map for the 343 nm wavelength; (b) corresponding surface roughness map (µm rms).

The 343 nm wavelength removal rates are not as high as those achieved with 515 nm and far off those achieved with 1030 nm. The maximum value for 343 nm, 0.0017 mm^3s^{-1}, was achieved with a line overlap of 56 % and a spot overlap of 89 %. This corresponds to an efficiency of 0.0043 mm^3J^{-1}. Similar to the relationship between 515 nm and 1030 nm the surface roughness was further reduced to values of 420 nm rms which was achieved at a line overlap of 73.7 % and 78.1 % spot overlap. The average surface roughness from all measured squares was 870 nm rms.

All these values give an indication that the fastest material removal, and therefore quick and rough machining of sapphire, is done when using a sufficient fluence of 1030 nm light at good overlap values of roughly 70 % in each direction. A better surface quality can be achieved when using the 343 nm or 515 nm. The surprising detail is that 343 nm is not as efficient when machining sapphire and the surface roughness improvement of 80 nm at the best parameters does probably not justify the increased cost in using the 343 nm for large area milling, unless a special case of very high quality is required. Further advantages of the 343 nm wavelength are that the removal depth can be controlled much more accurately. The smallest step height that was achieved when using 1030 nm is in the order of 8 µm, for 515 nm this is reduced to 5 µm and for 343 nm it is roughly 2.5 µm. For some applications this step height is very important, for example, in microfluidics flow rates need to be controlled very accurately or a very small volume flow through a very thin channel.

Similarly the quality of the laser machined edge can be crucial for certain applications, for example, if a thin wall of a few tens of µm is desired the edge quality can be the decisive reason to choose the 343 nm option examples of the quality of laser machined edges at the three different wavelengths is shown in Figure 3.41.

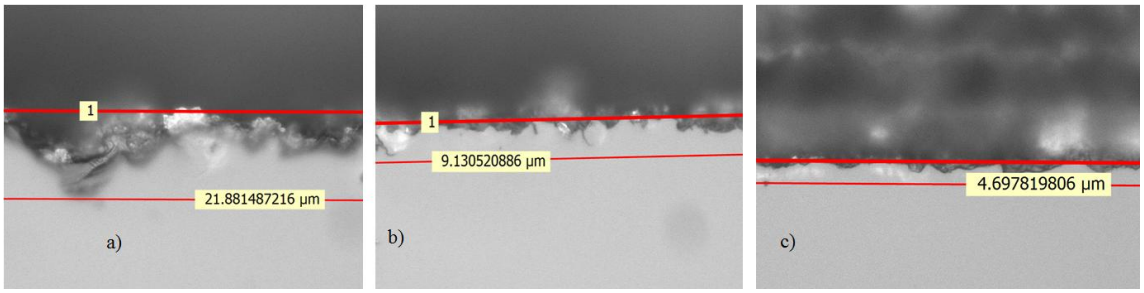

Figure 3.41: Surface of the unmachined sapphire at the edge to a machined square indicating the width where chipping and cracks propagate into the bulk sapphire to show the differences in edge quality that can be achieved with (a) 1030 nm, (b) 515 nm and (c) 343 nm.

3.5 Conclusion of high precision laser micromilling

The transparent and difficult to machine materials, fused silica and synthetic sapphire, can be machined with picosecond laser pulses. The achieved material removal rates are in a very usable range. Depending on the levels of precision desired one can choose between the three wavelengths and achieve removal rates close to 1 mm^3s^{-1} in fused silica and in excess of 0.2 mm^3s^{-1} in sapphire. These material removal rates are suitable for many applications such as microfluidic devices or larger scale precision cutting and milling of complex shapes out of these, very attractive, dielectrics. The achievable surface roughness and quality of machining enables true micro structures to be established using a very fast and easily adaptable laser manufacturing process. For many applications the green wavelength offers a good compromise because the green wavelength is quite efficiently produced while the surface roughness levels are only marginally larger than the values achieved with 343 nm. The edge quality of 343 nm is however unrivalled and

for some specialist applications this is required. One such example is shown in the next chapter which will discuss the manufacture of fibre optic sensing devices using picosecond laser pulses.

References

1. RMI, Rocky, Mountain, and Instrument, "Synthetic Sapphire Specifications," (2013).
2. J. M. Liu, "Simple technique for measurements of pulsed Gaussian-beam spot sizes," Optics Letters **7**, 196-198 (1982).
3. Y. Jee, M. F. Becker, and R. M. Walser, "Laser-induced damage on single-crystal metal surfaces," J. Opt. Soc. Am. B **5**, 648-659 (1988).
4. D. Gómez, and I. Goenaga, "On the incubation effect on two thermoplastics when irradiated with ultrashort laser pulses: Broadening effects when machining microchannels," Appl Surf Sci **253**, 2230-2236 (2006).
5. H. Choi, D. Farson, J. Bovatsek, A. Arai, and D. Ashkenasi, "Direct-write patterning of indium-tin-oxide film by high pulse repetition frequency femtosecond laser ablation," Appl Optics **46**, 5792-5799 (2007).
6. M. Mero, J. Liu, W. Rudolph, D. Ristau, and K. Starke, "Scaling laws of femtosecond laser pulse induced breakdown in oxide films," Phys Rev B **71**, 115109 (2005).
7. F. Costache, M. Henyk, and J. Reif, "Modification of dielectric surfaces with ultra-short laser pulses," Appl Surf Sci **186**, 352-357 (2002).
8. D. Ashkenasi, M. Lorenz, R. Stoian, and A. Rosenfeld, "Surface damage threshold and structuring of dielectrics using femtosecond laser pulses: the role of incubation," Appl Surf Sci **150**, 101-106 (1999).
9. SCANLAB_AG, "hurrySCAN, hurrySCAN II Technical Data Sheet," SCANLAB_AG, ed. (http://www.scanlab.de, 2011).
10. L. M. Machado, R. E. Samad, W. de Rossi, and N. D. V. Junior, "D-Scan measurement of ablation threshold incubation effects for ultrashort laser pulses," Opt. Express **20**, 4114-4123 (2012).
11. W. M. Irvine, and J. B. Pollack, "Infrared optical properties of water and ice spheres," Icarus **8**, 324-360 (1968).

Chapter 4: Picosecond laser manufacturing of optical fibre cantilever sensors

In this chapter a particular application of picosecond laser micromilling of fused silica glass is described. This application is to manufacture cantilever sensing elements out of an optical fibre in order to create a miniaturized optical sensor for operation with a remote detection system. Two standard single mode optical fibres designed for a wavelength of either 1550 nm (SMF-28) or 633 nm (SM600) have been used for manufacturing the sensors. These two fibres are made out of fused silica and have an outer (cladding) diameter of 125 µm. The only difference in terms of laser machining between these two fibres is the core diameter, which is 9.3 µm for SMF-28 and 4.3 µm for SM600. A cantilever structure is chosen because of its versatility as a sensor. Cantilevers can be used in scanning probes to measure surface topography; they can also be used, with the appropriate coating, to measure bio-chemical interactions; in general forces of almost any kind can be measured. A microcantilever is designed to fit into the smallest spaces, and a fibre optic tip is an ideal platform for high accuracy measurements in difficult areas, for example space constrained, electromagnetically noisy, or hazardous environments. In this chapter the approach towards mass manufacture of a fibre based cantilever sensor is described. The fibre cantilever working principle is explained and possible designs are shown. A manufacturing approach using laser machining was developed with laser parameters carefully optimised to avoid issues of cracking, and to negate the effect of taper angle. A single sensor was laser machined in less than 6 minutes (including manual alignment) improving on current technology by a factor of 40. This could be improved further with investment in automatic alignment. An electric arc was used for post-processing to improve the optical return from the machined surface, and finally a sensor was demonstrated in a deflection experiment.

4.1 Introduction to fibre optic sensors

Optical fibres show very little attenuation and therefore allow optical signal changes to be detected remotely. The detection of phase, wavelength and intensity of the light are all possible, which are the key factors that enable fibre optic sensing. In parallel to the developments in fibre telecommunication technology, optical fibres were developed for fibre optic sensing applications, exploiting the technology that was developed for the telecommunication industry and became affordable through mass manufacture. There are several reasons why optical fibres are widely used for sensing applications [1]:

- Immunity to electro-magnetic fields
- Inability to conduct currents
- Easy to integrate into larger structures, buildings, bridges
- Little to no ageing effects
- High sensitivity
- Multiplexing compatibility
- Variety of sensing applications;
- Lightweight
- Small in size.

Fibre optic sensors can be grouped into two main groups: (i) intrinsic sensors in which the light modulation occurs inside the fibre core and (ii) extrinsic sensors in which the light modulation occurs outside the fibre core, either in the cladding or in the external environment. Many of these are based on an intensity change to sense for example vibrations or translation [1]. Intensity modulation can easily be achieved because the light leaving a fibre is diverging at an angle specific to the refractive index difference between the core and the cladding. By placing a small reflecting substrate in front of the fibre an extrinsic sensor can be built that for example detect vibration through an intensity modulation [1].

Another type of extrinsic sensor is an extrinsic interferometer sensor most of which are so called extrinsic fabry perot interferometers (EFPI). This type of sensor contains two reflective surfaces separated by a cavity. The first conventional optics version of this interferometer type was developed in 1899 [2] and found application in high resolution spectroscopy. In the early 1980's, the EFPI was manufactured out of optical fibres and demonstrated to measure small length deviations [3]. This type of sensor is very similar to the one that is manufactured as part of this thesis. The main difference is that the configuration that is manufactured is more a Fizeau interferometer because the surfaces are not highly reflective. A Fizeau type interferometer typically has surfaces with a reflectivity between 4 and 30 %. Because both of these interferometers are very similar and in the literature the type of interferometer that is machined in this study is mostly reffered to as a Fabry-Perot interferometer I will stick to this terminology for the purpose of this thesis.

In this chapter, a laser-based fabrication process for EFPI sensors made of optical fibres is described. The Fabry-Perot cavity in the sensing elements is produced by removing material from an optical fibre using picosecond (ps) laser pulses.

4.1.1 Sensor designs and their working principles

In this section, the working principles of two different optical fibre-based EFPI sensors are discussed.

A fibre top cantilever sensor developed by Iannuzzi *et al*. [4-9] is shown in Figure 4.1. In this design, an optical cavity is established between the fibre end and the cantilever. Since both surfaces of the cantilever can act as an optical cavity, there are in fact three different cavities. The first cavity is formed between the surfaces A and B, the second is between the surfaces A and C, and the third is between the surfaces B and C, as can be seen in Figure 4.1. For interrogation of the cavity length (surfaces A and B) a broadband source is used that is coupled into the fibre by a 3dB coupler. The reflection spectrum is recorded using a spectrometer, and the signal is processed by a computer. By using an FFT algorithm to measure cavity length several cavities can be measured simultaneously and a single distinct peak can be

distinguished for each cavity length [10]. When actuating the cantilever, the cavity formed by surfaces B and C is the only one that does not change in length.

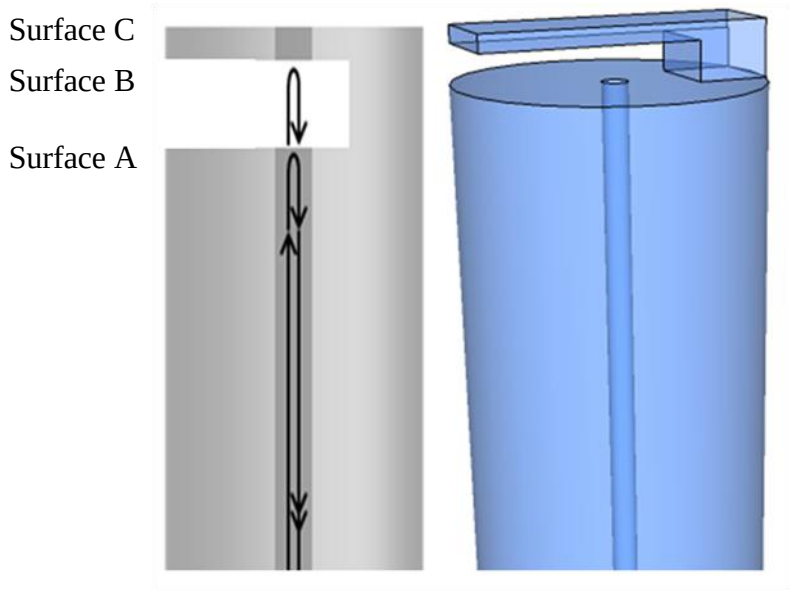

Figure 4.1: Basic fibre-top cantilever design and indication of the optical path.

The second design of an optical fibre-based sensor is shown in Figure 4.2. This sensor was designed at Heriot-Watt University. In this design, the cantilever and the optical cavity are established along the side of the fibre. The light travelling inside the fibre core is reflected towards the cantilever by a fibre-end surface which was cut at an angle of 45 , as indicated in Figure 4.2. This design although slightly more complicated than the fibre-top cantilever sensor offers better flexibility for the cantilever geometry, especially regarding its length which can be several 100's of micrometers. This is very important in terms of the mechanical response (sensitivity) of the cantilever to the acting force.

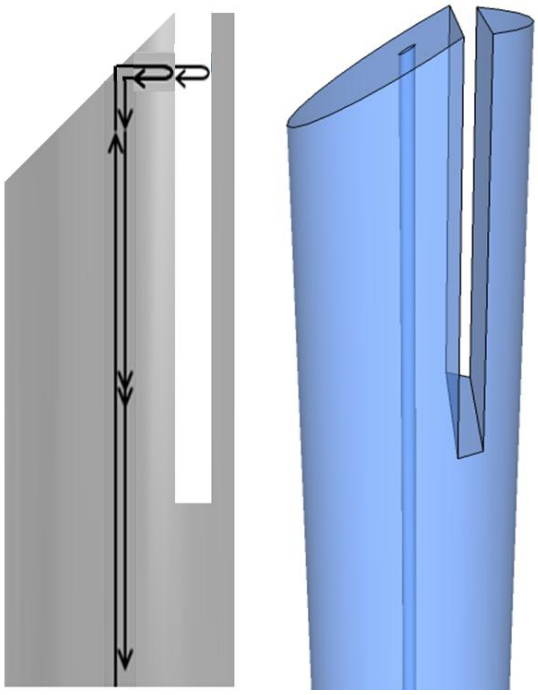

Figure 4.2: Fibre side cantilever design, the light is directed towards the cantilever by the 45 ˚ angled cut at the end of the fibre.

The mechanical behaviour of a static cantilever can be estimated by simplifying the Euler-Bernoulli equation which is used in basic beam theory:

$$\frac{d^2}{dx^2}\left(EI\frac{d^2y}{dx^2}\right) = q \qquad \textbf{(4.1)}$$

where x is the position along the beam, y is the deflection perpendicular to x, E is the Young's modulus, I is the second moment of area and q is a distributed load. One of the boundary conditions to solve equation (4.1) for a cantilever is to assume that one end of the beam is fixed. Another assumption is that the product of E and I are constant and a load is applied only to the free end – like in our application of the cantilever.

This is also the case investigated in our demonstration application where the cantilever is actuated; however for the final application of biomedical sensing a

distributed load has to be considered. By taking into account all the assumptions above, the deflection can be estimated as follows:

$$y = \frac{WL^3}{3EI} \tag{4.2}$$

where L is the cantilever length and W the applied load.

In the case of a fibre-top cantilever, the second moment of the area is given as follows:

$$I = \frac{bh^3}{12} \tag{4.3}$$

where b is the beam width and h is the beam thickness. For a rough estimate the same equation can be used for the side cantilever. Equation (4.3) shows that the width b of a beam has less influence on the deflection than the thickness h. Based on Equations (4.2) and (4.3), the ratio between thickness (h) and length (L) are the main factors in determining the mechanical response of the cantilever to an applied load.

In the case of fibre top cantilevers, the cantilever length is limited to the diameter of the fibre used. This means that the deflection of these cantilevers can be very small. For instance, when a point load (W) of 1 μN is applied to a fibre top cantilever with the width (b) of 20 μm, thickness (h) *of* 10 μm, and length (L) *of* 110 μm, then the deflection (y) is only 11 nm. In the case of a fibre side cantilever, where its length (L) is 500 μm and the thickness and width remain unchanged, the deflection is increased to approximately 1000 nm.

A cantilever sensor of this type can be used to measure all kind of forces. The cantilevers that were manufactured as part of this thesis were tested in an actuation where the cantilever was pushed with a motion stage. The final application of the cantilever is to use them for bio-chemical sensing. This can be done by applying a

coating to the cantilever a change of surface tension when a certain reaction occurs will pull or push the cantilever towards the fibre because the coating is only applied to one surface of the cantilever.

4.1.2 Manufacturing approaches

Machining the fibre top cantilever relies on the generation of a thin free standing structure that is attached to only on one side of the fibre end. We identified the general steps necessary to machine such a structure. A ridge is established on the end of the fibre and a cut underneath the top surface of the ridge will establish the cantilever. Two different methods to machine a ridge were found, (i) from the side and (ii) from the top of the fibre. In terms of alignment and simplicity at the fibre mounting arrangement a complete side machining approach appears the easier choice. A schematic drawing of this approach is shown in Figure 4.3. The fibre is mounted on the side, so that the laser is never incident on the cleaved top surface of the fibre. First a ridge is established by scanning the laser beam across the side of the fibre in a way that the outer parts are removed [Figure 4.3(a)]; this ridge is rotated by 90º so that the cut underneath the cleaved surface of the fibre can be made [Figure 4.3(c)].

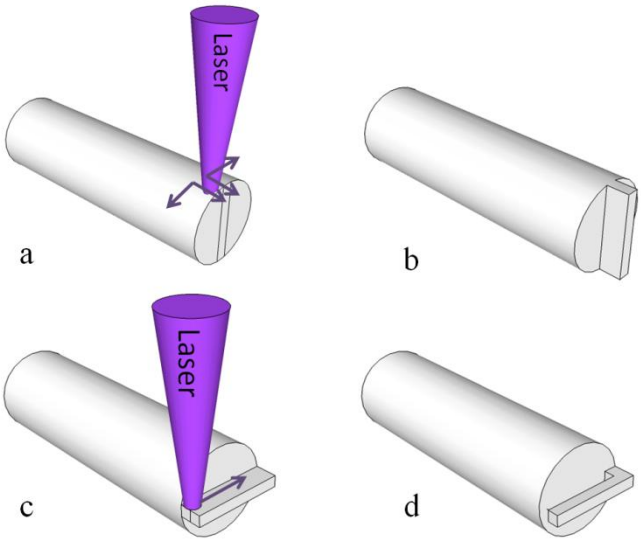

Figure 4.3: Manufacturing approach with all machining steps carried out from the side: (a) carving a ridge (b), (c) rotated by 90 degree to make the cut establishing (d) the finished cantilever.

While this approach on first sight seems to be simple it is important to correct for the tapering angle which makes things much more complicated. Either side of the ridge needs to be machined at an appropriate angle to correct for the taper in each case. More importantly correction for the cut underneath the cleaved surface is crucial. The axis of rotation necessary for this correction is different to the one required for rotation of the fibre after the ridge is cut therefore a two axis goniometer and a total of four cuts is necessary to remove all tapering angles.

The second approach to manufacture fibre top cantilevers starts again by establishing a ridge on the end of a fibre. The difference is the direction from which machining starts. The effect of the tapering angle can be used to shape the end of the fibre into a shape that resembles the tip of a flat screwdriver. We machine with the laser incident on the cleaved end face of the fibre. The beam is scanned in lines parallel to the later ridge across the cleaved end face of the fibre (see figure Figure 4.4 (a))leaving a central part of the fibre un-machined, which will later form the ridge. The exact pattern of laser scanning has a strong impact on the final result and will be explained in more detail in section 4.3.1. The schematic drawing in Figure 4.4, shows the steps that are used to machine the cantilever sensors. First a ridge is produced, after a rotation by 90^{o} plus the appropriate correction angle for the taper, two cuts removing each one tapered surface are made, a final cut removes the central structure that was left by the two earlier cuts to decrease debris on the previously machined surface.

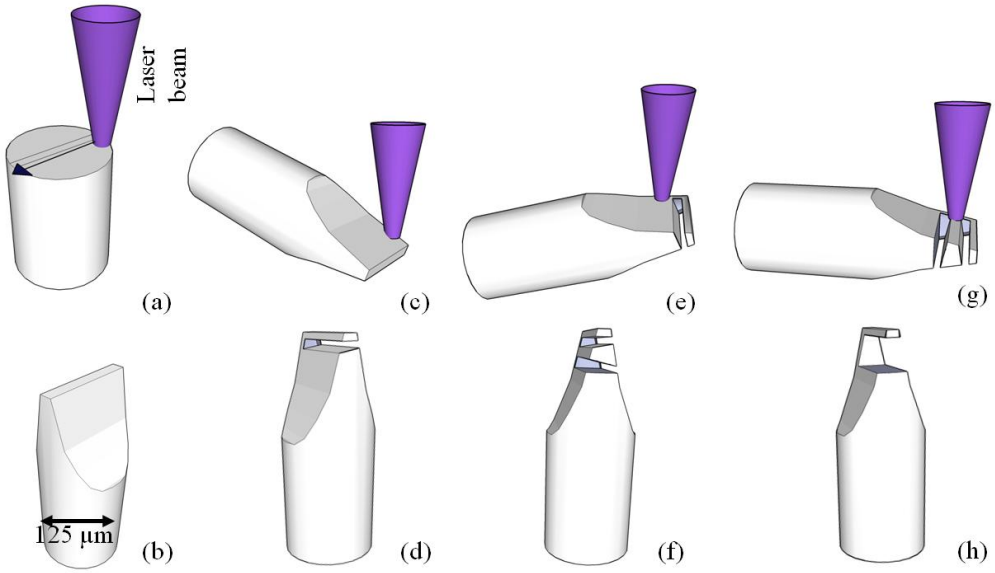

Figure 4.4: Optimised manufacturing approach for fibre top cantilever, top row machining steps, bottom row resulting structure. a) machining the ridge, c) first cut to establish cantilever already tilted to correct one surface for tapering angle, e) second cut to correct the second surface, g) removing central debris reducing structure, h) finished cantilever sensor.

The side cantilever (Figure 4.2) meanwhile can be manufactured using an all side approach. The 45º mirror surface will be either machined using focussed ion beam milling, in cases where only a very small mirror is needed, or the entire fibre is mechanically polished at 45º prior to laser machining. The cut for the side cantilever needs to be corrected for the tapering angle, which can be achieved by a rotation around the long axis. The main challenge in this approach is the positioning of the fibre so that the laser machining avoids the core of the fibre, also keeping the cantilever thin and stable is difficult.

4.1.3 Description of the setup and the mechanical mounts

To machine the fibre the picosecond laser machining setup described in Chapter 3 was used. For additional flexibility and to introduce the ability to correct for the tapering angle two rotational axes were added. For the initial approach of the fibre side cantilever one axis of rotation is required without correcting for tapering, if the important taper between the cantilever and the end of the fibre is also corrected two

rotational axes are required. The second approach to machine the fibre top cantilever requires only one axis of rotation however the stage used must allow rotation by at least 90º plus the taper correction angle. We used a rotation stage to achieve this because our goniometers did not provide the required range of rotation. To machine the fibre side cantilever only a single rotational axis is needed that is directed along the core of the fibre.

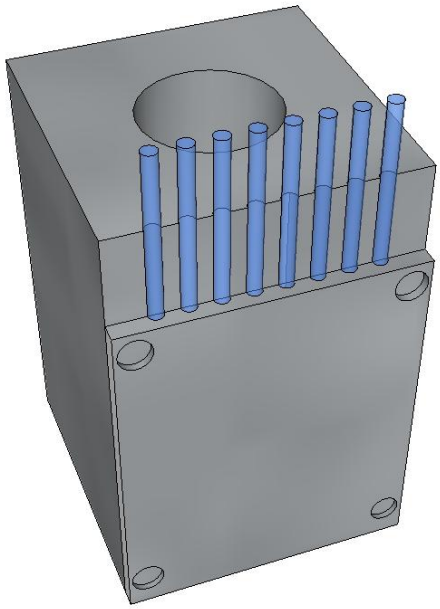

Figure 4.5: The fibre mount specifically designed to machine 10 fibres in parallel. A magnetic high precision mount allows for quick and easy removal.

A fibre mount (Figure 4.5) specific to the fibre-top cantilever machining approach shown in Figure 4.4 was designed and manufactured. It allows mounting of ten fibres parallel to each other. They are held in v-grooves by a metal plate. The mount has a hole in the centre allowing it to be used for FIB machining as well. The distance between the fibres is 2 mm. This mount can be used to speed up the machining because it is a sequential process, first the top sides are machined, then the entire block is rotated and the next step can be carried out for all fibres before rotating it again and carrying out the next steps and so on. This is useful because the rotation is carried out using a rotational stage and the fibres (depending on their length) are not always exactly in the centre of rotation. With a known distance

between the fibres finding the part of the fibre that needs to be processed is much more straight forward than carrying out the rotations for each fibre in turn, since the rotation is controlled manually and not as precise as the translation which is carried out by motorized stages with high precision.

4.2 Defining the processing parameters window

The influence of the laser parameters must be understood and optimised in a simple configuration to simplify the entire manufacturing process without other complicating factors. This section is about the laser parameters. The first decision that needs to be made is with regards to the best wavelength to use to manufacture fibre sensing structures. Some influence of the wavelength was already discussed in chapter 3 when micromilling of fused silica was investigated. It was found that the green and IR wavelength are more effective in terms of material removal rate. Optimization of power is also crucial for the best machining quality (reliability, cracking and surface roughness). It is well known that high power leads to higher removal rates and therefore speeds up the process but lower surface qualities are achieved, which means that the power or pulse energy is a parameter that needs to be tuned within a certain window for ideal processing. A study of the relationship between tapering angle and pulse energy is also included in this section.

4.2.1 Wavelength

One of the first decisions to be made when laser processing is to choose a wavelength and here are several factors to be considered: The cost per watt is often the most important factor for mass manufacture, however the cheapest laser power does not always achieve the best result, and whilst sometimes this can be overcome by increasing the power further this is not necessarily the case. Sometimes better results can be achieved when some energy is lost during the conversion to other wavelengths which might machine the material more efficiently. The laser used has its fundamental wavelength at 1030 nm and also offers the possibility of doubling or tripling the frequency giving wavelengths of 515 nm or 343 nm respectively, the doubling process is up to 60 % efficient giving a maximum output power of 30 W

compared with 50.5 W at 1030 nm. The tripling process is only 30 % efficient with a drop in maximum output power to 15 W. The absorption of any material varies significantly with wavelength. Transparent materials are only weakly absorbing at lower power levels in the visible range of light hence the main absorption effects in this range are typically non-linear and hence are strongly dependent on intensity. Absorption in the germanium doped core of this single mode standard fibre (SMF-28) can be achieved in a two photon process for 343 nm, in a 4 photon process for 515 nm and a 6 photon process for 1030 nm, however because these are non-linear processes the likelihood decreases exponentially with the number of photons involved [11], hence it is much easier to access these non-linear absorptions if frequency-tripled light at 343 nm is used. The cladding of the fibre is made of high purity fused silica with a bandgap energy of 9.3 eV compared to the lower 7.2 eV bandgap of the Ge doped core. This means that for the cladding the ionization process requires an 8 photon process for 1030 nm, a 4 photon process for 515 nm and a 3 photon process for 343 nm. These values are more important than those of the Ge-doped core because material from the entire fibre is being removed.

To determine the wavelength that was to be used for manufacturing the cantilever a series of cuts of the optical fibre was carried out. Simulating the cut underneath the cantilever shown in Figure 4.4(c) the fibre was cut from the the side by removing a volume of material. The laser beam was scanned across the surface of the fibre by scanning it in lines with a spacing of 3 µm. The laser repetition rate was kept at 40 kHz and the laser beam was moving with a speed of 30 mms^{-1}. The tapering angle and the cutting quality (occurrence of cracks) were the main subject of this series of experiments. The importance of the tapering angle and how well it can be controlled is important for the application as an optical sensor, as discussed in section 4.2.3.

With infrared light the fibre was found to crack at the bottom of the cut as shown in Figure 4.6(a).

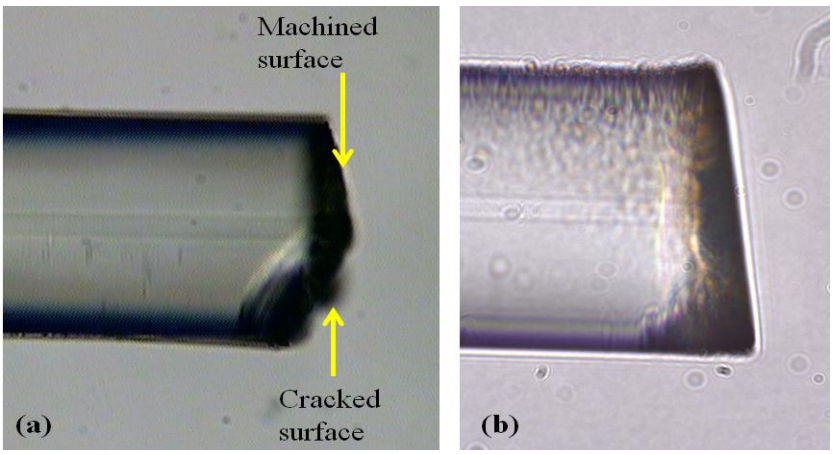

Figure 4.6: a) Fibre machined with infrared laser incident from the top, showing good machining on the top while the bottom part cracked; b) fibre machined with UV, no obvious cracking of the fibre.

The machining that was carried out with 515 nm cracked in 8 out of 45 cuts, hence being more reliable. The most reliable machining was achieved with the 343 nm wavelength, this is related to the smallest spot size and the fact that less photons are required to remove the material. The cracking using 515 nm occurred randomly and no relationship to the power used could be found. A strong variation of tapering angle ± 2 º makes it almost impossible to correct for the occurring tapering angle.

4.2.2 Pulse energy/Fluence

The pulse energy, average power and fluence are inter-dependent and also clearly important. It is well known that higher average powers lead to a higher material removal rate, which is a good thing for rapid machining especially in an industry oriented process. However there is usually a trade off between removal rate and machining quality (resolution and surface roughness), as shown in chapter 3 with the bulk samples. Often the process efficiency drops with higher energies. In chapter 3 ablation threshold measurements carried out on fused silica are described, which provide an ideal starting point for machining optical fibre as the material is identical. However tests on fibres are also very important as the cylindrical geometry and the small diameter of the sample can have an effect, especially during the 'side machining' process. All studies presented here were carried out by scanning the laser

beam, which replicates later machining better than single spot ablation, and pulse accumulation is accounted for. To determine a realistic range of powers that can be used for machining we investigated the first step of the fibre top cantilever machining process (Figure 4.4(a)), varying the power used to machine the ridge. The beam was scanned across the cleaved top surface of the fibre, using average powers ranging from below the single shot ablation threshold to the highest power available from the laser. Three different regions can be identified: (i) too low power, resulting in partial machining on the top and cracking deep inside the fibre (Figure 4.7 a). It is likely that the cracking is caused by self focusing and the top machining by thermal accumulation effects; (ii) correct power yielding controlled machining on the top, layer by layer can be removed and no visible cracking occurs (Figure 4.7 b); too high power while machining from the top, excessive energy is deposited in the thin ridge causing it to crack (Figure 4.7 c).

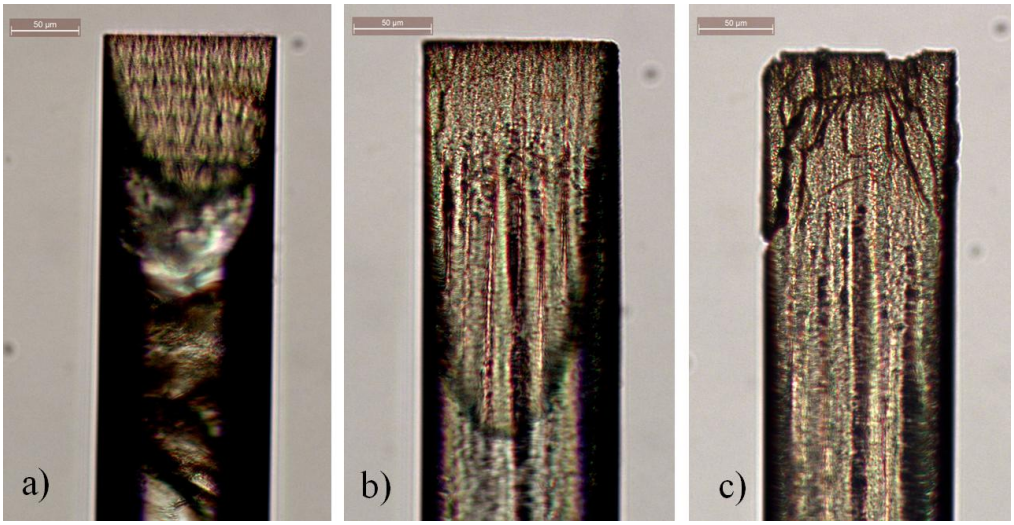

Figure 4.7: Top machined fibre at 3 different fluences, a) 6 µJ, 3.9 Jcm^{-2} fluence; b) 10 µJ, 6.5 Jcm^{-2} fluence and c) 16 µJ, 10.4 Jcm^{-2} fluence.

4.2.3 Tapering angle

Tapering is inherent to many laser machining processes and is dependent on the laser wavelength, pulse length, energy, focussing conditions etc. In some cases it can be

avoided, reduced or corrected for [12, 13]. In our process the existence of the tapering angle can be used as a positive effect when machining the ridge, as it reflects the laser light away from the important core area of the fibre. However when machining the cantilever it is important that the inner surfaces are as close to parallel to each other as possible. An angle of up to 3 degrees is acceptable according to the geometries and the NA of the fibre.

The depth of the ridge is strongly dependent on the fluence used to machine it, as can be seen in Figure 4.7 in which different fluences are compared. Machining the fibre from the side, simple end cuts were made with varying pulse energies. The taper angle for UV machining is plotted as a function of fluence in Figure 4.8, highlighted is the crack free machining range. For low fluences below 2.8 Jcm^{-2} the fibre was not machined all the way through.

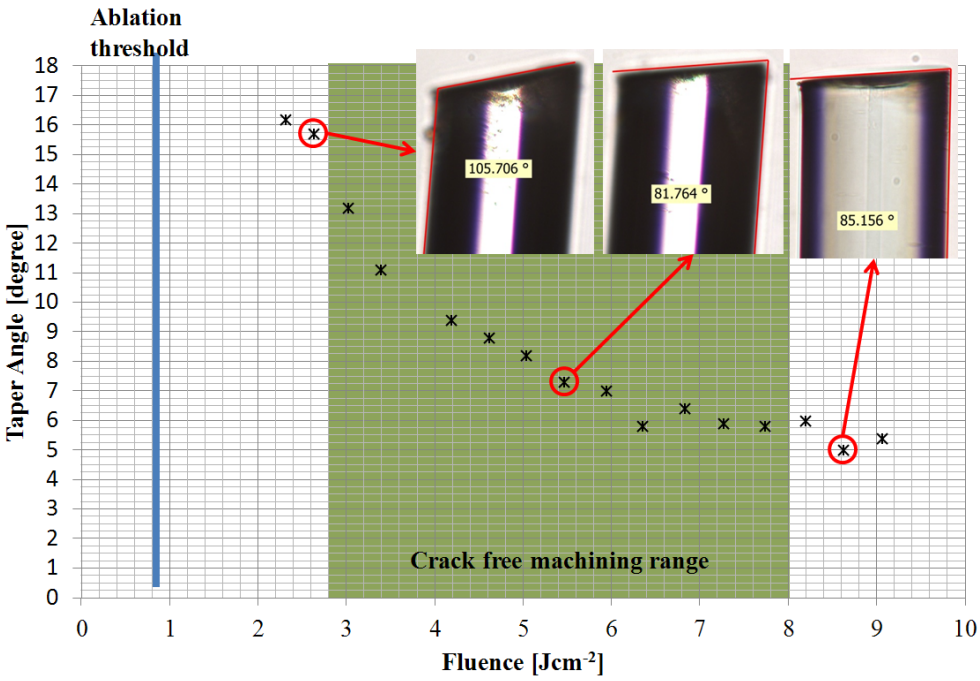

Figure 4.8: Dependency of tapering angle on the fluence used to machine the fibre for UV.

Focussing below the surface can have the effect that the fluence level is maintained into deeper machining ranges and this might lead to a reduction of the taper angle. However, defocusing did not have such an effect with the optical fibre.

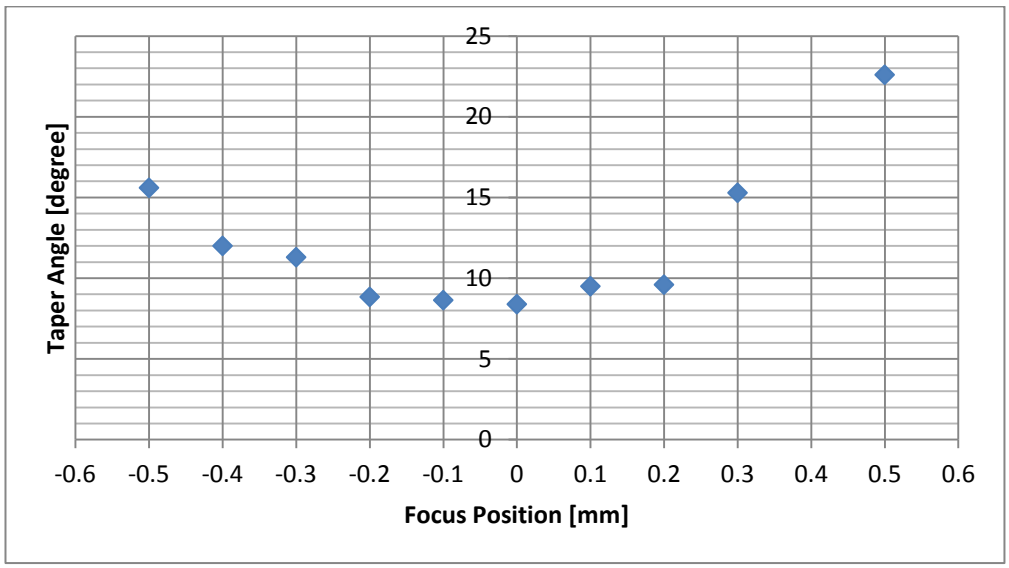

Figure 4.9: Taper angle as a function of focal position for optical fibre machining, where a negative focus corresponds to a focal plane below the fibre surface. Pulse energy kept constant at 6.5 µJ.

This movement of the surface relative to ideal focus position changes the spot size and therefore the fluence. The data shown in Figure 4.9 is therefore re-plotted in Figure 4.10, where taper angle is shown as a function of fluence. Also plotted for comparison are data recorded for different fluences but the same focal position.

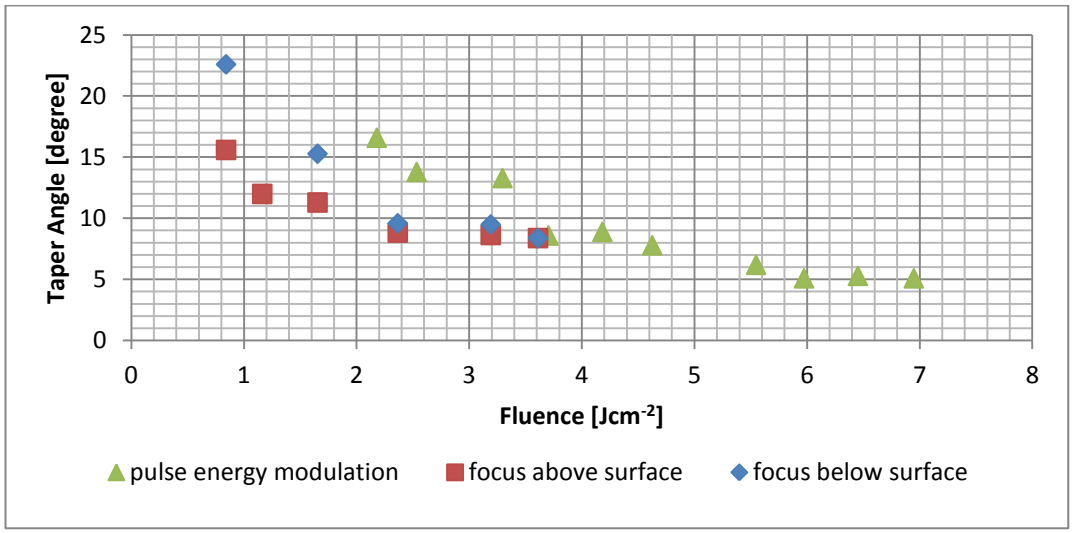

Figure 4.10: Fluence modulation by different methods. Triangles represent a fluence altered by changing the pulse energy, for red squares the fluence change is achieved by focussing above the surface; diamonds represent focussing inside the fibre.

This type of study is fairly repeatable in the UV and none of these fibres showed significant cracking whereas at other wavelengths cracking occurs as mentioned in 4.2.1. The same test was carried out for Green (Figure 4.11) and IR. With IR almost all of the fibres cracked and measurements of the tapering angle were not possible. With the green wavelength many fibres experienced cracking and the variation of tapering angles at similar fluences is about 4 °± 2 °, more than twice as large as with the UV indicating that the process is unstable and repeatable, and so correcting for the tapering angle is almost impossible.

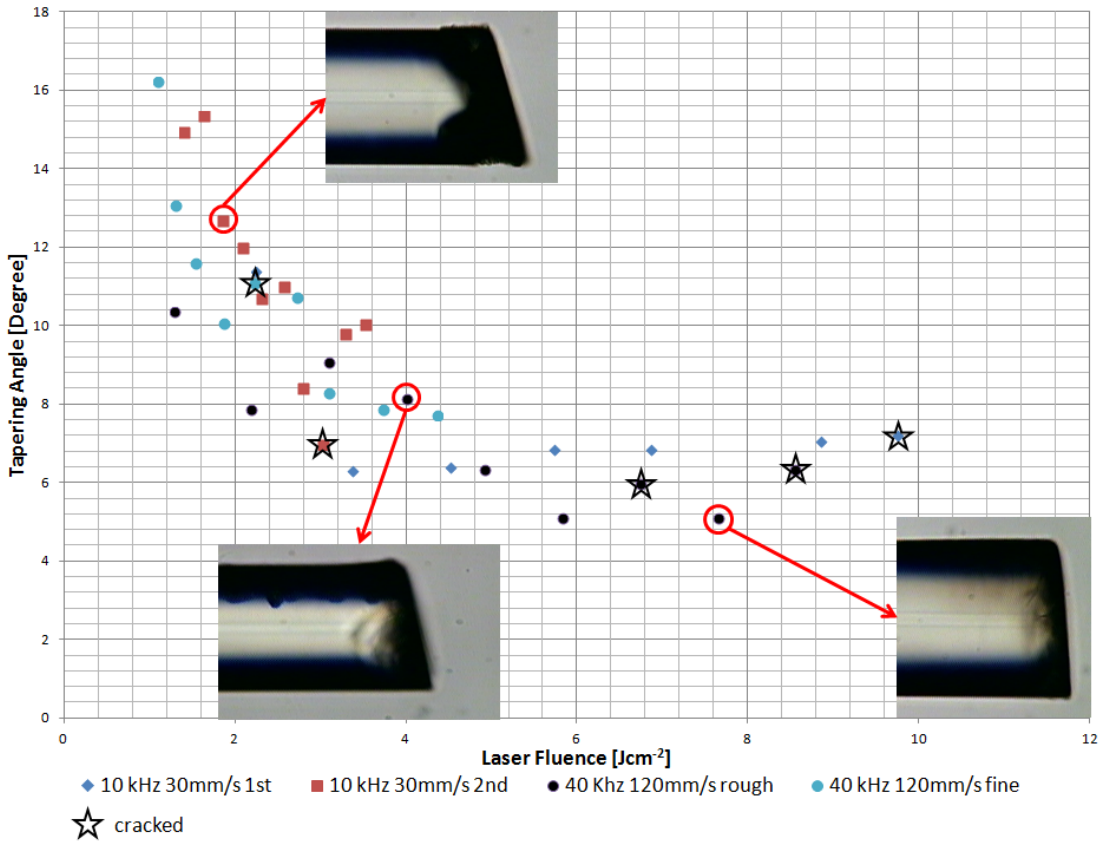

Figure 4.11: Taper angle as a function of laser fluence, machining optical fibre with 515 nm (green). The different colours and shapes of markings indicate experiments that were carried out on different days.

4.3 The fibre top cantilever machining process

In this section each step and the developments taken in the actual machining process are explained, further details on the machining parameters are given and some intermediate process steps are explained in more detail.

4.3.1 Establishing a ridge

The approach to manufacture these fibre top cantilevers was explained earlier, in section 4.1.2. In this section I will examine every step and compare the theoretical approach with the actual machining that is taking place. The first step is to manufacture the ridge. The two different approaches to manufacture the ridge on the fibre end are shown and the problems are discussed.

4.3.1.1 Manufacturing the ridge using only 'side-machining'

In this approach all the laser machining steps are carried out from the side. It offers the advantage of fairly simple alignment with a single axis of rotation along the core axis of the fibre. It is important that the fibre does not move out of the focal region during rotation. Initial trials used a fibre rotator (Thorlabs HFR007) mounted on the 3-axis translation stage system, but later the fibre rotator was exchanged for a more advanced holder mounted on a two axis goniometer to allow more accurate correction of the tapering angles. A ridge machined using this approach is shown in Figure 4.12. Very well defined and sharp edges at the bottom of the ridge [Figure 4.12 (b)] are possible. The ridge is tapered with one thick (36 µm) and one thin (16 µm) end and its height is 35 µm. Although the geometry of the ridge is well defined the cracks which are visible Figure 4.12(c) make it impossible to produce a stable cantilever with this ridge.

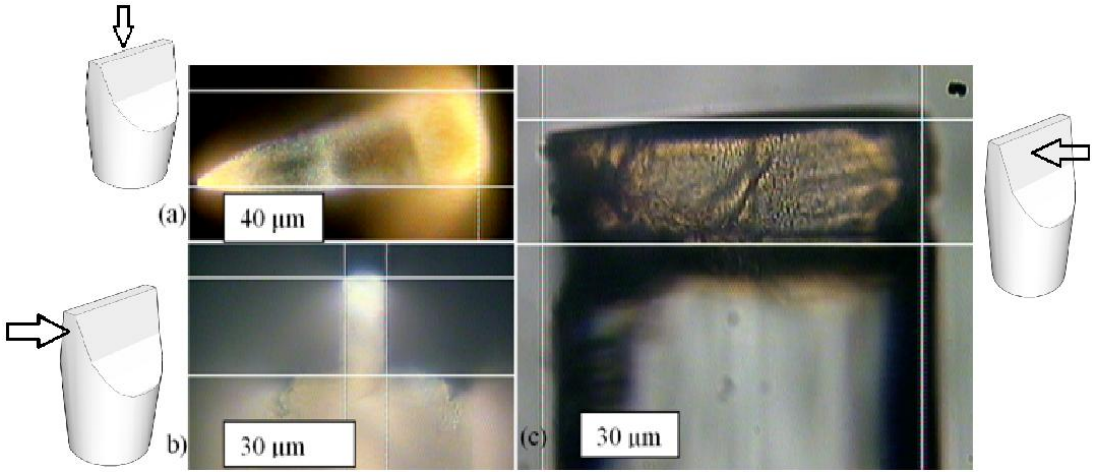

Figure 4.12: Micrographs of a ridge machined on a fibre end using the purely side machining approach at a pulse energy of 6.62 µJ. (a) top view indicating the effect of the tapering angle when machining the ridge from the side; (b) side view showing the well defined geometry with sharp corners at the bottom the graticule shows dimensions of 16 µm width and 33 µm height; (c) side view showing the cracking that occurs in the ridge.

For sensing applications these cracks are fatal as the cantilever might just fall off when the cantilever is actuated and the mechanical response is not as predicted. This cracking is very likely due to the scan heads not being optimized. They become stationary at either the beginning or the end of each machined line causing an accumulation of heat which results in an introduction of stresses and ultimately cracking. In some cases it was still possible to machine a cantilever out of such a ridge (Figure 4.13). Some cracks in the cantilever are visible. Sensing was demonstrated with a cantilever of this type indicating that picosecond laser machining is a viable route to creating a fibre cantilever sensor. However due to the cracking and unreliable machining this approach was not investigated further. The idea of top machining was therefore developed, and this more successful approach was used for further studies. It might have been possible to further optimize this process and make it work, but correction for the tapering angle would have made it more complicated than the top approach.

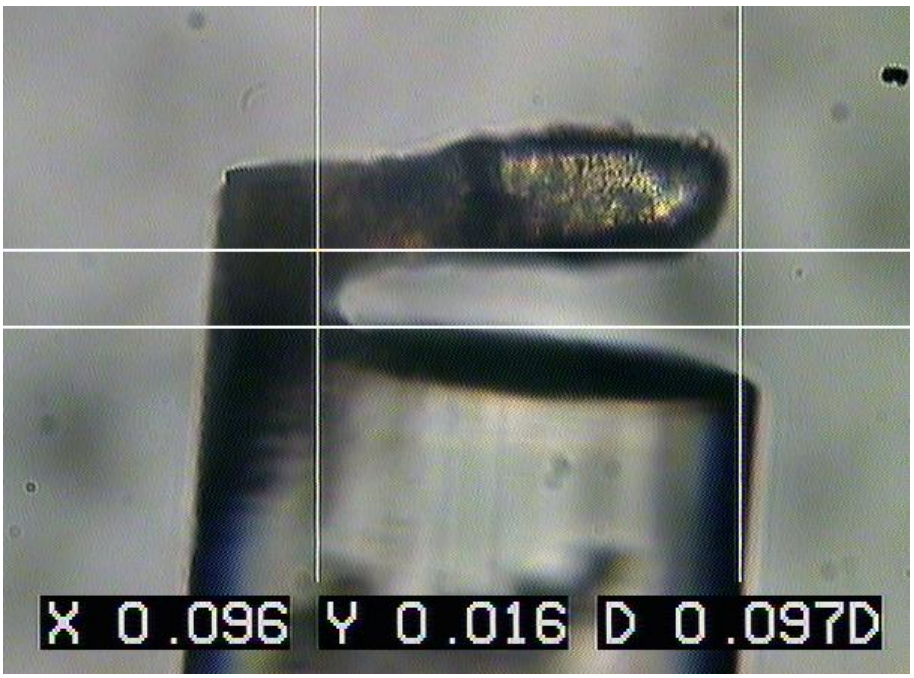

Figure 4.13: A cantilever that was manufactured out of a ridge machined with the side approach.

4.3.1.2 Machining a ridge from the top

A solution to overcome the cracking is to machine a ridge from the top. The initial thought was to stop the machining process after a ridge of height sufficient to machine the cantilever was established. However because of the speed of the process and a higher repeatability we left the machining to run until a wedge shape similar to a flat blade screwdriver has formed at the end of the fibre (see Figure 4.4). The following sections will explain and show all the steps to machine a ridge.

4.3.1.3 Evolution of the ridge

By scanning the laser beam across the cleaved surface of the fibre and removing a small amount of material with every pass the ridge starts to develop. To determine how much material is removed in every pass, the process was interrupted after 1, 5,

10 and 25 passes and pictures were taken at each of these steps which are shown in Figure 4.14.

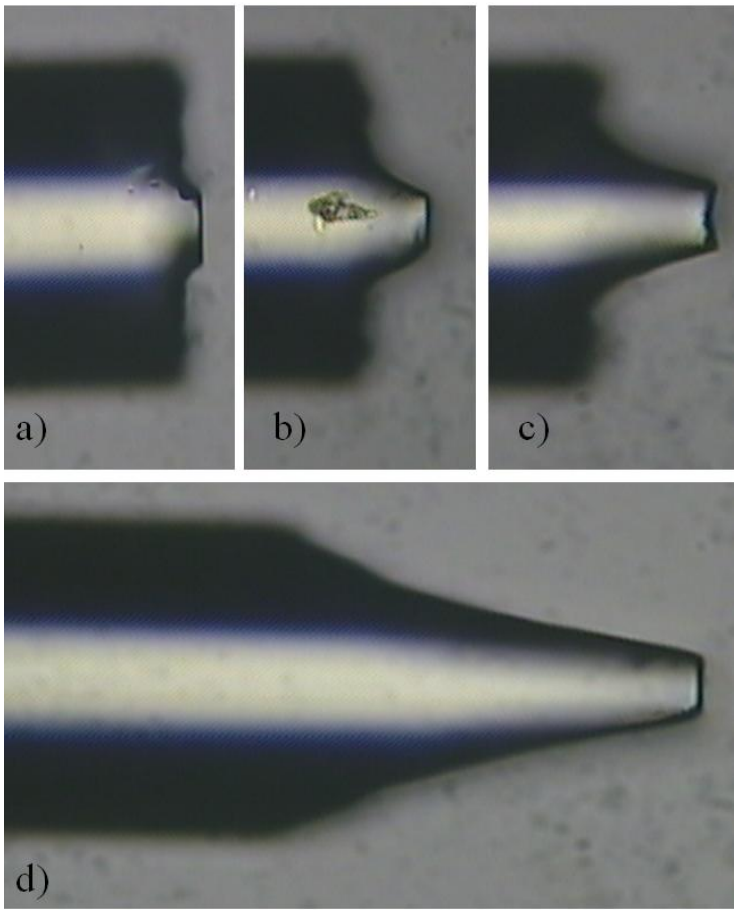

Figure 4.14: Evolution of ridge shape through various repetitions of laser machining pattern keeping constant focal plane and a fluence of 0.9 Jcm, a) once, b) 5 times, c) 10 times, d) 25 times.

On average in these experiments the first passes remove each about 10 µm. The further the machining progresses the less material gets removed, this is mainly due to the energy spreading over a larger area as an angled surface is generated, reducing the fluence, leading to less efficient machining. In addition to that the beam size changes with deeper machining, due to the machining plane moving out of focus, but on the scale of the height of the ridge this enlargement does not have a big effect. As shown in Figure 4.9 the tapering angle does remain almost constant over a range of 600 µm around focus and therefore the height of the ridge is not influenced by this defocusing effect. The height of the ridge can be changed by altering the tapering

angle and as mentioned in sections 4.2.2 and 4.2.3 this can be done by varying the pulse energy. As expected the behaviour is similar to the tapering angle experiment. The values that can be used are limited by cracking at low and high powers (see p110). When plotting the ridge height as a function of fluence the graph appears to be logarithmic [Figure 4.15 (a) and (b)]. This relationship is expected from the ablation threshold behaviour, where at higher fluences the depth of machining follows a logarithmic function. We can calculate the threshold from the linear regression fit, giving a value of $F_{Th} = 1.0 \pm 0.1\ J\,cm^{-2}$, matching the values found in the ablation threshold measurements, see chapter 3. This confirms that the fibre material behaves similarly to a bulk fused silica sample.

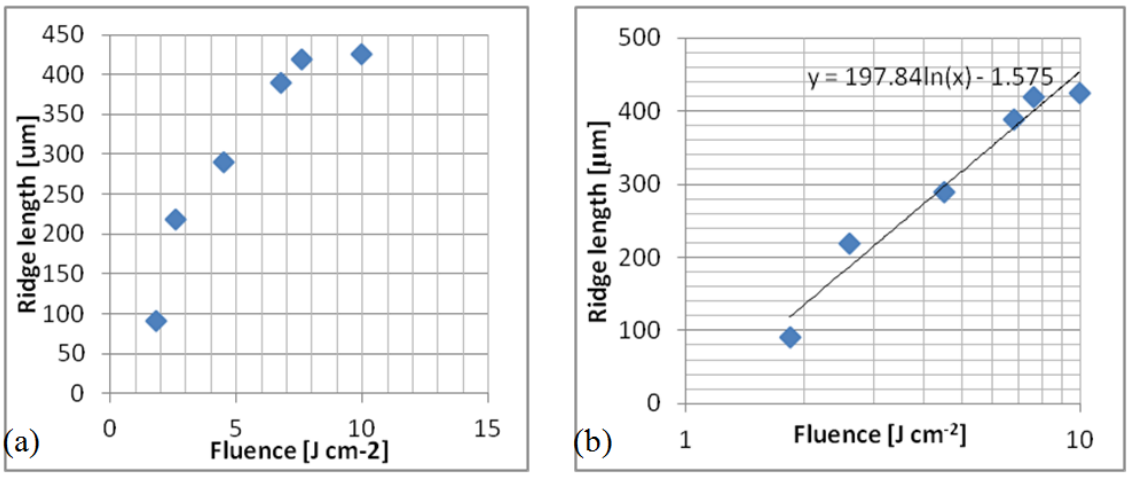

Figure 4.15: The ridge length is depending on the laser fluence, experimental data plotted with a linear fluence axis (a) and a logarithmic fluence axis (b), the line indicates a logarithmic fit to the function as would be suggested when comparing to the theory for ablation thresholds.

A fluence of 4.2 Jcm^{-2} was chosen to avoid the surface cracking observed at high values of fluence and the internal cracking observed at low values (section 4.2.2). This results in a tapering angle of 10 °, producing a ridge height of 297 µm. This is longer than necessary, but does not have any detrimental influence on the ridge, and indeed provides more parallel surfaces for machining the cantilever.

4.3.1.4 Debris reduction on the Ridge

It is very important to minimize debris re-deposition on the fibre end face as this is one of the optically active surfaces during sensing. In addition any debris could prevent the bio-chemical coating required for some sensing applications from adhering to the surface of the cantilever. The most common technique to minimize debris during laser machining is to use some kind of gas flow over the machining area. The easiest way to achieve this is by using a fume extractor causing a low velocity air flow across the machined surface removing any airborne debris. This technique however showed only little improvement over machining without any air flow [Figure 4.16(a)]. Although some of the largest debris particles were removed a layer of firmly attached debris remained [Figure 4.16(b)]. With an increased gas flow velocity it was thought that more debris would get caught and less re-deposition take place however the increased velocity caused the fibre to vibrate during machining causing damage and an increase in debris deposition [Figure 4.16(c)]. The third technique used ultrasonic cleaning in an isopropanol bath which removed most but not all of the debris [Figure 4.16 (d)]. The most successful method of was to use a piece of adhesive tape (3M scotch magic tape) and bringing the end of the ridge in contact with the sticky side of the tape. The debris sticks to the tape and when the tape is pulled off the debris is removed and the end of the ridge is as clean as the cleaved fibre [Figure 4.16 (e)]. This technique also adds a step to the manufacturing process and whilst it is easy to automate it still increases the complexity of the entire process.

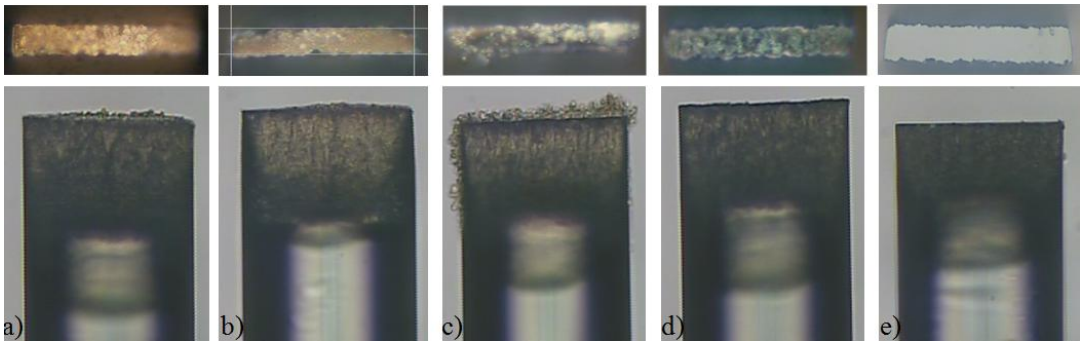

Figure 4.16: Comparison of five different debris removal methods. a) As machined; b) fume extractor close to the machining area generating an air flow; c) a nitrogen nozzle to have a higher velocity gas flow across the machining surface; d) after cleaning of a ridge in an ultrasonic bath with isopropanol; e) a ridge that was carefully brought into contact with sticky tape.

It is of course better to avoid debris deposition altogether. The direction of debris expulsion from a laser machining process is strongly dependent on the physical constraints of the surrounding unmachined material. Hence the order of machining e.g. overlapping lines is critical. Investigating the steps of the ridge production it was found that the automatic hatching method for machining started from one side and translated towards the centre and then from the centre to the outside, for further clarity this is shown in Figure 4.17. In addition to the impact on debris, this resulted in asymmetric ridges.

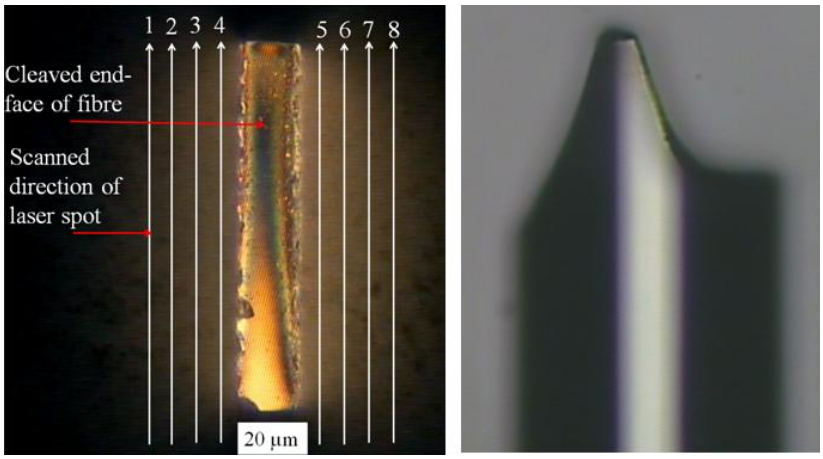

Figure 4.17: a) Top side of the ridge including indication of direction and order of the stadndard hatching pattern and order of lines and (b) the resulting asymmetric ridge shape in the sideview.

Symmetric machining patterns were therefore tested, with 3 different approaches; (i) Machining was alternated between one side of the ridge and the other for every single line, while the direction of the scan was always the same, with the first scan passing close to the fibre core [Figure 4.18 (a) and (b)]; (ii) Machining was alternated between one side of the ridge and the other, and the direction of machining was alternated for every pair of scans, with the first scan passing close to the fibre core [Figure 4.18 (c) and (d)]; (iii) same as method (ii), only changing the

first scan to be at the outside of the fibre with successive scans closer to the core [Figure 4.18 (e) and (f)].

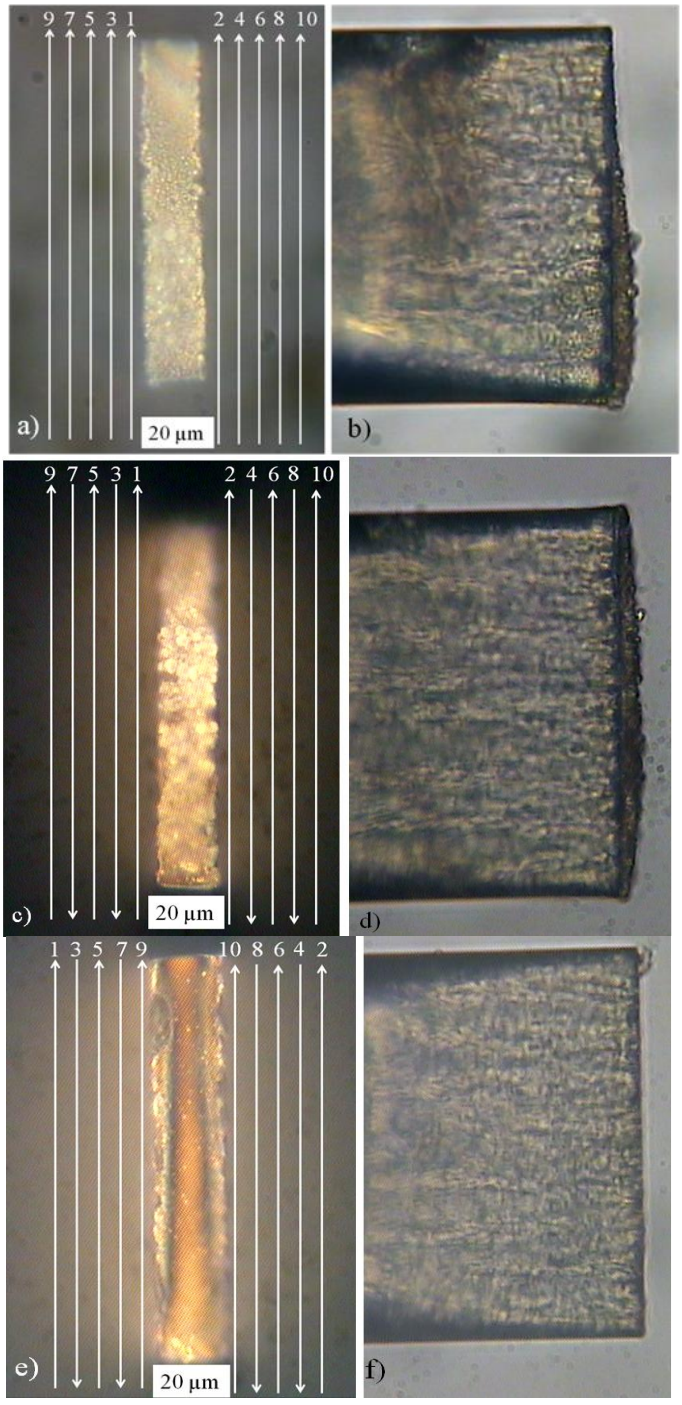

Figure 4.18: Effect of different scanning approaches on the machined ridge and the deposited debris. Top view (a) and side view (b) parallel scanning, alternating the side of

machining; Top view (c) and side view (d) alternating direction and side between each scan starting close to the later ridge; Top view (e) and side view (f) of a ridge machined with alternating direction of scan and alternating side of machining starting the first lines on the outside of the ridge.

All three of these approaches yield a symmetrical ridge shape, with both sides of a similar depth. The main difference is in the deposition of debris. In the first case [Figure 4.18 (a) and (b)] where all scans are moving from the same direction the debris is mostly deposited on the side of the ridge on which the machining started. A layer of debris with a thickness of 5 µm is visible in this case. The second case [Figure 4.18 (c) and (d)] meanwhile yields symmetrical debris deposition, with a debris layer of a similar thickness as in the first case. The third case is very similar to the second case only the starting point was changed to the outside of the fibre. This approach shows the lowest amount of debris while maintaining good properties on the ridge quality and symmetry. Only a few debris particles are visible on the end of the ridge, on the side view [Figure 4.18 (f)] no debris is visible suggesting a very good result. The high level of symmetry that can be obtained with this approach is shown in Figure 4.14 (d).

4.3.2 Cutting the cantilever

The finishing step of cutting a cantilever might seem simple however due to the special requirements for sensing it is very important to keep the surfaces of this cut as parallel as possible. The surface quality is also critical but it does not need to be perfect. If no steps are taken to avoid the natural taper during a cantilever cut the return signal is very low. Because of the strong taper with a single cut most of the light is directed outside of the fibre core area, and therefore the signal is lost or strongly reduced. A simple consideration of the geometries indicates that the light cone is not coupling back into the core area if the tapering angle is larger than 3° assuming a gap of 60 µm and a core diameter of 9 µm. A schematic drawing of the geometries is shown in Figure 4.19. Refraction of the diverging light at the exit of the core causes the light to leave at an angle, the reflection of the angled inside surface of the cantilever causes the light to be directed out of the core area.

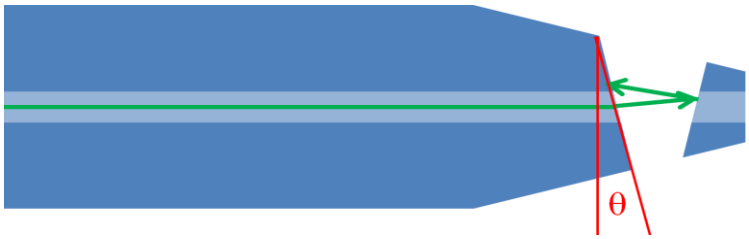

Figure 4.19: Schematic drawing of a cantilever made with a single cut, the core area is exaggerated in size. The lightpath is indicated in green and the taper angle θ is shown in red. A taper angle of just 3.3° causes the light to be not coupled back into the core, for a cantilever spacing of 30 µm

A typical cantilever that was machined only with a single cut has a strong taper as shown in Figure 4.20. The outside of the cantilever is still the cleaved surface and therefore a very smooth and clean surface. The structure shown in Figure 4.20 was corrected so that the tapering angle only affects one machined surface, if the angle remains uncorrected it affects both sides, the one towards the fibre and the cantilever inside. In this case the fibre was rotated to show the full tapering angle only on one surface. If no correction is done, the tapering angle is shared between both sides, the inside of the cantilever and the end of the fibre.

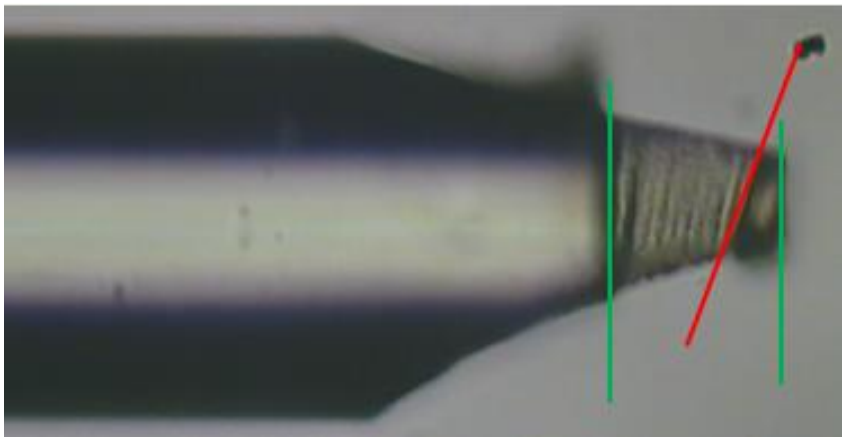

Figure 4.20: A cantilever machined with a single cut, tapering angle indicated by lines, view along the cantilever from the side of the fibre.

One solution to this problem is to machine twice, once on each side so that both tapering angles are removed however it gives rise to other problems. Such a rotation can be achieved using the goniometers or rotational stage. First of all the fibre is angled such that the cut to establish Figure 4.21 surface (B) is at 90 ° to the fibre axis. Then the fibre is rotated by twice the correction angle which is chosen according to Figure 4.8 and the end of the fibre [Figure 4.21 surface (A)] is corrected. With this machining approach the surfaces important for fibre optical sensing are made parallel.

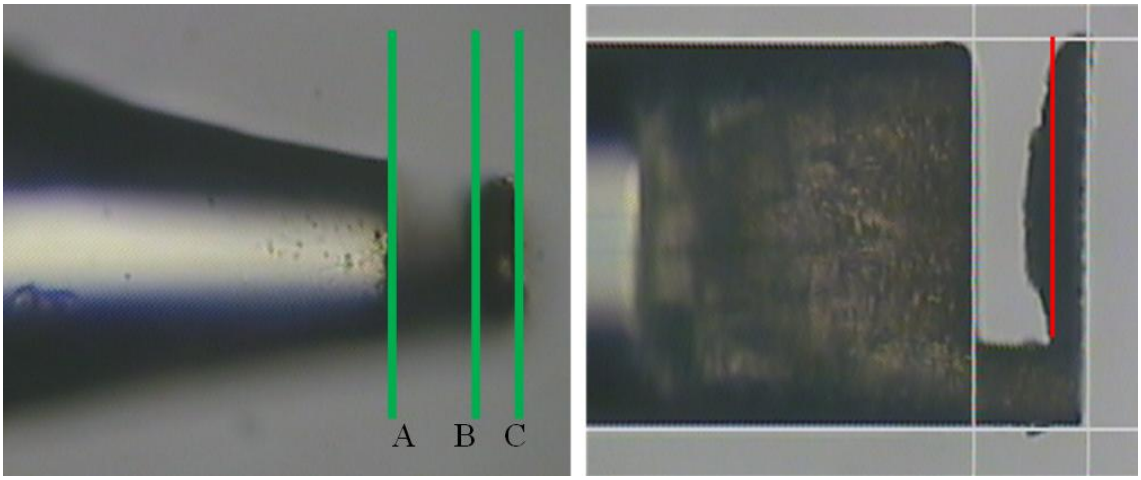

Figure 4.21: A fibre cantilever machined with correction on both inner surfaces, and (left) indication of parallel surfaces; (right) view rotated by 90 ° around the fibre axis showing the debris, and indicating the actual shape of the cantilever without debris.

During the machining of the second cut surface (A) debris is deposited on surface (B), a layer of up to 5 µm of debris is deposited. The debris deposition is directional in unconfined areas, when machining the second cut a 'spray' of debris is ejected in the direction of the cantilever. A solution here is to make two separate cuts, a thin structure in the centre between the cuts as shown in Figure 4.22, which shields the cantilever from the debris spray. No debris is visible on the inside of the cantilever.

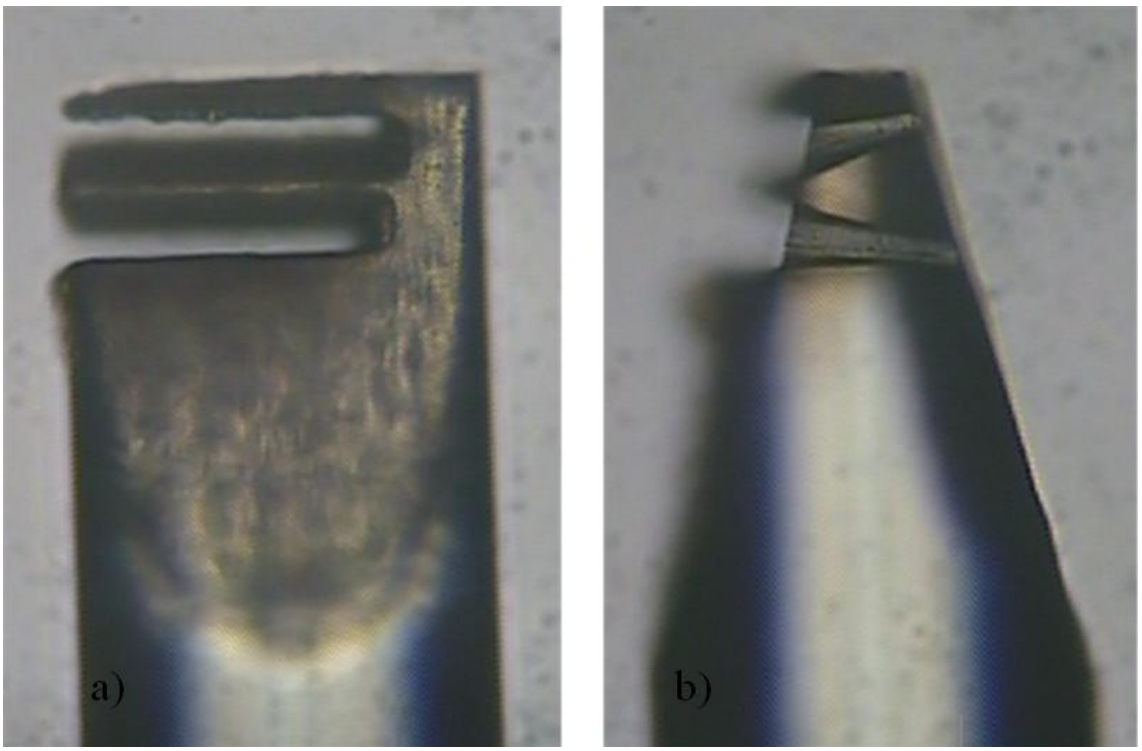

Figure 4.22: Microscope images of a micromachined cantilever and the central structure that catches the debris that would have been deposited on the inside of the cantilever.

The final cut removing the central structure is located close to the hinge area. This cut should be as small as possible to minimize the material that needs to be removed and that could be deposited as debris. An example of a finished cantilever machined with this technique is shown in Figure 4.23. The cantilever is very well defined with close to parallel surfaces and very little debris deposited. This type of cantilever was repeatably machined with a yield of more than 80 %. The 20 % failure rate is mainly due to a slight change in alignment with each batch, the first cantilevers of each batch being sacrificial to fine tune the alignment. Many of the cantilevers have been tested as sensors.

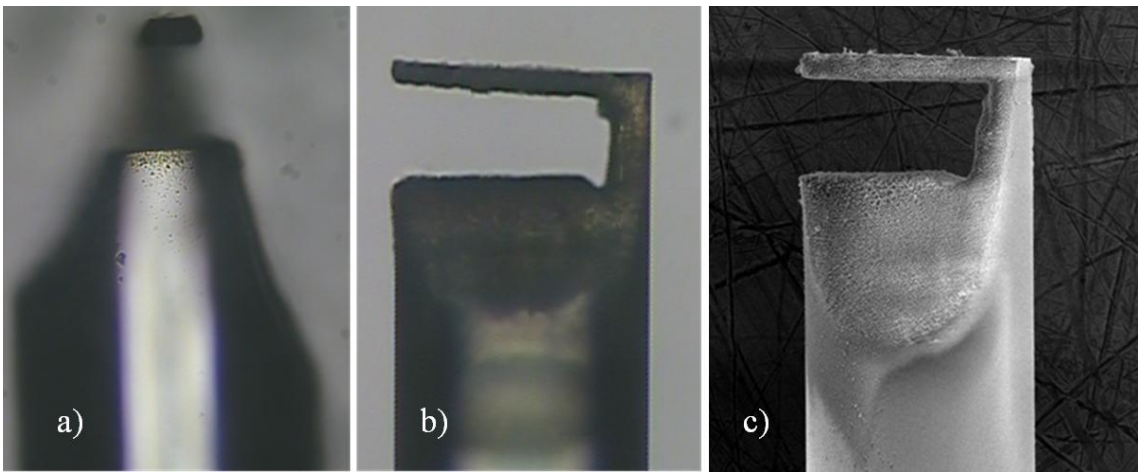

Figure 4.23: Finished fibre cantilever, machined with taper correction, and the central structure to catch the debris. It is 10 µm thick, 110 µm long. (a) sideview showing the amount of taper looking along the cantilever; b) and c) sideviews showing the length of the cantilever with a microscope (b) and a SEM (c)

To investigate factors that influence the quality of a cantilever sensor it is essential to show that an optical cavity exists and investigate the return signal. For a first analysis it is not necessary to deflect the cantilever. It is clearly important to also be able to move the cantilevers and sense the deflection and such an experiment is described in section 4.3.5. In paticular the returned intensity and the fringe visibility are important for sensing. The fringe visibility is calculated as

$$Visibility = \frac{maximum - minimum}{maximum + minimum} \qquad \textbf{(4.4)}$$

A typical cantilever machined with this technique achieves a very good fringe visibility in the range of 0.6 to 0.7. The total returned intensity however is very low typically below 3 % of the Fresnel reflection. Because the measurement is interferometric it relies on the change of cavity length and is in the first instance dependent on the fringe visibility. The reflected light intensity for a low finesse cavity as we have can be expressed by

$$I_R = \mathrm{I}_0 \left[1 + \mathrm{V} \cos\left(\frac{4\,\pi\,\mathrm{n}\,\mathrm{L}}{\lambda} + \varphi_0\right)\right]. \qquad \textbf{(4.5)}$$

Where I_0 is the incident light intensity, V the visibility and L the cavity length. The cavity length can be determined by analyzing the spectrum of the broadband light delivered through the fibre reflected from the cantilever using a Fast Fourier Transform (FFT). Alternatively a tunable laser source could be used. Some more details on the interrogation system can be found in section 4.3.5.

An example cantilever and the corresponding interferogram are shown in Figure 4.24. The measured cavity length in this case corresponds to the cavity formed by the cleaved surface and the end of the fibre. In many cases more than one cavity contributes to the interferogram. The FFT technique used allows several cavities to be distinguished and measured provided they are not too similar in size. In our case the thickness of the cantilever is typically 10 µm, therefore the optical path length inside the glass is in the order of 15 µm, whereas the gap between the cantilever and the fibre end is at least 20 µm because the laser cuts are >10 µm wide.

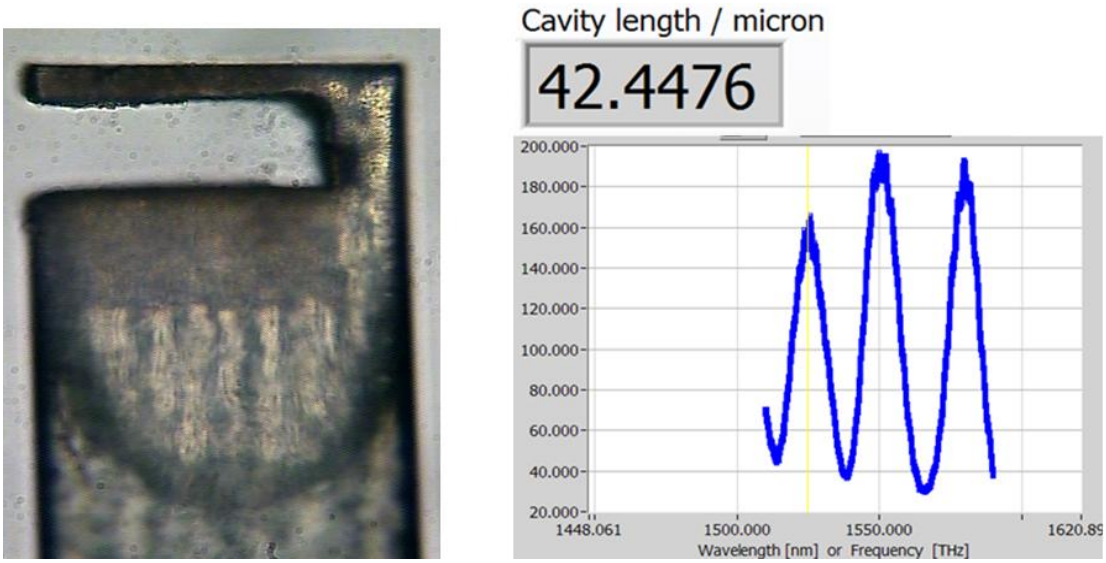

Figure 4.24: Picosecond laser machined cantilever and the corresponding recorded interferogram showing a cavity of 42.4 µm. This corresponds to the cavity formed by the outside of the cantilever and the end of the fibre. The maximum returned intensity of 200 units corresponds to only 3% of the Fresnel reflection, the fringe visibility is 0.73.

The interferogram shown in Figure 4.24 was recorded using a tunable laser source, which has a high intensity therefore the return signal was recordable, however with a lower-cost broadband light source (more suitable for a sensing application) the intensity is much lower, hence the return signal would be lower and the signal to noise ratio worse. Hence although the results presented above demonstrate successful production of a working cantilever sensor using a purely picosecond laser machining process, the return intensity was not sufficient for the low cost sensor incorporating a broadband light source. Hence some improvement of the surfaces is necessary to achieve a higher return signal intensity.

4.3.3 Improving the cantilever after laser machining

Improving the surface of laser machined glass parts is not easy, especially at this scale. Mechanical polishing techniques do not work. A technique that other groups used to polish microresonators that were etched out of glass was to expose the structure to the light from a CO_2-laser which is strongly absorbed within a few microns of glass, partially melting the structure and removing the surface roughness of laser machining [14]. However, because this involves another laser and a complicated setup to mount the fibre in focus of the laser, a simpler technique is desirable. An alternative technique to locally re-flow the glass surface is to use an electric arc as commonly used for joining (splicing) fibre optics, this technique was also used on femtosecond laser machined microresonators [15]. A fibre optic fusion splicer (Beale International Technology BFS-50) can deliver an arc with a lower current than used when splicing two fibres. This can be done in the "cleaning" mode, which is used to prepare the fibres before splicing. The arcing time can be set in steps of 0.1 s and the current can be controlled in steps of 1 mA. A series of experiments was carried out in the fusion splicer which is equipped with a microscope to align the fibres, allowing changes to the shape of the cantilever to be monitored. If a very short time or a very low current was chosen no change was visible on the microscope or in the reflected spectrum. The sensing signal starts changing at currents higher than 8 mA although at this current times longer than 1 s are required. This effect is not necessarily beneficial, in some cases the signal dropped or was completely lost, probably due to melting and bending of the

cantilever leading to the signal being reflected away from the core area. However, with the same cantilever when a higher current was subsequently applied the signal reappeared and could even be improved over the inital intensity, presumably due to the cantilever bending back into place. There are two distinctive regimes: (i) for currents from 8 to 10 mA and short arc durations of less than 0.4 s the debris and dirt is removed while the shape of the cantilever does not change significantly and (ii) for currents higher than 10 mA and times longer than 0.5 s the shape of the cantilever changes significantly, probably due to the heat softening the glass and the cantilever melting. For a comparison of this process Figure 4.25 shows a microscope image of the cantilever and the spectrum of the cantilever directly after laser machining. The first regime results in an improvement of the signal intensity by a factor of 2 to 3 [Figure 4.26]. More than two or three short 0.1 s cleaning arcs of a current of 9 mA do not improve the signal further.

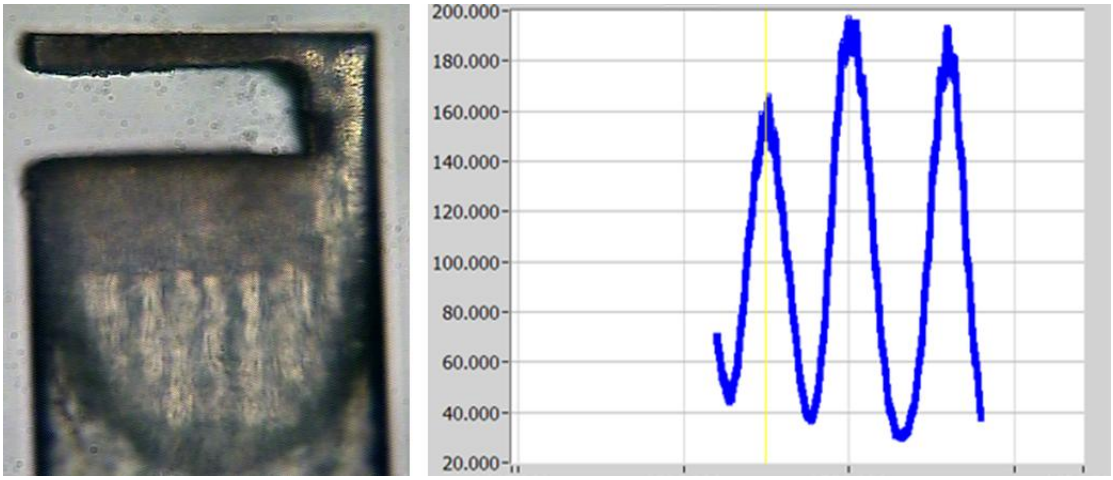

Figure 4.25: Reference cantilever and spectrum directly after laser machining. Maximum signal strength is 3% of Fresnel reflection, and fringe visibility is 0.73. The cavity length in this case was 42.5 µm.

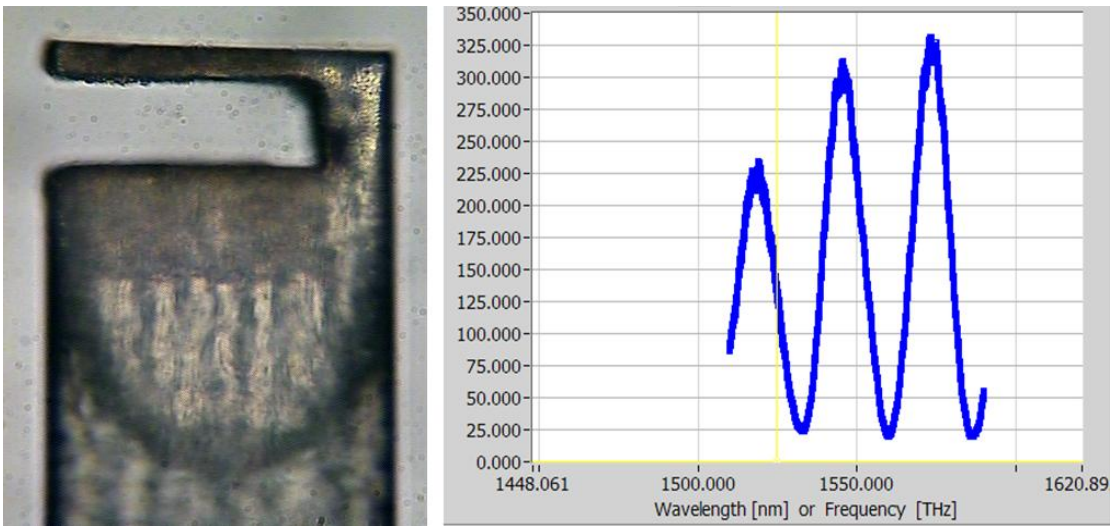

Figure 4.26: Cantilever structure after 0.1 s 9 mA cleaning arc was applied. The maximum intensity corresponds to 5.6% of Fresnel reflection signal, the fringe visibility is 0.89. The cantilever appears slightly more transparent. The cavity length is 43 µm.

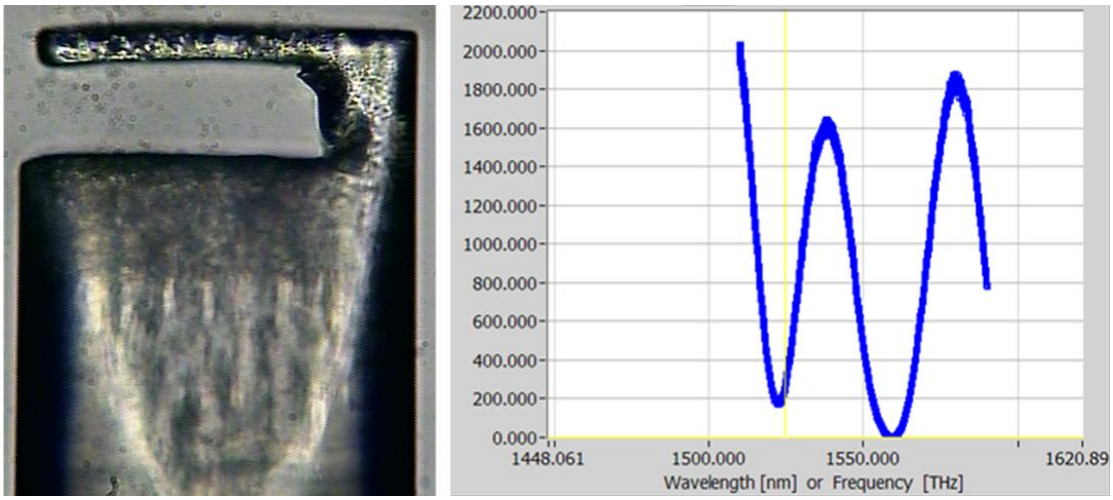

Figure 4.27: Cantilever that was arc cleaned with 8 cycles of a 0.7 s arc of 9 mA. The intensity of the signal is 30% of Fresnel reflection, and the fringe visibilty is higher than 0.9. The measured cavity length was 28 µm.

The second regime introduces a noticable change of the interferogram when an 0.7 s long arc is applied, [Figure 4.27]. The cavity size decreases due to the cantilever softening and changing its shape slightly. The optical scatter from the cantilever starts to disappear and a more specular image shows on the microscope. A sudden shift of the detected cavity size occurs, due to the surfaces that form the dominant

cavity shifting from the inital configuration in which the outside of the cantilever and the end of the fibre formed the cavity to the inside of the cantilever and the end of the fibre being the stronger signal. This typically occurs when the surface melts and a slight reflow causes the surface shape to change to be more uniform and the surface to be smoother. This melting also causes the taper angle to be reduced even further. If a too high current is chosen or the duration of the cleaning arc is too long the cantilever melts almost completely [Figure 4.28]. This has two effects, the length of the cantilever changes significantly as it decreases in length and gets thicker, but also the surface quality improves.

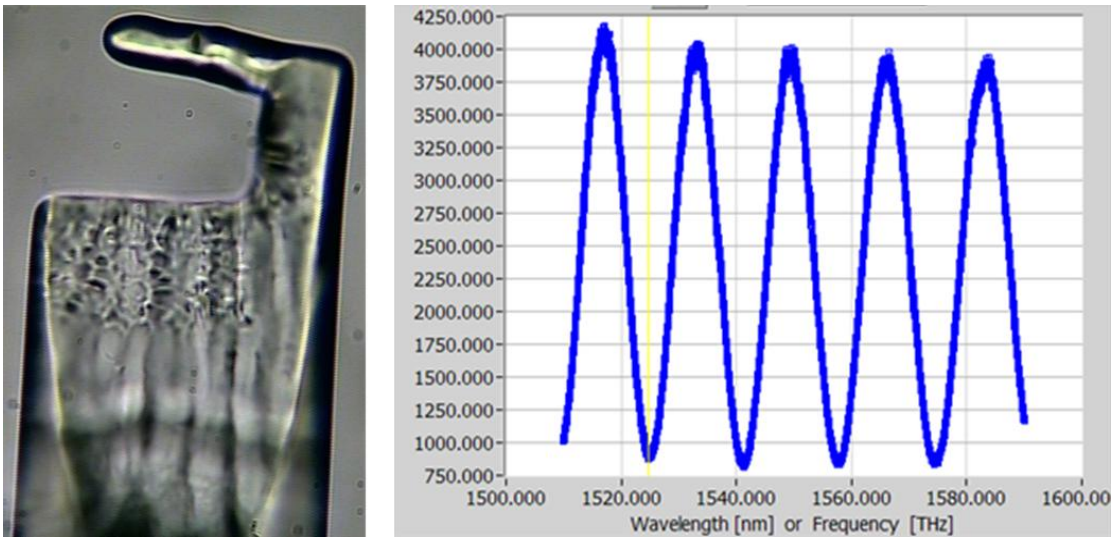

Figure 4.28: Micromachined cantilever that was arc cleaned for a duration of 1 s with an arc current of 15 mA. Causing the cantilever to melt and bend away from the fibre. Interferogram recorded from the cantilever. With an intensity corresponding to 90% of Fresnel reflection and a fringe visibility of 0.65.

While the interferogram seems desirable the shortened length and the increased thickness of the cantilever increase the stiffness of the cantilever reducing the possible applications. The best results, that do not compromise the performance of the cantilever due to the shortening effect whilst providing the best surface improvement are achieved by using multiple short arcs between 5 and 10 and a current between 8 and 10 mA.

In addition to improving the surface roughness this process also improves the strength of the cantilever. When trying to break off a cantilever by attaching a fibre with epoxy glue, the cleaned cantilevers were much more difficult to break off than the uncleaned. This probably had two reasons: (i) The surface of the cantilever is smoother therefore the contact area of the glue with the cantilever is less, hence the adhesion is lower; and (ii) the microcracks on the surface and stresses introduced by laser machining are likely to have been reduced due to an annealing effect during arc cleaning.

4.3.4 Investigation of the surfaces of the cavity and the influence of the arc cleaning process

In this section the surfaces that are important for sensing are investigated. Specifically the end surface of the fibre, the inner surface of the cantilever and the the outer surface of the cantilever, are labelled A, B and C in Figure 4.29. The measurements of the surface roughness indicate the quality of the surface and therefore provide an indication how well optical sensing of the cavity can be executed. The surface roughness is directly related to the surface scattering and therefore the reflected intensity. The measurement of the surface roughness is carried out by scanning the surfaces with an AFM probe, the measurement of roughness is then calculated along a line across the long axis of the cantilever as indicated by the line in Figure 4.29(middle).

To measure the change of surface roughness the various surfaces were examined with an AFM and a white light interferometer. The white light interferometer was the prefered measurement instrument because it offers the advantages of a much quicker measurement with a similar precision, also alignment is simpler and a larger area (60 µm by 90 µm) can be measured in the highest resolution compared to the maximum of 56 by 56 µm that can be measured with the AFM. The AFM was operated in contact-mode, this leads to errors when the tip approaches a steep edge or the fibre bends with the scanning tip. To align the AFM tip with the top of a cantilever is very difficult as the cantilever is less than 20 µm wide, and therefore not visible without aid. The magnification of the microscope that is built into the AFM is

also not sufficient to allow accurate alignment causing the AFM tip to hit the cantilever from the side during a scan and bending it rather than measuring the surface profile. Hence using the AFM to image the top surface of a cantilever top is a case of being lucky. For the inside of the cantilever (surface B) AFM images were not captured, because measuring the inner surface with the AFM while the cantilever was still attached was not possible, due to the difficult alignment and the space constraint environment. Also the white light interferometer does not work on the surfaces that were not arc treated due to strong scattering of the light.

4.3.4.1 Investigation of the inner surface (surface A)

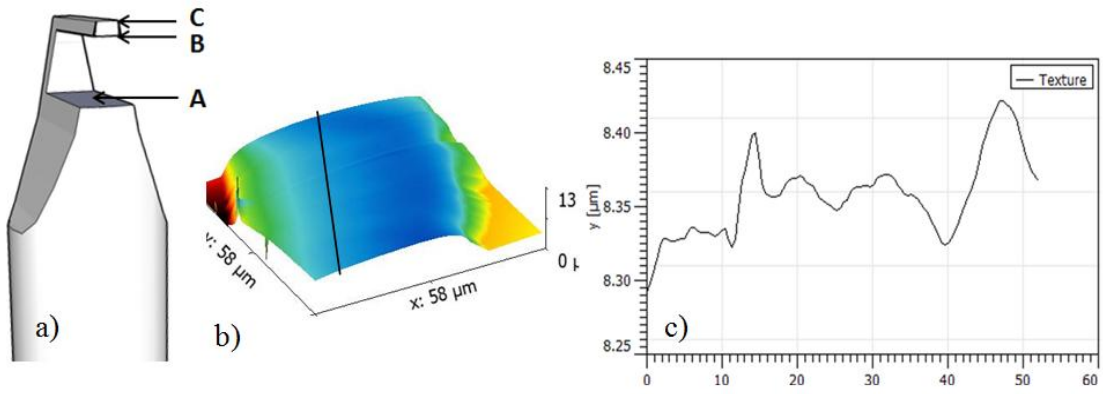

Figure 4.29: Image acquired through an AFM scan of surface A, which was cleaned with the electric arc technique. The surface roughness is 30 nm rms along the indicated black line which corresponds to the direction of the cantilever.

To compare the results obtained using the white light interferometer (Figure 4.30) with those from the AFM (Figure 4.31), measurements on surface A [Figure 4.29 (a)] were investigated with both the white light interferometer (Figure 4.30) and the AFM (Figure 4.29 (b)). The results show a slightly lower surface roughness R_q of 11 nm measured with the whitelight interferometer compared to the R_q 30 nm measured with the AFM. This is, however, not a significant difference given the fact that different samples were investigated. Several cantilevers were snapped off in order to take these images. Due to the difficulties of mounting the fibre for investigation with the AFM and the whitelight interferometer it was not possible to

investigate exactly the same cantilever, it was however possible to measure cantilevers that were machined in the same batch and hence identically processed.

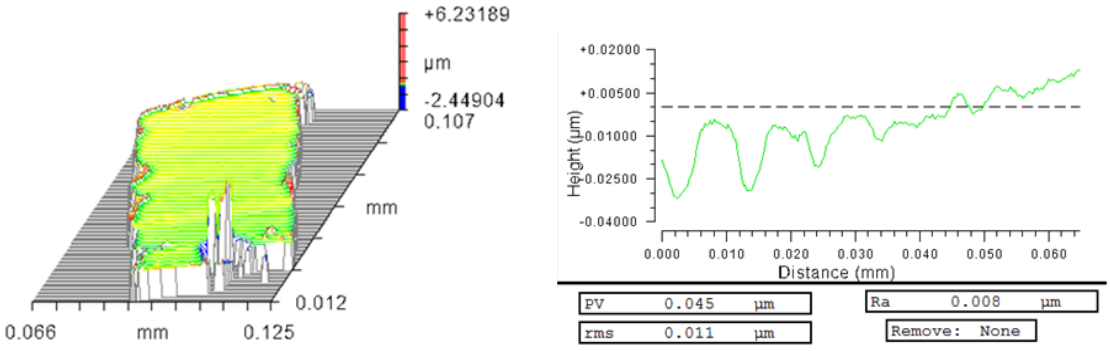

Figure 4.30: Topography of the inside of the cavity, surface A, after the arc cleaning process measured with the white light interferometer. The surface roughness R_q is 11 nm along the direction of the cantilever.

The surface of a cantilever that was purely laser machined (i.e. without the additional arc cleaning step) is much rougher than the surface of an arc cleaned structure. The surface roughness of an example surface A was measured with the AFM, the R_q roughness is 165 nm and the peak to valley height is 707 nm. This surface should be very similar in quality to the inner surface of the cantilever (surface B) as both are directly machined surfaces of similar geometries using identical laser parameters.

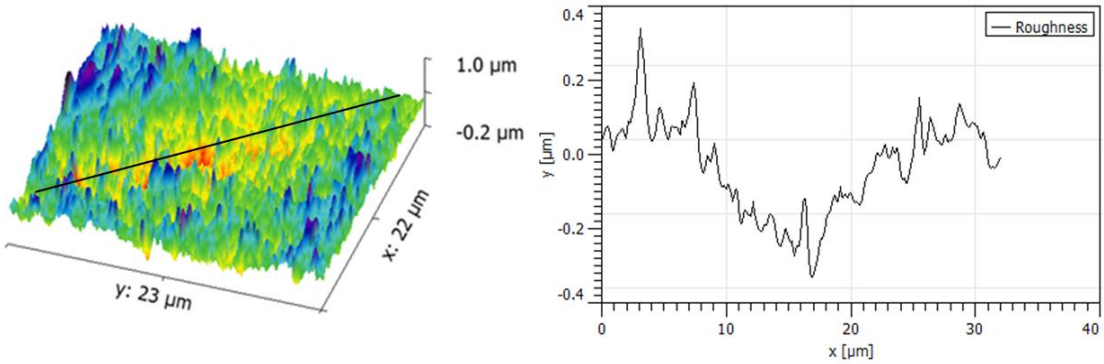

Figure 4.31: As Laser machined surface A. The profile shown on the right is measured across the diagonal of the image shown on the left. The R_q roughness is 165 nm.

More information about the directly laser-machined surface can be gathered by using an SEM. As shown in Figure 4.32 in the case where a cantilever was deliberately broken off, the structured surface of the laser machined cavity surface is clearly visible. It is not a smooth or polished surface as it would be expected from a melting process. Instead, it is a surface with structure in the order of 0.5 to 1 µm (Figure 4.32(centre)). Each of these structures consists of several smaller grains which are on the order of 50 to 100 nm (Figure 4.32(right)). The laser machined edges are sharp and the surfaces show very little waviness apart from close to the hinge. The final cut that removes the sacrificial structure seems to machine slightly into the bulk of the fibre. It is obvious that this surface finish will be highly scattering, as it is roughly on the scale of the interrogation wavelength.

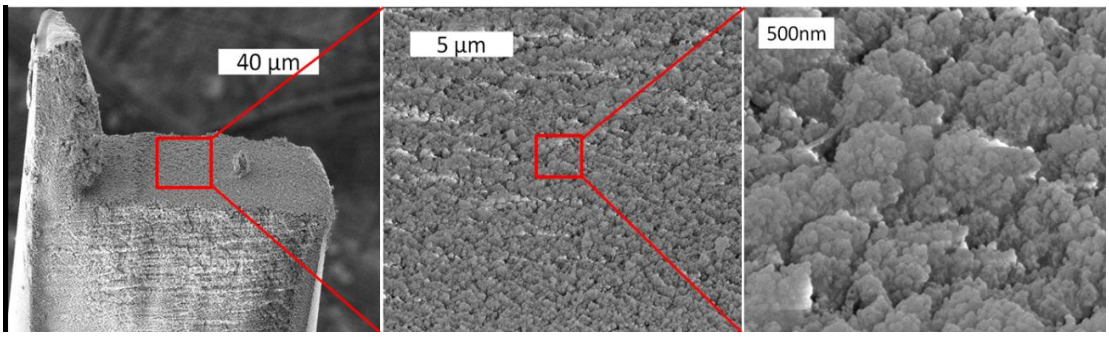

Figure 4.32: SEM micrographs of a fibre where the cantilever was deliberately broken off to allow access to the surface of the fibre; zooming into the machined area shows a rough structure with small clusters of debris.

4.3.4.2 Inside of the cantilever as machined and arc processed (surface B)

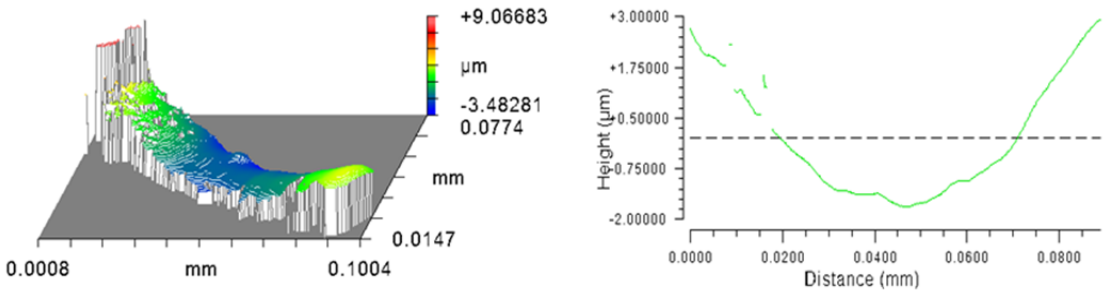

Figure 4.33: Inside of a cantilever that was arc cleaned showing the circular profile.

The inside of the cantilever (surface B) after arc processing shows a similar rounded profile (Figure 4.33) to the top side of the cantilever (Figure 4.37). In Figure 4.33 the inner surface of a fibre cantilever that was arc cleaned is shown. The problem with this profile of such a curved surface is that the surface roughness is not visible anymore due to the overall shape. A standard technique to still resolve the surface roughness from such a sample is to use a filter, to block long scale deviations of shape whilst passing small scale changes. This technique was only used on curved samples. By choosing a high pass mode with an appropriate low filter wavelength the general shape is filtered out and the roughness data remains. A Gaussian filter was used in this case, with a cut-off wavelength of 6.8 µm. The roughness profile after the filter was applied is shown in Figure 4.34. The surface roughness is only 28 nm rms, and whilst it is not as smooth as the outside of the cantilever it is significantly smoother than a directly laser machined surface.

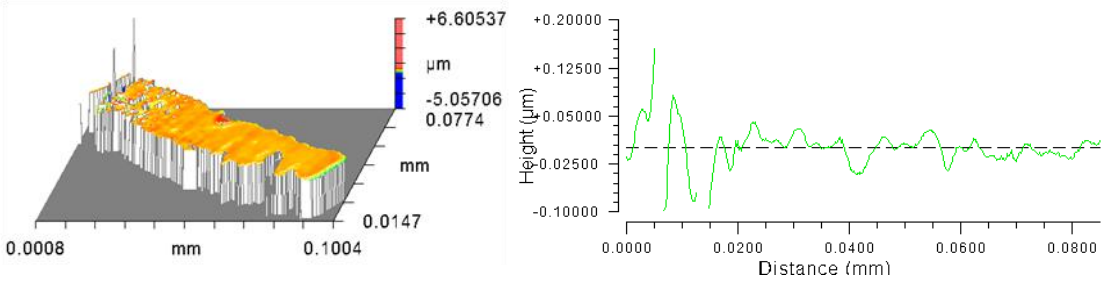

Figure 4.34: Roughness profile of the cantilever inside (surface B) after treating with an electric arc, and applying a gauss filter to remove the curved shape. The surface roughness is 28 nm rms.

Additional evidence of the changes to surface roughness and shape was found by using an SEM to investigate an arc treated cantilever, an image of which is shown in Figure 4.35. Apart from some dirt on the cantilevers the surface is clearly much smoother than the as-machined surface shown in Figure 4.39. Even at a very high magnification no grains can be resolved. Instead the images in Figure 4.35 show features typical of a melting process, smooth surfaces and rounded edges. However they are less flat, clearly as a result of surface tension effects.

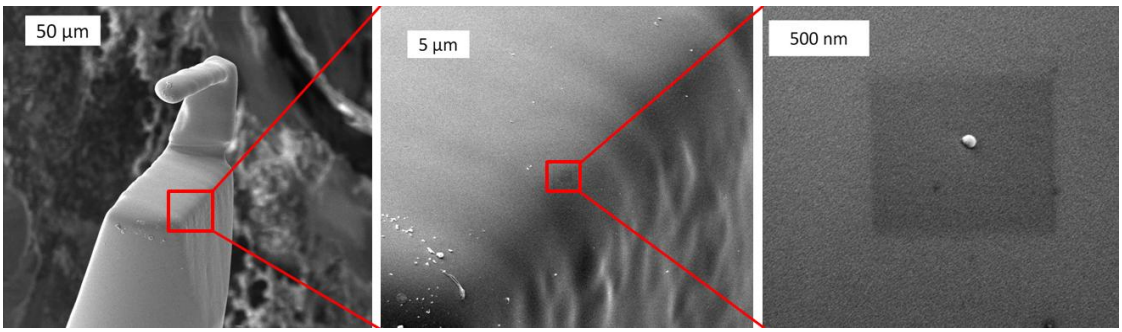

Figure 4.35: SEM image of an arc treated cantilever. It is obvious that the surface of the cantilever is much smoother, there is not the typical grain structure as seen on laser machined parts. A slight waviness is still apparent. The edges of the laser machined features are also smoothed.

4.3.4.3 Top surface of the cantilever (surface C)

The top surface might not be important for the sensing signal because it is not part of the sensing cavity, however for some applications it becomes very important because it is the surface that a functional coating can be applied to, and some coatings do not stick well on rough and durty surfaces. Hence this surface must be investigated as well.

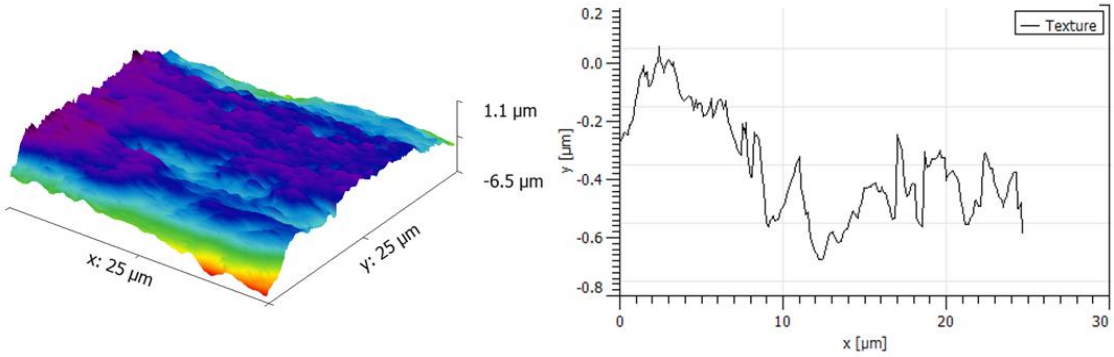

Figure 4.36: Top side of the cantilever (surface C) directly after laser machining measured with an AFM. The surface roughness is around 150 nm rms.

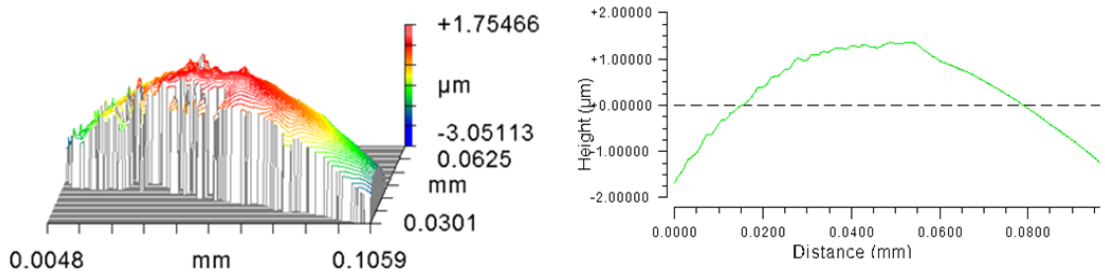

Figure 4.37: Top side of an arc cleaned cantilever (surface C). The cantilever bend means that the small surface roughness is not resolved in these images.

In Figure 4.36 the top surface (surface C) is shown directly after laser machining the image was taken with an AFM. Although this surface is the surface that was created by cleaving, the redeposition of machining fumes causes it to become rough. The arc that was used to clean the inside of the cavities shows effect here as well. In Figure 4.37 the top surface C is shown after it was arc cleaned, if the Gaussian filter is applied (as in section 4.3.4.2; cut off wavelength of 3.2 µm) the surface roughness is visible [Figure 4.38]. The resulting profile is shown in Figure 4.38, showing a low surface roughness of just 10 nm rms along the full length of the cantilever.

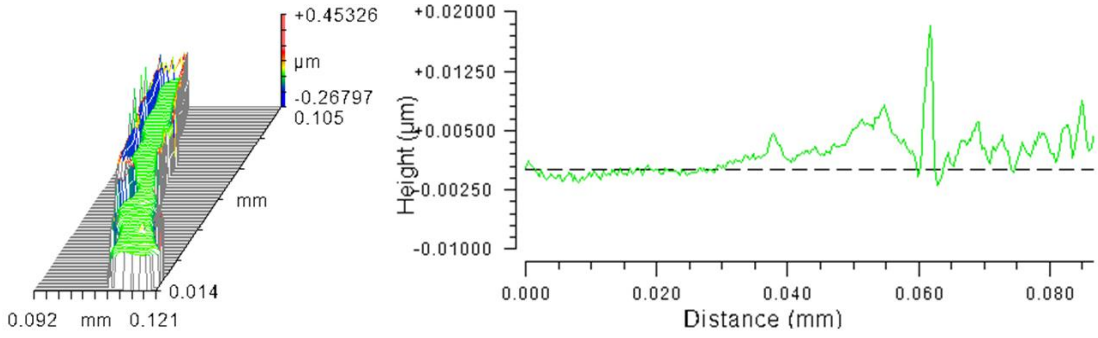

Figure 4.38: Resulting shape of surface C after software processing with a gauss filter with cut-off wavelength of 3.2 µm. The surface roughness is just 10 nm rms.

The improvement of surface roughness provided by arc cleaning, is further highlighted by examining an SEM image of an as-machined cantilever [Figure 4.39]. This shows that the originally cleaved outer surface of the cantilever is very similar to the one shown in Figure 4.32 of the laser cut surface, only the particle size is slightly larger and of a slightly different structure.

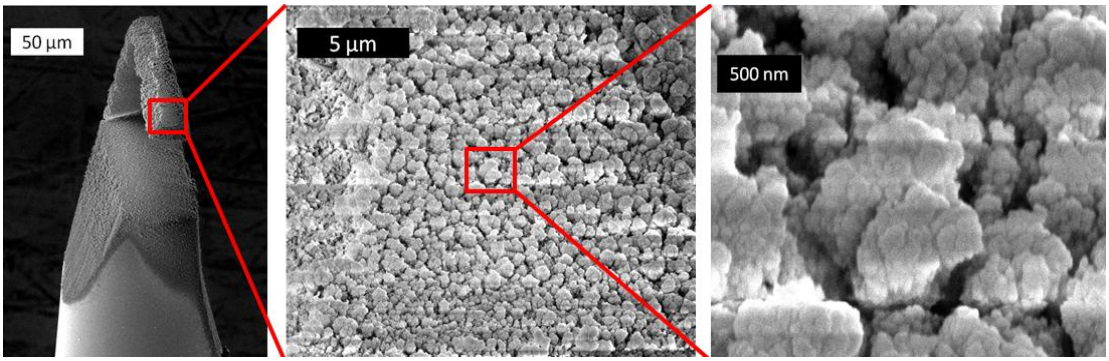

Figure 4.39: SEM Micrograph of an as-machined fibre cantilever; the higher magnifications of the top surface of the cantilever show the rough surface structure.

4.3.5 Application example

It is important to investigate applications of such a cantilever sensor. However there are many possible applications and a detailed description of the interrogation system for dynamic measurements is more complicated than is suitable for this thesis. Work on applications of a fibre optical readout cantilever is covered by a fellow PhD student, Jun Li, who also helped with some of the experiments shown here. However the cantilevers for his research work were machined by me, and I was co-author in some of his publications.

To demonstrate that the proposed process is capable of machining fused silica fibres to a quality sufficient for optical sensing a cantilever sensor was manufactured with a thickness of 10 µm and a length of roughly 100 µm. This cantilever was tested as a simple displacement sensor. An actuator was used to push the end of the cantilever by a known distance and thereby displace it slightly, see Figure 4.40. The response was observed using an optical microscope as well as a commercial interferometric displacement sensor (Renishaw ML10) capable of a measurement accuracy of 1 nm. The cantilever deflection was obtained by determining the optical cavity length via analysis of the spectrum of the reflected light [16].

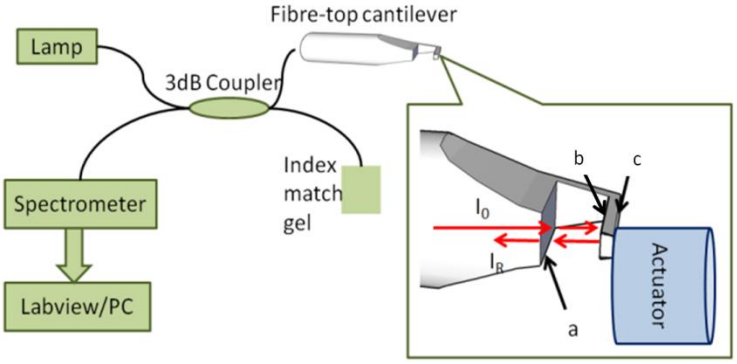

Figure 4.40: Fibre interrogation system.

The optical interrogation system consists of a low-cost broadband light source (tungsten halogen lamp) and a grating based CCD spectrometer (Ocean Optic S2000). A 3dB 2x2 fibre coupler for 633 nm with a bandwidth of ± 15 nm centred around 633 nm was used to direct light reflected to and from the sensor cavity to the spectrometer. The light was partially reflected by the first surface of the cantilever which is the fibre-to-air interface (surface (a) in Figure 4.40 inset). A second reflection occurred from the air-to-cantilever interface and a third reflection from the cantilever-to-air interface (surface (c) in Figure 4.40 inset). The intensity of the light reflected by the air-to-cantilever interface (surface (b) in Figure 4.40 inset) is very low due to surface roughness and to a first approximation this reflection does not contribute significantly to the optical signal and therefore can be ignored. The main sensing interference is generated by the two remaining reflections from surface (a) and (c). If monochromatic light had been used one could see changes in the intensity of the recorded signal when the cantilever is actuated however an absolute measurement of the cavity length would not be possible. In our case a broadband source is used that emits over a range of wavelengths. For example a 5 µm cavity is sufficient to fit 20 periods of 500 nm light (10 periods before the reflection and 10 after) but only 19.5 periods of a 513 nm wave. Therefore the interference between the light being coupled back into the fibre core and the reflection from surface (a) is constructive for 500 nm and destructive for 513 nm. Hence the spacing of the peaks of the recorded spectrum contains is dependent on the cavity length see Figure 4.41 for an example spectrum. By using an FFT algorithm [16] the spectrum can be

analyzed and a very accurate measurement of the absolute cavity length can be acquired.

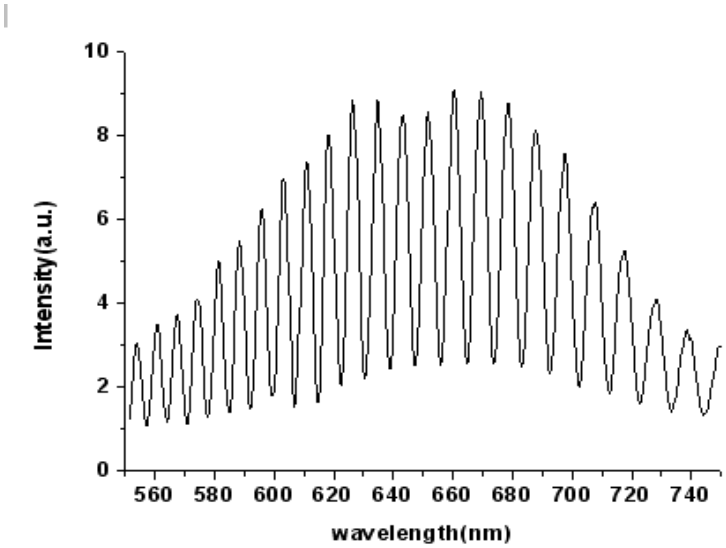

Figure 4.41: A typical spectrum recorded from a cantilever when illuminated by a tungsten light bulb through a 2x2 fibre optic coupler designed for 633nm.

Cantilever displacement results in a change in the length of the optical cavity, and hence a corresponding change in the spectrum of the reflected light. The noise level was determined by mounting the cantilever in a temperature stabilised environment (±1°C), and using the optical interrogation system to measure the cavity length over a period of 5 minutes (measurement made every second). This showed a maximum deviation equivalent to 50 nm. For actuation testing the cantilever is mounted onto a micro block, with actuation applied via a second fibre controlled by a calibrated piezoelectric translation stage. A plot of the data recorded using the fibre interrogation system and using the ML10 is shown in Figure 4.42(a). The residuals of a linear fit to the measurements are plotted in Figure 4.42(b), showing a maximum deviation of ±15 nm. The residuals do not appear entirely random but are instead overlaid by some sort of function, which could be a result of the actuation happening at a slight angle, or a slight misalignment.

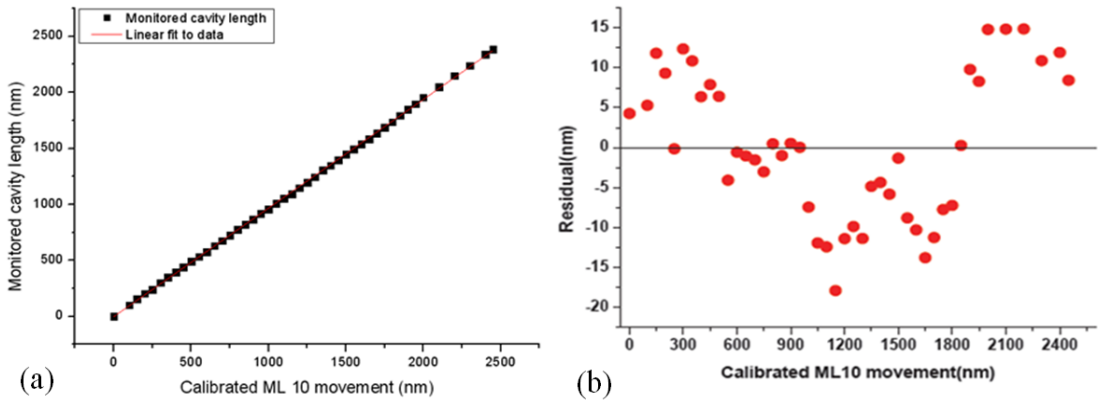

Figure 4.42: Cavity length measured with fibre optic interrogation method versus the measurement taken with a commercial displacement sensor and the residuals of a linear fit to the measurement data.

4.3.6 Alternative designs and further possibilities

Due to the limit in fibre diameter the fibre top cantilever design is restricted to lengths shorter than roughly 115 µm allowing 10 µm for a hinge. Given a typical thickness of 10 µm (e.g. cantilever shown in Figure 4.39) the cantilevers are not highly sensitive, and vibration measurements are not possible at sensible accelerations. There are three ways to improve sensitivity of the cantilever sensors: (i) reduction in thickness; (ii) increased length and (iii) increased mass at the end of the cantilever to introduce a larger force on the cantilever whilst maintaining thickness. Producing a thinner cantilever was not possible with laser machining, however it is possible to machine the rough shape with the laser and use a FIB milling process to reduce the thickness further. This approach was developed separately by Jun Li [17]. Two other approaches were tested although the process was not fully developed.

A fibre top cantilever with a larger mass was the first attempt because the main geometries and the laser processing steps are identical to the fibre top cantilever. There are several possible ways of altering the cantilever design in order to increase the mass. The quickest way to change the process was to keep more of the intial 'ridge' shape; instead of cutting all the way to the outside a rectangular shape from the centre of the ridge was removed (see Figure 4.43). By making a small cut on the

thicker side of the ridge one can establish a cantilever with a larger mass attached to one end, as shown in Figure 4.43. Unfortunately with this approach a sacrificial structure is not possible, however the amount of debris is considerably less than in the normal top cantilever approach as the distance between the machining and the cantilever is much larger.

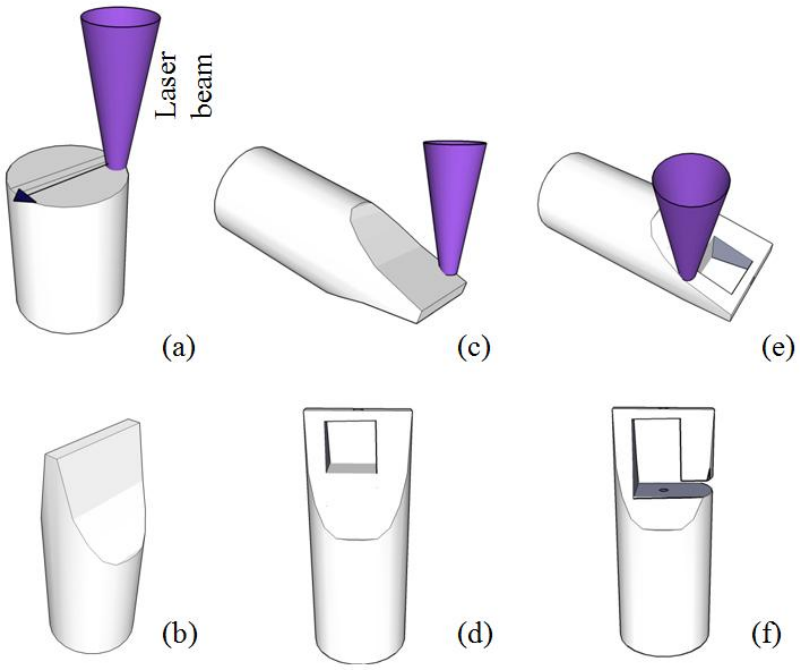

Figure 4.43: Schematic of the laser machining process to establish a cantilever with a larger mass which could be beneficial for acceleration measurements.

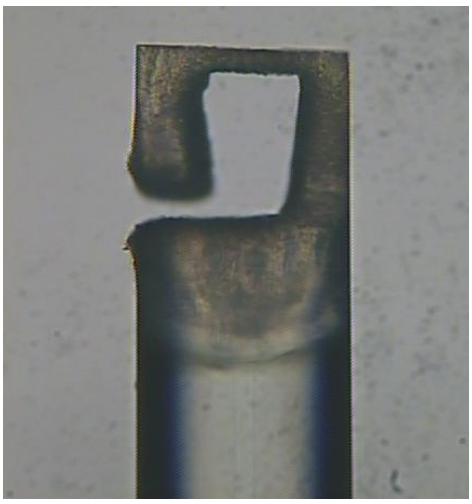

Figure 4.44: Laser machined fibre top cantilever with increased mass at the open end of the cantilever.

A cantilever that was machined with this approach is shown in Figure 4.44. This is one example of the possible shapes that can be machined. The biggest advantage of the ridge approach is that the thin layer of glass can be machined with a high accuracy and almost arbitrary shapes can be cut out of the ridge allowing many different shapes of increased mass at the end of the cantilever.

A further example of the machining possibilities is shown in Figure 4.45. This was used to showcase the possibilities rather than as a demonstration of a fully developed process, hence it was not tested as a sensor. First a disc is cut out of the fibre by mounting the fibre on the side leaving only a thin part of the fibre attached to the disc (Figure 4.45 (a)). This cut is performed twice to correct for the taper angle. This disc (Figure 4.45 (b)) is subsequently cut(Figure 4.45 (c)) to establish a large mass at the end of the cantilever while maintaining a thin cantilever with a low width (Figure 4.45 (d)).

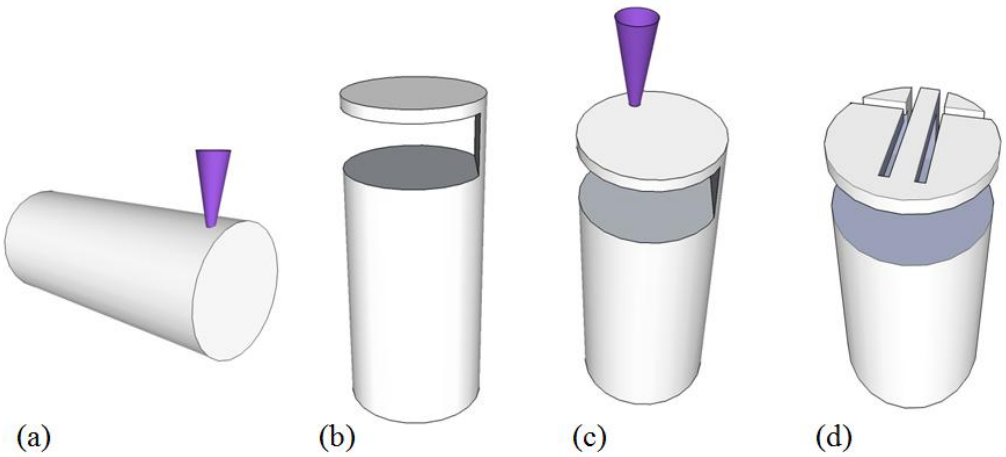

Figure 4.45: Fibre top cantilever laser machined with an increased mass. (a) cutting a (b) disc shape cantilever; (c) patterning the disc to establish a thin cantilever (d) with low width for increased sensitivity and a high mass at the end.

Such a device was successfully machined out of the fibre [Figure 4.46] although it did not perform as a sensor due to a number of reasons, including surface roughness and mechanical strength. By improving the process it is likely that it is possible to build a fibre top cantilever this way.

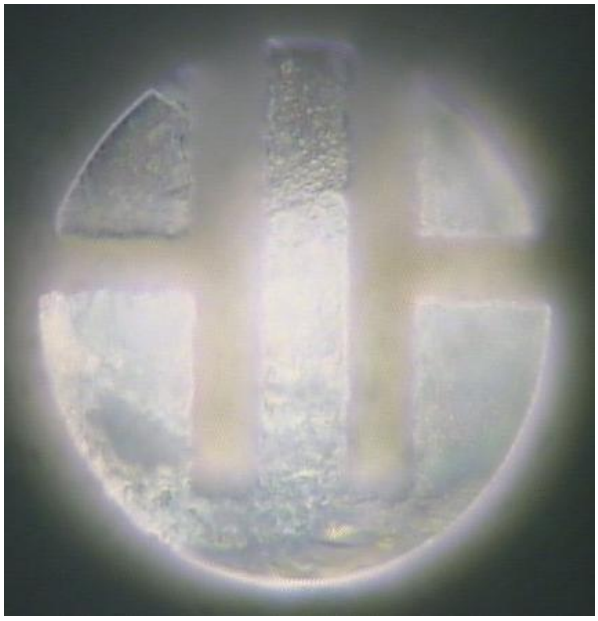

Figure 4.46: Top view of a disk shaped fibre top cantilever. Initially a disk was machined out of the fibre, and then patterned from the top. The central cantilever is still attached to the fibre while the other cuts ensure that the mass can move freely. The cantilever has a thickness of 20 µm.

The fibre top approach has shortcomings with regards to its flexibility. The length of the cantilever cannot be increased therefore a different geometry was investigated. In this manufacturing approach the fibre cantilever is not placed at the top end of the fibre but at the side of the fibre. The working principle was already discussed in Section 4.1.1. The light is reflected by a 45° surface in the area of the fibre core towards the cantilever that is placed along the fibre. Here we show promising results that it is possible to machine such a device however the development of a working sensor was beyond the scope of this thesis. A working sensor of this geometry was however machined in the FIB milling approach by Jun Li [18]. An example of a laser machined side cantilever is shown in Figure 4.47 and Figure 4.48.

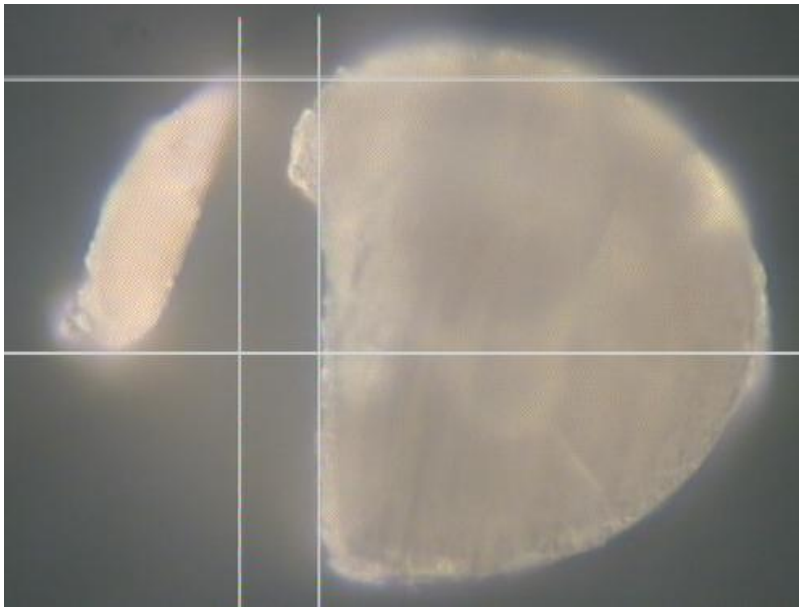

Figure 4.47: View of the end face of a laser machined fibre side cantilever. The gap shows the taper that is typical for laser machining. The gap is between 16 µm and 32 µm wide. The cantilever bends slightly away from fibre.

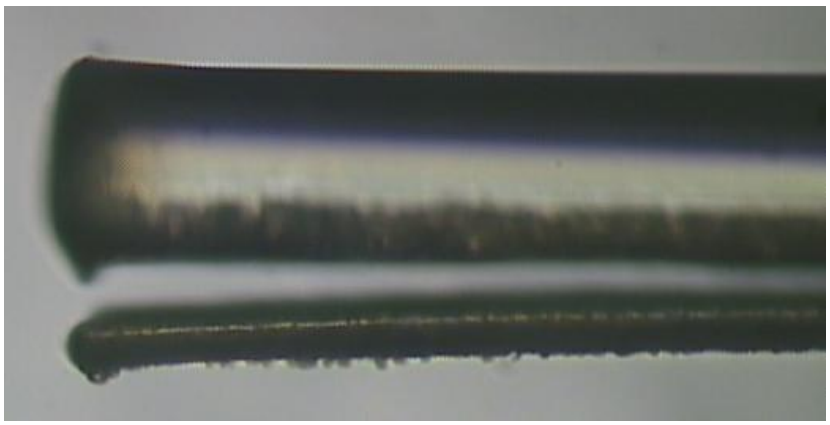

Figure 4.48: Side view of the laser machined cantilever showing that the the cantilever bends away from the main part of the fibre. Cantilevers of up to 1 mm long were successfully machined.

In this section the possibilities and the flexibility of the picosecond laser micromachining of fused silica optical fibres were demonstrated. The examples shown of alternative designs of fibre cantilevers overcome some of the dimensional limitation of a simple fibre-end cantilever. The increased mass cantilevers can be used for example in vibrations sensing, whilst the side cantilevers can be used to create much longer cantilevers, and hence significantly increased sensitivity [18].

1. E. Udd, "An overview of fiber optic sensors," Review of Scientific Instruments **66**, 4015-4030 (1995).
2. A. Perot, and C. Fabry, "On the application of interference phenomena to the solution of various problems of spectroscopy and metrology," The Astrophysical Journal **9**, 87 (1899).
3. T. Yoshino, K. Kurosawa, K. Itoh, and T. Ose, "Fiber-optic Fabry-Perot interferometer and its sensor applications," Quantum Electronics, IEEE Journal of **18**, 1624-1633 (1982).
4. D. Iannuzzi, S. Deladi, J. W. Berenschot, S. de Man, K. Heeck, and M. C. Elwenspoek, "Fiber-top atomic force microscope," Review of Scientific Instruments **77** (2006).
5. D. Iannuzzi, S. Deladi, V. J. Gadgil, R. G. P. Sanders, H. Schreuders, and M. C. Elwenspoek, "Monolithic fiber-top sensor for critical environments and standard applications," Applied Physics Letters **88** (2006).
6. D. Iannuzzi, S. de Man, C. J. Alberts, J. W. Berenschot, M. C. Elwenspoek, A. A. Said, and M. Dugan, "Fiber-top micromachined devices - art. no. 700403," P Soc Photo-Opt Ins **7004**, 403-403 (2008).
7. S. Deladi, D. Iannuzzi, V. J. Gadgil, H. Schreuders, and M. C. Elwenspoek, "Carving fiber-top optomechanical transducers from an optical fiber," Journal of Micromechanics and Microengineering **16**, 886 (2006).
8. D. Iannuzzi, K. Heeck, M. Slaman, S. de Man, J. H. Rector, H. Schreuders, J. W. Berenschot, V. J. Gadgil, R. G. P. Sanders, M. C. Elwenspoek, and S. Deladi, "Fibre-top cantilevers: design, fabrication and applications," Meas Sci Technol **18**, 3247-3252 (2007).
9. D. Iannuzzi, S. Deladi, M. Slaman, J. H. Rector, H. Schreuders, and M. C. Elwenspoek, "A fiber-top cantilever for hydrogen detection," Sensor Actuat B-Chem **121**, 706-708 (2007).
10. Y.-J. Rao, and D. A. Jackson, "Recent progress in fibre optic low-coherence interferometry," Measurement Science and Technology **7**, 981 (1996).
11. E. Udd, K. Corona, K. T. Slattery, and D. J. Dorr, "Tension and compression measurements in composite utility poles using fiber optic grating sensors," Pacific Northwest Fiber Optic Sensor Workshop, Proceedings **2574**, 14-19 (1995).
12. M. Ghoreishi, D. K. Y. Low, and L. Li, "Comparative statistical analysis of hole taper and circularity in laser percussion drilling," International Journal of Machine Tools and Manufacture **42**, 985-995 (2002).
13. R. D. Schaeffer, "Understanding and controlling taper when laser machining," in *Micro Manufacturing*(Don Nelson, 2010), pp. 13-14.
14. E. Mendez, K. M. Nowak, H. J. Baker, F. J. Villarreal, and D. R. Hall, "Localized CO2 laser damage repair of fused silica optics," Appl Optics **45**, 5358-5367 (2006).
15. K. Tada, G. Cohoon, K. Kieu, M. Mansuripur, and R. A. Norwood, "Fabrication of high-Q microresonators using femtosecond laser micromachining," in *Lasers and Electro-Optics (CLEO), 2012 Conference on*(2012), pp. 1-2.

16. J. Yi, "Fourier Transform White-Light Interferometry for the Measurement of Fiber-Optic Extrinsic Fabry-Perot Interferometric Sensors," Photonics Technology Letters, IEEE **20**, 75-77 (2008).
17. J. Li et al. "Fabricating optical fibre-top cantilevers for temperature sensing" in Meas. Sci. Technol. **25** 035206 (2014)
18. J. Sun et al. "Fabrication of a side aligned optical fibre interferometer by focused ion beam machining" in J. Micromech. Microeng. **23** 105005 (2013)

Chapter 5: Manufacture of high precision encoder scales using a nanosecond laser process

In this chapter some example applications of high precision nanosecond laser processing are presented, which demonstrate that ultrashort pulsed lasers are not always the route to the highest precision; in some cases longer pulses are better. Nanosecond lasers are very common tools for many manufacturers, due to their relatively low cost and high reliability. This is because achieving a high average power together with pulse lengths of nanosecond is a 'simple' process compared to achieving a high average power with pico- or femtosecond lasers. Nanosecond pulse length can be achieved by q-switching, without the need for more complicated pulse picking electronics and pulse stretching and compression techniques, providing suitable high average powers and pulse energies for micromachining without subsequent amplification. Typical q-switched nanosecond lasers have pulse lengths in the order of 10-50 ns. In the example that is discussed here the aim is to manufacture encoder scales for optical position encoders. Because the encoder head relies on optical reflection from the encoder scale, smooth and highly reflective surfaces are essential for good and reliable operation of the encoder. A schematic drawing of the encoder is shown in Figure 5.1, with the profile of the required encoder scale shown in Figure 5.2.

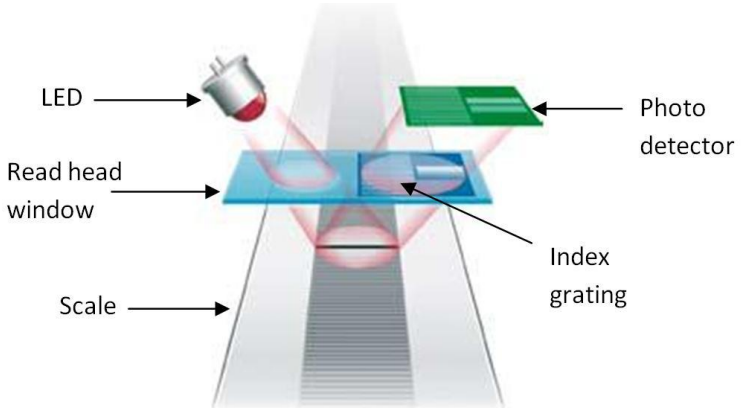

Figure 5.1: Schematic drawing of the working principle of an optical position encoder. All parts except the scales are integrated into the read head. Usually the read head is mounted on the moving part while the scale is fixed.

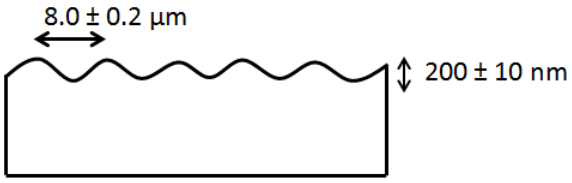

Figure 5.2: Profile of a sinusoidal encoder scale with a pitch of 8 µm and a depth of 200 nm

Encoder scales are high precision products which are used in many sectors including manufacturing and life science. Process control and therefore position control is closely related to reliability and company credibility. These factors can provide a direct competitive advantage. High precision position encoder scales are based on a repeatable distance between lines although slight fluctuations of up to 100 nm would be tolerable due to interpolation over several lines. The precision of an optical position encoder is related to the pitch of the grating, and the interpolation electronics. The proposed design involves an LED emitting at 800 nm. The interference on which the encoder relies therefore requires a 200 nm optical path length difference, i.e. the peak to trough height of the encoder scale [Figure 5.2]. The challenge to laser manufacturing was to achieve this within a tolerance of ±10 nm. The periodicity was chosen to be 8 µm for a demonstrator product. By decreasing the pitch further the resolution of the read head can be increased; a read head that is already commercially available using a pitch of 20 µm can achieve resolutions down

to 5 nm with interpolation techniques. Current manufacturing methods for such gratings typically use lithographic techniques as mentioned in section 2.2.5 to manufacture metal-on-glass scales however these processes are not suitable for the meter scale gratings required for long scale manufacturing applications. Prior to this project scales manufactured with embossing techniques that are very quick however accurate peak-to-trough height control is an issue.

The laser used for the work presented in this chapter is a diode pumped Nd:YAG laser with a pulse length of 33 ns, pulse energies of up to 1 mJ and an average power of up to 10 W, manufactured by JDSU. The fundamental wavelength of the gain medium is converted from 1064 nm to 343 nm and the frequency conversion is achieved in the same housing, so the laser emits only at 343 nm. This laser was used specifically for a metal modification application because the reflectivity of stainless steel is less in the UV than for the common 1064 and 532 nm wavelengths, hence the heating influence of the laser pulses can be better controlled. When other wavelengths are used a higher energy is required to raise the temperature of the metal to melting at which the absorption suddenly increases and a sudden onset of ablation happens showing a very non-linear behaviour. The absorption into the IR range of the light of stainless steel 304, which is a very common steel, is shown in Figure 5.3.

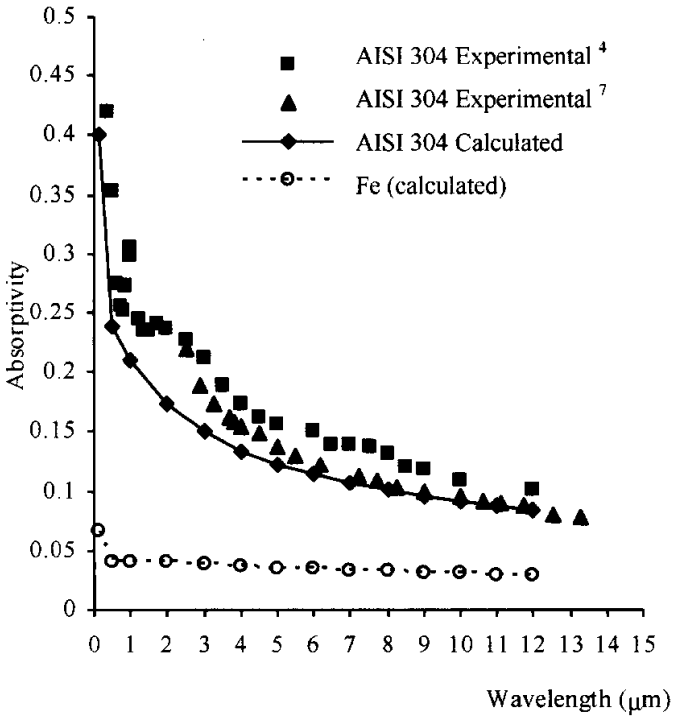

Figure 5.3: Absorptivity of stainless steel AISI 304 as a function of the wavelength at room temperature [1].

With this increased control it is possible to achieve 'gentle' heating rather than immediate melt pool expulsion and ablation, and the associated rough surfaces.

5.1 The YAGBoss melt-reflow process

The name of this technique is derived from the laser source, a Nd:YAG laser and the term 'embossing'. The process was developed in collaboration with Renishaw plc. to quickly manufacture high precision encoder scales using nanosecond laser pulses on stainless steel samples. The process on stainless steel itself is not part of the work presented in this thesis (it was developed by other members of the research group [2]) but it is essential to understand the basic principles of this as background to the work that I carried out on alternative techniques reported in this thesis. The YAGboss process relies on controlled melting and subsequent melt flow driven by thermally-induced surface tension gradient. A number of phenomena are involved in the process including: [3-7]

- Local absorption of the laser light and generation of heat;
- Local heating and propagation of the heat;
- Melting temperature is reached at the point of incidence;
- The melt front propagates along the surface;
- Development of a surface tension gradient across the meltpool introducing localised melt flow [8, 9];
- Eventually reaching of vaporisation temperature at the point of incidence
- Recoil pressure from the expanding material enhancing the surface tension effects.

In case of ablation and recoil pressure occurring usually the depth of machining is much deeper than desired and therefore this effect should be avoided for our application, however for larger scale manufacturing of shapes it can be useful to exploit this effect (e.g. SurfiSculpt) [10, 11].

A schematic drawing of the process showing some of the effects that are used to shape the material by laser melting and reflow of the material is shown in Figure 5.4.

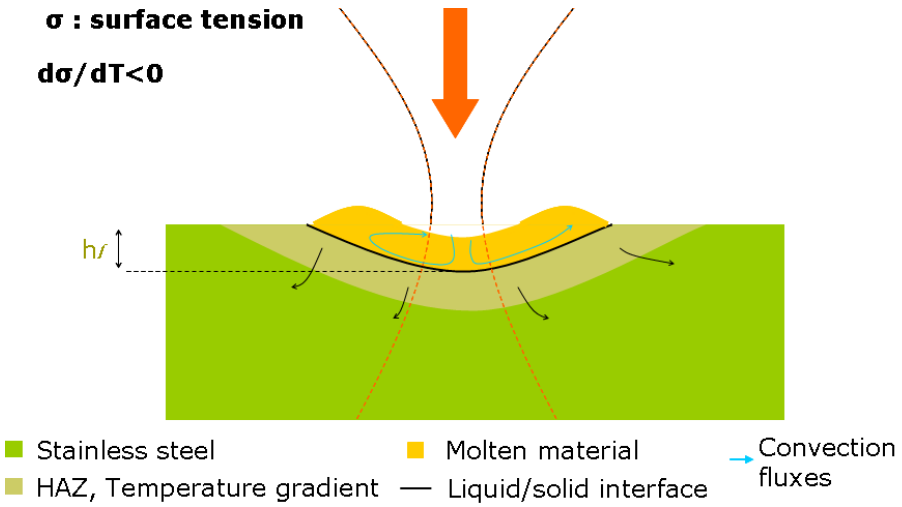

Figure 5.4: Hydrodynamic surface distortion through laser melting of a surface layer. [8]

By using a cylindrical lens the laser intensity is concentrated along a line, hence linear shapes can be generated. The target surface profile is ideally either a

sinusoidal or square profile of 8 µm periodicity in one dimension, uniform over at least one mm in the other dimension. Each line is written with either a single pulse or a few pulses, after creating the first line the sample is moved by 8 µm and the next line is written. Repeating this process provides the required a sinusoidal. This processing example is one potential application of a melt and reflow process. Further understanding of the process was gained through studies of the ambient temperature and single versus multiple pulses as well as different compositions of steel. Information on this work can be found in [12].

As mentioned earlier this melt and reflow process on stainless steel samples was carried out by others. My work was to investigate alternative materials for the generation of similar periodic structures of 8 µm periodicity.

5.2 Experimental arrangement for nanosecond processing for scale manufacture

A schematic diagram of the set-up for the experiments described in the following sections is shown in Figure 5.5. The source is a nanosecond JDSU Nd:YAG q-switched laser, frequency tripled to provide a laser emission wavelength of 355 nm. The exit beam has a circular shape, a diameter of 1.6 mm and $M^2 < 1.2$. The maximum average power of the laser is 10 W at a repetition rate of 10 kHz, corresponding to a pulse energy of 1 mJ. The average power was controlled by an attenuator consisting of a half wave plate and a polarizing beam splitter. Therefore the polarization is known and the laser runs at a stable power being less dependent on fluctuations of the pump current. The pump current is the primary means of adjusting the laser output power. Once the laser has warmed up a working power is selected and further changes in average power are obtained using an external attenuator to minimize power fluctuations. The beam is expanded and collimated by a set of spherical lenses, providing an expansion factor of 2.5. The expanded beam is directed through a cylindrical lens of focal length 50 mm to generate a line 8 µm by 4 mm. The lens is mounted on a z-axis linear stage to allow the focus to be optimised on the sample surface. The sample is positioned by a linear translation stage with an air bearing and high precision linear encoders for accurate triggering

which is crucial in order to achieve precisely the 8.00 ±0.01 µm pitch. The difficulty with this setup is that it requires a very high precision in terms of sample z-position. Further more the angular alignment of the sample relative to the long axis of the cylindrical lens is crucial because even a minor change in the angle results in lines that are slightly closer to each other than set on the stage. During the period that the work presented here was undertaken the positioning and triggering had not been optimized and the laser started to fail causing reliability issues. The main problem was that the stage is not stationary for the fast processing, and the smallest delay in triggering caused a measureable pitch change. In the later stages of the project the positioning and triggering of laser pulses was improved, however the studies presented here did not make use of these improvements and are rather a proof of concept than a complete working process. However they demonstrate that surface structuring to the required precision can be achieved.

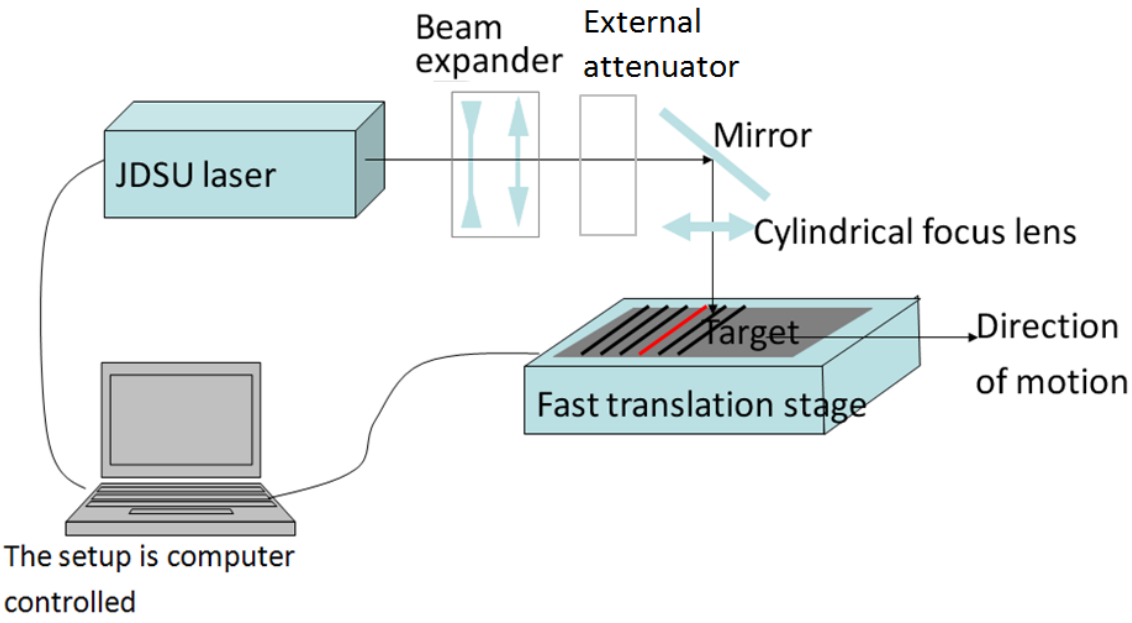

Figure 5.5: Schematic drawing of the setup used for nanosecond laser machining of optical encoder scales

5.3 Processing of nickel coated samples

With the knowledge that the YAGboss process can generate the desired features on stainless steel, it is very likely that the same process with different parameters also works with other metals. The advantage of stainless steel is that its availability is very good, and also it is possible to polish it to a high quality mirror like finish. The thermal properties of stainless steel strongly vary depending on the type of steel. One of the very important components in stainless steel is the metal nickel. Nickel has a high reflectivity over a broad range of wavelengths as can easily be seen when looking at a nickel coated sample. Nickel also has a melting point which is very similar to that of stainless steel. Furthermore it can be applied as a coating that attaches well to other materials such as copper.

Stainless steel like most materials have a positive coefficient of thermal expansion (CTE), which can introduce errors to a positioning system. These errors can be accounted for but a material that has a CTE of close to zero would be clearly advantageous for high precision equipment. Carbon-fibre-reinforced plastics

(CFRP) are known to offer the possibility of a tailored CTE. However machining CFRP is very difficult, and also the reflectivity of CFRP is very low. Therefore the ideal material would be a reflective CFRP sample, which can be achieved by depositing a reflective coating. However adhesion to CFRP is not simple and not every coating adheres well. The solution was to use samples with more than one coating layer. The first samples consisted of three different materials and a cross section through one of the samples is shown in Figure 5.6.

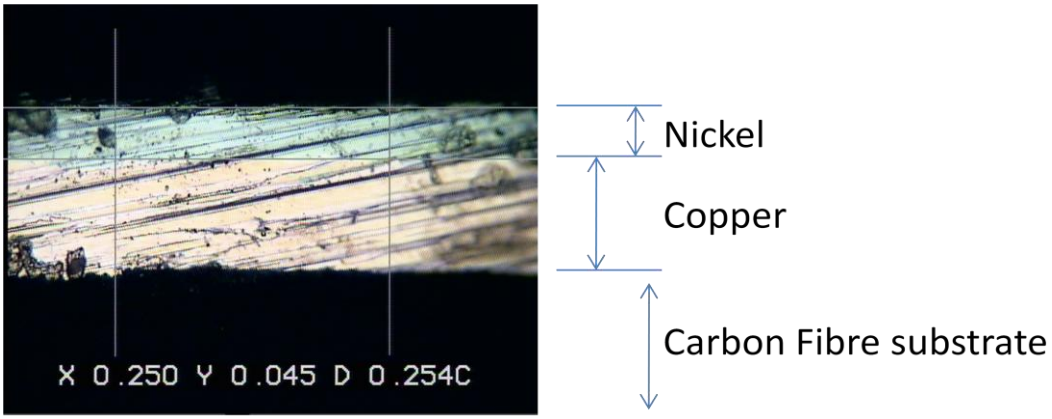

Figure 5.6: Micrograph of a section through the nickel on carbon fibre sample. A nickel layer of ~45 µm and a copper layer of ~100 µm are coated on top of the black carbon fibre structure which is barely visible due to the high absorption.

A layer of copper of roughly 100 µm thickness acts as an adhesion agent between the nickel and the CFRP, because the nickel on its own does not adhere well to the CFRP. The nickel coating in this specific sample is roughly 45 µm thick. The samples had imperfections and areas with low or no adhesion forming bubbles underneath the metal coating indicating the difficulty in manufacturing a suitable material. This process was being developed in parallel by a third party so only early samples (all from the same batch) were available. However as a proof of concept and to determine whether further investments in the sample manufacturing process are worthwhile, the YAGboss process was tested on these samples. Details of the CFRP manufacturing process were not made available to Heriot-Watt.

The YAGboss process was tested on these samples and the results obtained are very similar to those on stainless steel. As discussed in section 5.1 a number of

parameters can be modified to tune the process. The depth can be controlled by the number of pulses and the energy per pulse. The best parameters were found to be around 600 µJ per pulse and 10 pulses per line for stainless steel. In total an energy of 6 mJ per line showed ideal results, however it was found that multiple pulses showed better results than fewer pulses at a higher energy however a minimum energy of 500 µJ was required to initiate the process.

For sample analysis, it was found that limited information can be gained from an optical microscope as shown in Figure 5.7.

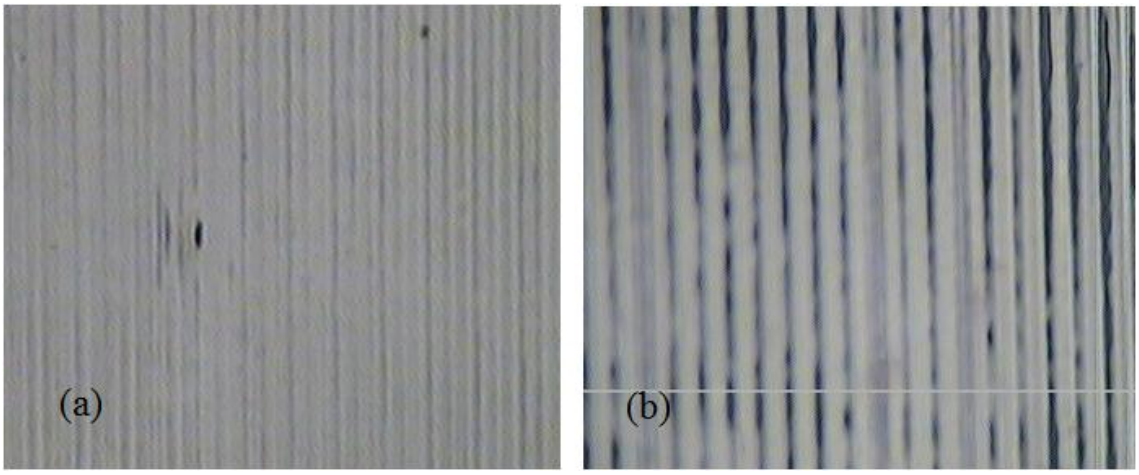

Figure 5.7: Microscope images of machined gratings both with a pitch of 8 um (a) is machined with parameters below the ablation threshold, 5 pulses of 420 µJ, the lines have a peak to valley depth of 250 nm, (b) is machined with the same pulse energy but with 7 pulses, ablation occurred in this case and black lines show on the sample, the peak to valley depth is roughly 700 nm.

The only reliable information from the microscope concerned the periodicity of the machined lines and whether or not ablation has occurred; the pulse energy in Figure 5.7(b) shows an example of ablation, whilst in Figure 5.7 (a) there is no ablation.

The best YAGboss results were generated by using multiple pulses and relatively low pulse energies, with an optimum at 12 successive pulses of 300 µJ energy. A sample that was machined with these parameters is shown in Figure 5.8.

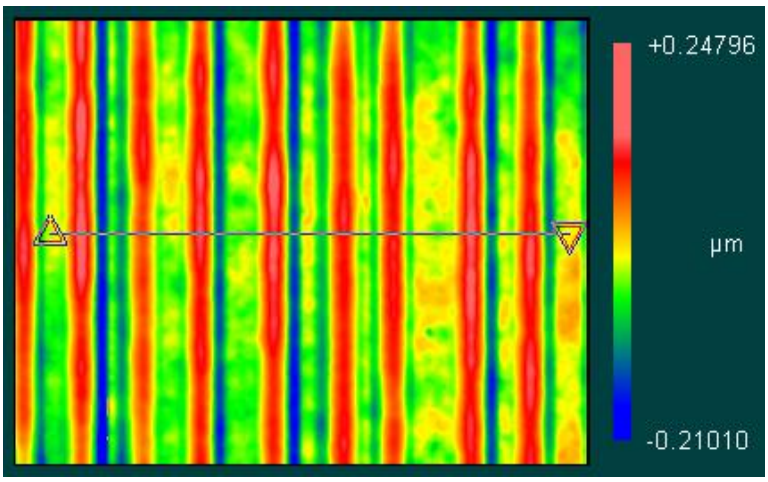

Figure 5.8: Height map of a machined nickel coated sample measured with the whitelight interferometer. Changes in valley width resulted from a drift in the linear stage. The maximum peak to valley is roughly 450 nm, however the average height of the peaks is in the range around 350 nm.

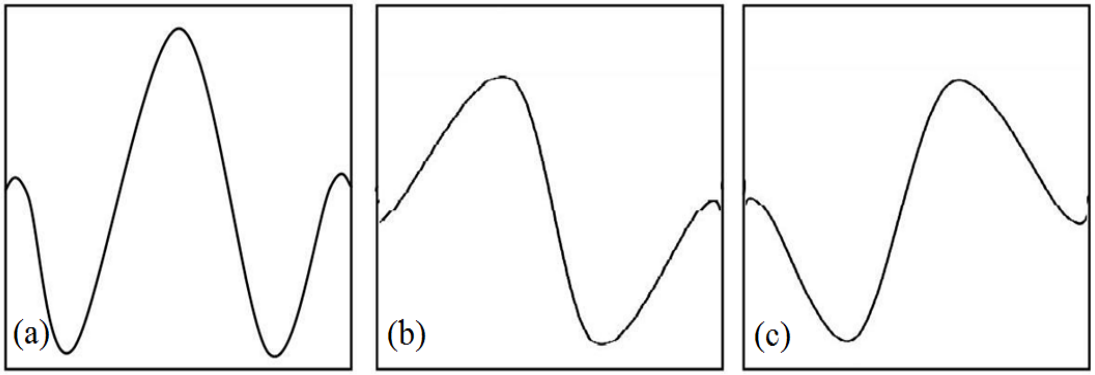

Figure 5.9: Schematic drawings of lines that are achieved with the laser machining process (a) is the desired shape of a line and two depressions next to it; (b) and (c) drift of the stages during successive pulses shifted the position of the line.

A slight drift of the stages between successive pulses which was caused by inprecise triggering can result in different shapes of the machined area.

These proof-of-principle results demonstrated that the process can be used to shape the surface of the nickel coated samples into a sinusoidal pattern. However the laser broke down during these studies and further experiments were postponed and finally stopped due to the success that was achieved with the stainless steel samples.

However, the material used here could still be a useful alternative to stainless steel due to its low CTE.

5.4 Processing of polyimide coated steel

An alternative approach investigated was to machine a polyimide layer deposited onto a stainless steel sample, as shown in Figure 5.10. In this case the process would provide a binary scale rather than a sinusoidal scale. However both types are suitable for encoder applications.

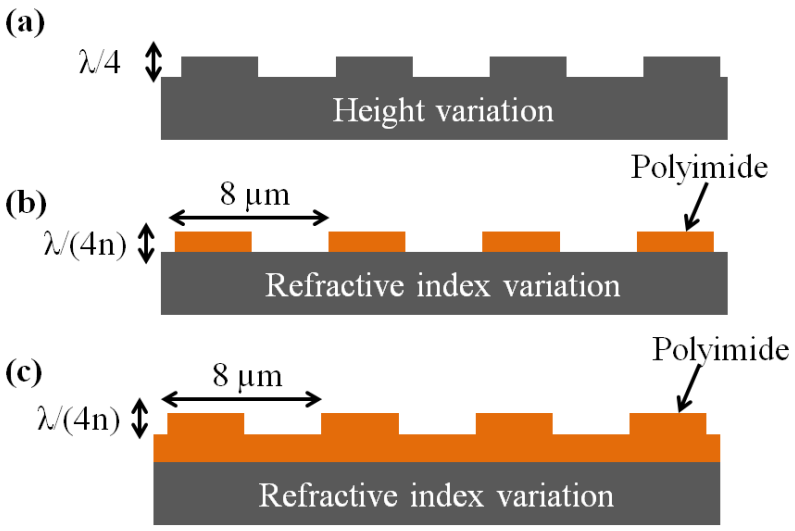

Figure 5.10: Idealized grating types (a) purely reflective grating path difference is twice the height difference (b) binary grating machined with the stainless steel aiding as a stopping layer; (c) binary grating machined out of a thick layer of polyimide;. In (b) and (c) the optical path difference is the height divided by the refractive index of the polyimide.

The step height requirement depends on the wavelength of the encoder read head, which requires is $\frac{\lambda}{2}$ on reflection as described at the beginning of this chapter. This means that the step height for a purely reflective grating (Figure 5.10(a)) is $\frac{\lambda}{4}$. For the overcoated samples (Figure 5.10(b) and (c)) the optical path length is influenced by the refractive index n of the coating. However the refractive index depends on the thickness of the coating, and in particular very thin coatings have a refractive index that differs strongly from the bulk refractive index.

Because the removal of layers as thin as 200 nm from a thick sample is not straightforward with a laser process and most ablation processes result in a rough surface with surface roughness rms > 300 nm it was decided that the best way to produce a binary grating with the desired feature sizes is to use a thin film of the required thickness and use the stainless steel surface as a backstop to the removal process i.e. the approach used in Figure 5.10(b). However this results in challenges of how to apply a thin coating to the necessary precision. A standard technique used to apply thin coatings is spin coating, a simple process that is well understood. A relevant material with well known parameters that can be spin coated and diluted to achieve a lower viscosity in order to achieve thinner coatings is a liquid polyimide VTEC PI-1388. Importantly for this application is also has a very low absorption at a wavelength of 800 nm and hence is suitable for the encoder read-head, whilst being strongly absorbing at the laser machining wavelength of 355 nm. Its optical transmission is shown in Figure 5.11 along two other photoresists that were considered.

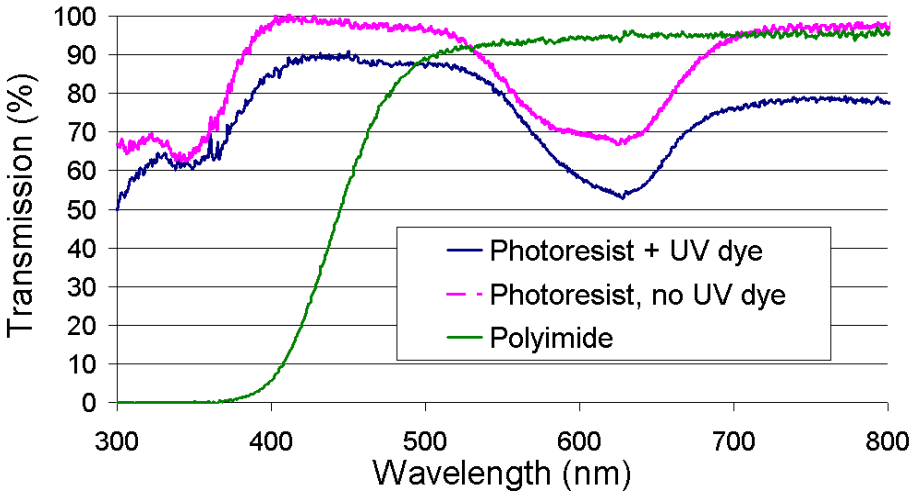

Figure 5.11: Tranmission spectrum of 3 different coating materials suitable for spin coating.

The bulk refractive index of this polyimide when cured is 1.78. This would result in a coating thickness of 266 nm to achieve a path difference of 400 nm after the

reflection. However at these coating thicknesses the refractive index is modified compared with a bulk sample occurs. In order to measure the refractive index for thin coatings several samples were coated with different thicknesses by using different spin coating parameters and different percentages of solvent added to the liquid polyimide. The solvent used is 1-methyl-2-pyrrolidinone. The spin coating process that was used consists of three stages. The initial stage with a low rotational acceleration and low final rotation speed aids an even spread over the whole sample, however it is not fast enough to spray the coating from the sample edges. The second stage with a mid range rotational speed establishes an initial uniform layer, and removes any excessive coating material. The third and final stage is the most important for achieving a thin coating. At this high speed stage the amount of material that is removed from the sample is related to the time at the top speed. The first two stages in our experiment were maintained: The first stage reached a top speed of 200 rpm with an acceleration of 20 rpm s^{-1} for 30 s; the second stage had a top speed of 500 rpm at an acceleration of 50 rpm s^{-1} for 30 s.

A range of different parameters was tested for the final stage with speeds from 3000 rpm to 5000 rpm and spinning times from 30 s to 240 s. The ratio of solvent to polyimide was kept constant at 1.2:1. All samples were cured for 30 minutes at 125 °C. The best and most reliable results were achieved with a spinning speed of 3000 rpm and a time of 180 seconds. This resulted in a thickness between 200 nm and 250 nm. The thickness was measured by scratching the surface of the coated sample and measuring the profile of the scratch with the AFM. In some cases delamination occurred close to the edge of the scratch, samples that showed this behaviour were wiped clean and measured again.

To find the refractive index of the thin coatings one needs to know both the optical thickness and physical thickness of the material. The physical thickness is measured with the AFM. To find the optical thickness we used the thin film interference effect, measuring the transmission as a function of wavelength such a measurement is shown in Figure 5.12. Transmission maxima are observed for wavelengths for which $2\,n\,d = m\,\lambda$ and minima for wavelengths for which $2\,n\,d = (m - \frac{1}{2})\lambda$ where

m is an integer. The refractive index n of any material is itself a function of wavelength, however this effect is relatively weak.

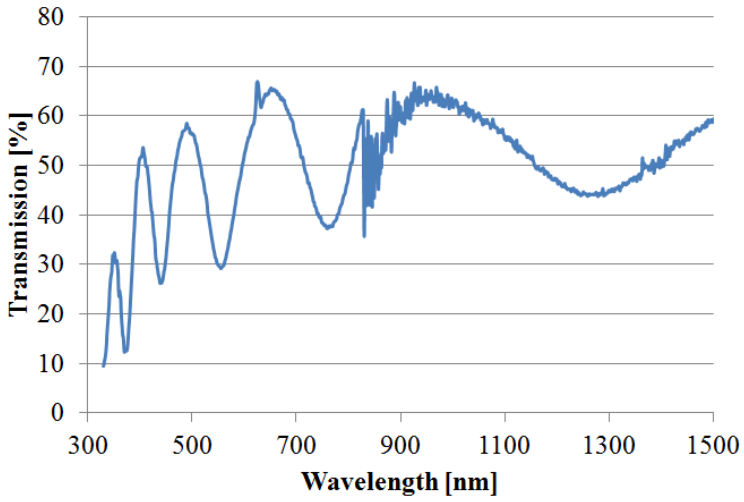

Figure 5.12: Typical reflection spectrum of a coated stainless steel sample. The maxima and minima occur due to thin film interference effects; their relative position allows the optical thickness to be determined and hence also the refractive index. In this case the coating is 515 nm thick and the refractive index measured is 1.9.

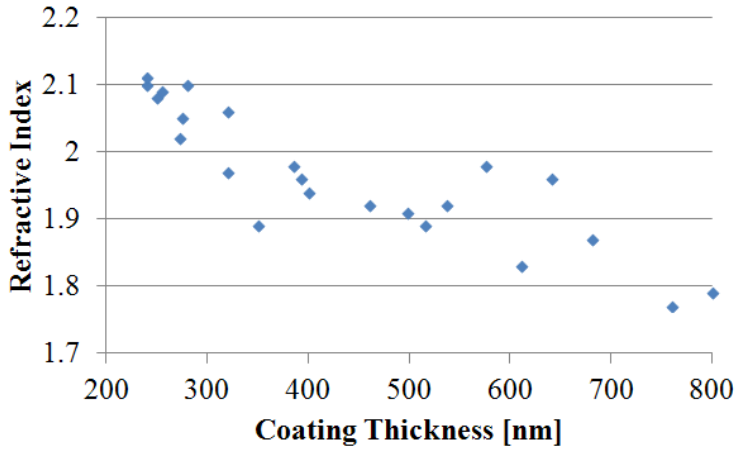

Figure 5.13: Dependence of the refractive index of the deposited coating as a function of the coating thickness.

The refractive index of the coating is somewhat higher than the expected bulk value as shown in Figure 5.13, and the thinner a coating is the higher is its refractive index. This means that the required thickness is only 180 nm. This was achieved by altering

the dilution ratio to 1:1.6. At this ratio the viscosity of the solution was decreased and the desired thickness was achieved with a final spinning procedure of 3000 rpm for 210 seconds.

An estimate of the energy that is required to remove the volume of a single line with a laser pulse can be compared with the energy that was required to form a line in the YAGboss process. Using the volume of a line (1 mm length, 4 µm width and 200 nm depth) of 800 μm^3 and assuming a density of 1.4 g cm^{-2} (values for VTEC PI 1388 were not available, values for DuPont Kapton used for estimate) and a heat of combustion of 26 kJ g^{-1} [13] the required energy is on the order of 30 µJ. This is far less than the 6 mJ that were required to write a single YAGboss line on stainless steel. Another mode of material removal is by delamination, which occurs when the stresses in the film are higher than the strength of adhesion. Since the strength of adhesion of the coated layer is not known we can assume that the energy to heat the material to cause delamination is much lower but the slow heat dissipation in polyimide can limit the effects. A difference between delamination and ablation is that delamination removes an entire layer of the coating film, normally with very well defined edges whilst ablation has an less well-defined edges and often leaves a residue of the coating behind. In our case that is shown in Figure 5.14 some residue is visible and the edges of machining suggest that the removal process is by ablation. The strong absorption of the polyimide coating at the machining wavelength also benefits an ablation process. To evaluate this process and understand the influence of pulse energy and number of pulses a series of experiments was carried out. With the set-up used for the YAGboss process. It was found that the line width varies with pulse energy and number of pulses. For example, with 2 pulses of relatively low energy of 23 µJ with 2 pulses the lines have a width of 2 µm as shown in Figure 5.14(a) whereas with 10 pulses the width is increased to 4 µm. The line width increases with the amount of pulses used for machining however the maximum for this particular energy is reached at about ten pulses. Machining with 2 pulses does not go all the way through the coating, resulting in a rounded bottom; also the troughs are only about 2 µm wide whilst they areabout 4 µm wide with a flat bottom when 10 pulses are used.

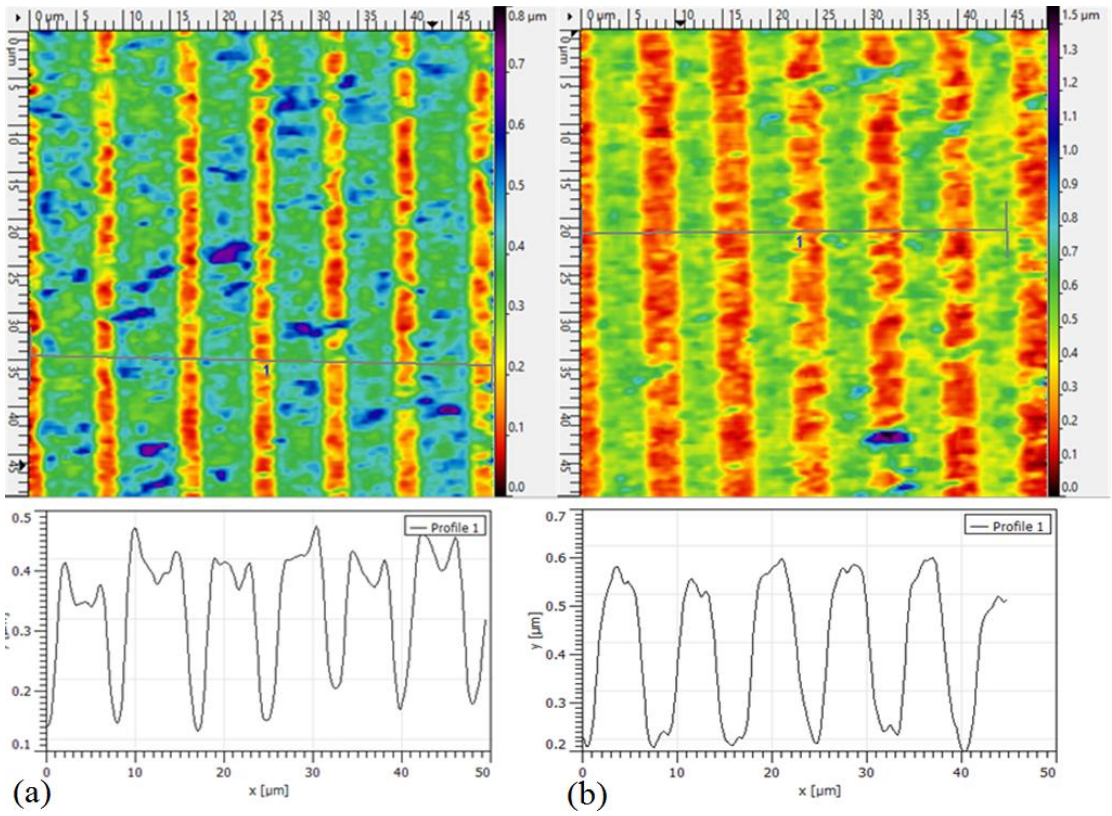

Figure 5.14: AFM scans of a coated stainless steel sample machined with (a) 2 pulses and (b) 10 pulses of 23 µJ. The line graphs at the bottom are each averaged over 20 lines to reduce noise.

A further increase of number of pulses did not significantly increase the width of the trough presumably due to an ablation threshold effect. An increased pulse energy, meanwhile results in wider lines of removed polyimide as shown in Figure 5.15, since a larger proportion of the focussed beam is above the ablation threshold. However the results at lower energies were closer to the desired 8 µm pitch with 4 µm polyimide and 4 µm blank stainless steel.

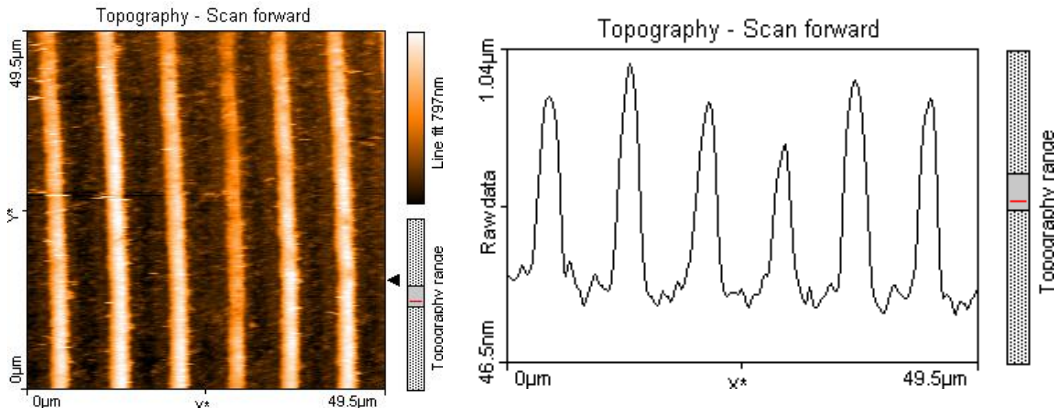

Figure 5.15: Laser machined poyimide coated sample with a pulse energy of 45 µJ and 10 pulses per line. The majority part of the polyimide is removed only thin lines of roughly 2 µm width remained. The coating in this case had a thickness of 800 nm.

When examining the machined samples with an SEM (Figure 5.16) it is obvious that the polyimide removal is not entirely clean and debris is deposited on the sample. However it is not expected that this will cause many problems for the read head as the reflectivity remains high. Another potential issue is that the polyimide layer close to the laser machined area has an increased thickness which might be caused either by a melting process or by an effect that is called bumping in which the thickness of a polymer increases due to some bonds breaking resulting in a decreased density.

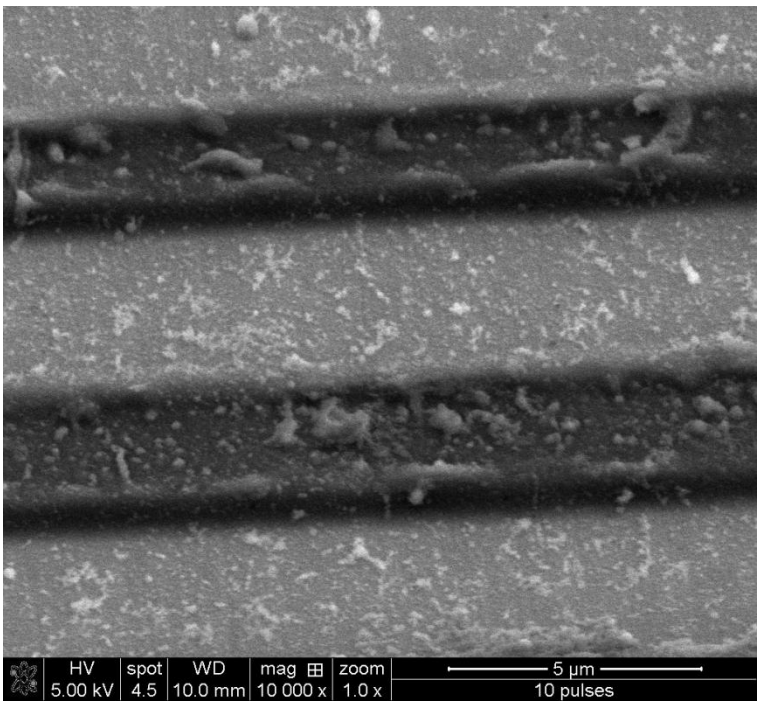

Figure 5.16: SEM scan of a machined sample angled at 45 ° showing the amount of debris that is deposited across the sample and the bumping effect on the edges of the laser machined areas. The machined parts appear brighter in these images because they do not charge up as much as the uncoated polyimide. The sample shown here was machined at a pulse energy of 40 µJ.

5.5 Conclusion

In many high precision manufacturing processes using lasers, ultra short pulses have advantages over nanosecond pulses. However in some cases nanosecond laser pulses are more suitable, this is partially because in cases of metal processing the average heating effects can increase machining speed and therefore the throughput. When considering micro processing with precision of a few tens of nm, the almost generally accepted opinion is that the shorter the laser pulse the higher the precision that can be achieved. As was shown in this chapter this is not always true if an optical surface is required, where ns-induced melting avoids the roughness associated with an ablation process. Marangoni effects can be exploited to generate the high resolution surface feature required for encoder manufacturing. Furthermore the throughput of this melt and reflow process is higher than the current techniques

for these high resolution position encoders. The second process investigated for encoder manufacture was designed to move the process control requirements somewhat away from the laser machining step towards the preparation of the sample, since the machined depth control is provided by the coating thickness.

The two techniques investigated for encoder manufacture are examples of processes where a nanosecond laser is the laser of choice due to the precision and control that can be achieved. In addition nanosecond lasers are currently significantly lower cost than picosecond laser systems of the same average power.

References

1. S. Boyden, and Y. Zhang, "Temperature and wavelength-dependent spectral absorptivities of metallic materials in the infrared," Journal of thermophysics and heat transfer **20**, 9-15 (2006).
2. N. J. Weston, D. P. Hand, S. Giet, and M. Ardron, "Method of forming an optical device," Patent WO2012038707.
3. G. Lallemand, G. Jacrot, E. Cicala, and D. Grevey, "Grooving by Nd: YAG laser treatment," Journal of Materials Processing Technology **99**, 32-37 (2000).
4. J. Qi, K. Wang, and Y. Zhu, "A study on the laser marking process of stainless steel," Journal of Materials Processing Technology **139**, 273-276 (2003).
5. N. Pierron, P. Sallamand, and S. Matteï, "Numerical modeling of molten pool formation during an interaction of a pulse laser (Nd: YAG) with an aluminum sheet," in *Proc. Comsol Multiphysics Conference*(2005).
6. J. Jouvard, A. Soveja, and N. Pierron, "Thermal modelling of metal surface texturing by pulsed laser," in *Proc. Comsol Multiphysics Conference*(2006).
7. S. Lu, H. Fujii, and K. Nogi, "Marangoni convection and weld shape variations in Ar–O_2 and Ar–CO_2 shielded GTA welding," Materials science and engineering: A **380**, 290-297 (2004).
8. D. Bäuerle, *Laser processing and chemistry* (Springer, 2000).
9. M. Zaeh, R. Daub, A. Mahrle, and E. Beyer, "Influence of CO2 in the Ar Process-Gas on the Heat-Conduction Mode Laser Beam Welding Process with Nd: YAG and Diode Lasers," in *Proceedings of the Fifth International WLT-Conference on Lasers in Manufacturing. München*(2009), pp. 45-51.
10. J. Blackburn, and P. Hilton, "Producing Surface Features with a 200 W Yb-fibre Laser and the Surfi-Sculpt® Process," Physics Procedia **12, Part A**, 529-536 (2011).
11. P. Hilton, and I. Jones, "A new method of laser beam induced surface modification," The Laser User, 46-48 (2008).
12. S. Giet, M. Ardron, F. Albri, M. D. Kidd, R. R. J. Maier, J. D. Shephard, N. Weston, and D. P. Hand, "Micro-sculpting of Diffractive Scales on Metal Surfaces for Optical Position Encoders, the 'YAGboss' Process," in *ICALEO 2011*(Orlando, FL, USA, 2011).
13. R. N. Walters, S. M. Hackett, and R. E. Lyon, "Heats of combustion of high temperature polymers," Fire and Materials **24**, 245-252 (2000).

Chapter 6: Conclusion and future work

6.1 Conclusion

Much of the work in this thesis is associated with the investigation and application of laser ablation of two transparent and difficult to machine materials, sapphire and fused silica. These materials have unique mechanical and optical properties that make them suitable for a range of specialized applications for example in microfluidics, integrated optics, and high temperature sensing. To precisely remove a given volume at a reasonable rate is a challenging task that few processes can achieve as quickly as the laser milling process whilst maintaining the resolution in the order of 10's of micrometers. The microfluidics industry mostly uses low cost polymer technology and reproduction processes, however in some niche products the high mechanical strength and optical transmission of fused silica or sapphire are required. Laser processing offers the possibility of modifying the material refractive index and hence writing waveguides, in addition to laser machining of optical cavities and flow channels to generate optical microfluidic devices. The picosecond laser pulse operates in the ultrashort pulsed laser regime and it is possible to ablate both materials with the laser, however we observed some signs of heating and cracking caused by heat related effects, likely to be caused by some residual heat of the pulse, the heat of the plasma plume and an accumulation behaviour of these effects. Removal rates as high as 1 mm^3s^{-1} can be achieved with IR laser pulses of 125 µJ and a repetition rate of 400 kHz. In sapphire the material removal rate is lower with only 0.2 mm^3s^{-1}. These high material removal rates however come at a price, the surface roughness when machining with the IR are significantly higher than those when machining with UV. The maximum ablation rates that were achieved with 343 nm are 0.12 mm^3s^{-1}, which is still a reasonable speed for such micro-manufacture applications. It was shown that comparing material removal rates is only part of the story, it is also important to consider the energy required for material removal. These values are all in the same range for the three wavelengths, with some advantages for the UV because the lower ablation threshold allows removal of material at much lower energies, and therefore the removal rate per joule

is higher. However the efficiency of producing the laser light at that wavelength also has to be considered, and from this perspective IR achieves the highest material removal rate for a given electrical energy input. The requirement for surface finish is often a deciding factor however it was demonstrated that the UV and green wavelengths provide the best quality since in the IR a heating effect occurs and cracking and chipping of larger chunks of material increases removal rate but greatly reduces the quality. The IR process generates chips 4 times larger than those produced by the UV (which were < 5 μm) and twice as large as with green light. Hence there is an overall tradeoff between higher quality and lower throughput when machining with the UV and high throughput but many effects of heating and reduced quality when machining with the IR. The green wavelength can in many cases be seen as the compromise between the two. It also has the advantage that the lifetime of the non-linear crystal is higher for green than for the UV. It is worth pointing out that the quality achieved with all three wavelengths is similar to many abrasive techniques if not better, and that all removal rates are much higher than that achieved with focussed ion beam milling.

One common application of fused silica is in optical fibres. A strong collaboration with the optics sensing group of Heriot-Watt University lead to a particular interest in applications of the laser for manufacturing of optical fibre sensors. The specific sensors that were discussed in this thesis are fibre cantilever sensors, which were fabricated using UV picosecond laser pulses. The wavelength was chosen because of the high quality that is desired for such intricate devices. The structure is a free standing cantilever that is attached on one side to the fibre, the cantilever has a thickness of less than 10 μm, a width of 20 μm and a length of 110 μm. The thickness is a crucial part for sensing as it is the main factor for the sensitivity. It was only possible the machine such a structure with the UV wavelength. The cracking occurring with the other wavelengths results in the cantilever shearing off during the machining process. Also the tapering angle that occurs when laser machining glasses was found to depend on the wavelength, with the smallest angles created by the UV. In addition, the tapering angle depends on the fluence of the laser. At a high laser fluence, the fibre cracked even when using the UV wavelength. At low fluence the machining did not occur on the top surface, instead cracking

occurs inside the fibre, due to laser self focussing effects. Both the high and low laser fluence therefore have to be avoided while a small tapering angle is desired. The best results were found to be at a laser fluence of 6 Jcm^{-2} which results in a tapering angle of 8°. To machine a fibre cantilever different approaches were tested, the best was to produce a tapered ridge on top of the fibre, and in a second step remove some material out of the ridge to establish the cantilever. The ridge was created by scanning the laser beam in parallel lines across the fibre end-face. A symmetrical scanning approach showed the least debris deposition, starting from the outside of the fibre and machining towards the core, with alternating the side and direction of each scan. In the next step of cutting out the cantilever, a sacrificial surface was used to catch debris, and the cut angle was adjusted to correct for the taper. With this approach it was possible to manufacture cantilevers repeatedly with a thickness of less than 10 µm and a length of 100 µm. The cavity length was typically between 30 µm and 50 µm. The time to manufacture one cantilever including the time to manually align and rotate the fibre was 6 minutes. This process was not optimized for industrial production, however it is already much faster than the currently used technique to produce similar although thinner cantilevers (4 hours with FIB machining).

The surface quality of laser machining can be problematic for generating optical surfaces, for example the typical R_q surface roughness values when machining glass with ultrashort pulsed lasers are in the range of 300-600 nm. This kind of surface results in significant optical scattering, and hence reduces the transmitted optical signal. To reduce the roughness and to increase the mechanical strength of the cantilevers thermal post processing was used. An electric arc fusion splicer was used to apply localized heat to melt the surface of the cantilever, and the resulting flow of material under surface tension smoothes the surface. This technique was very successful and it was possible to reduce the R_q surface roughness to levels below 30 nm. However because heat was applied the general shape of the cantilever often changes as well causing it to bend, and shorten in length. Using this technique the signal intensity was increased from 3 % of Fresnel reflection to 90 % of Fresnel reflection. As a result the fringe visibility is increased from 0.65 to more than 0.9. The best Fresnel reflection values, however, were achieved only with significant

shortening and bending of the cantilever, which reduced the fringe visibility. The ideal parameters were found when several short arcs were applied with a low current, cleaning the cantilever and only slightly melting it, this lead to a fringe visibility of 0.9 and a signal strength of 30 % of Fresnel reflection. These cantilevers were tested repeatedly in deflection experiments where an actuator pushes the cantilever and the response is monitored using fibre interrogation. The experiments showed a resolution better than 15 nm deflection, and the cantilevers showed no sign of damage despite repeated actuation.

The overall topic of this thesis is high precision laser micromachining and in many cases this requires ultrashort pulsed lasers. Such short pulses, however, do not always provide the highest precision. Another application that was studied was the generation of encoder scales for optical position encoders. The challenge is here to machine features that are very repeatable and of very high accuracy, the depth of the features is 200 nm ± 10 nm and a pitch of 8 µm. Whilst the main commercial interest of this industrially supported project was focussed on developing a process for stainless steel scales (work undertaken by colleagues, Stephanie Giet and Marcus Ardron), in my PhD work I investigated some alternative materials and methods. For the application, either a sinusoidal or binary grating structure can be used. The sinusoidal shape can be achieved by melting the surface and creating thermally-driven melt flow causing it to form bumps and voids, if repeated with a pitch of 8 µm this can lead to the desired structure. The other possible type of grating is a binary grating in which a step is produced by removing material to the desired depth. For both approaches a focussed line was formed by a cylindrical lens. The sample was moved by high precision stages and a laser pulse or a burst of pulses was triggered at the desired position. The heating that is caused by a burst of pulses results in controlled melting of the metal surface, the dynamics of melt flow including Marangoni effects and vapourization pressure cause the metal to flow away from the heated zone or towards the heated zone depending on the chemical structure and the ambient atmosphere. In the case of the nickel coated carbon fibre samples the results presented in this thesis demonstrate the feasibility of these samples to be processed in a similar way to the stainless steel samples that were the main aspect of the project. Melt flow can be achieved and surface features of a

similar height and pattern can be achieved. An alternative process was investigated for the production of binary scales, where the refractive index of a periodically-patterned thin transparent layer is used to provide the necessary phase shift. To generate this structure, a metal carrier layer is coated with a thin layer of polyimide before ablating lines with a suitable laser. A technique of spin coating polyimide layers of just a few 100 nm thickness was developed and samples with a thickness of 260 nm were machined. There are added complications with this process in that the refractive index of the coating was found to vary with coating thickness. In the approach investigated the metal carrier would have several functions: (i) it is the reflective layer and hence important for the sensing application; (ii) it acts as a stopping layer for laser machining ensuring that the maximum depth that is machined is only the coating thickness; (iii) it makes the sample stable. The presented results show that it is possible to produce coatings in the range of the desired thickness of 200 nm. Ultimately however this process was not pursued further as the melt process on stainless steel was found to produce a more robust scale with suitable optical performance.

In this thesis I have presented three different applications in which a laser light source was used to manufacture high precision products with a an emphasize on manufacturing. The laser is an ideal tool for many applications however as shown the shortest pulsed laser does not necessarily generate the highest precision. Also, knowledge of the process and the materials that are being machined is important. Laser micro machining of glasses and transparent dielectrics often requires ultrashort laser pulses if cracking has to be avoided. The shorter the wavelength the better the surface features however the lower the throughput of machining. With such a laser it is possible to machine intricate structures out of glass such as the fibre cantilever sensors. However, it is also possible to use a much lower cost nanosecond laser to machine to a higher precision.

6.2 Future work

The work presented in this thesis is a starting point that can be followed up with further work and investigations. The purpose of the thesis is not to fully develop a process but to investigate the possibilities. Work that can be carried out to follow up on the research presented here is further demonstrations of the fibre cantilever sensor in other applications. Some of the further applications that are partially already investigated by my colleague Jun Li include the use as a temperature sensor or a pH sensor.

The knowledge that was gained during the studies towards manufacturing fibre optic cantilever sensors can be used on further studies on microstructing of optical fibres. Some interesting new possibilities are enabled by laser machining optical fibres for example on a multi core fibre it could be possible to separate the cores and for example use this in a fibre optic fan out, that is currently difficult to produce. Also other possibilities of fibre optic sensors are enable e.g. distributed gas sensing.

The machining and microstructuring of glass materials can be used in the manufacture of bespoke optical glass structures that are currently machined by companies such as PowerPhotonic Ltd. using CO_2 lasers, the advantage here over the current technology is that a higher later resolution is possible with the shorter wavelengths and ultrashort pulsed laser.